

Micro/Nanoscale Manufacture of Advanced Materials and an Exploration of Their Properties

Lead Guest Editor: Kausala Mylvaganam

Guest Editors: Haihui Ruan, Weidong Liu, and Chengyuan Wang





**Micro/Nanoscale Manufacture of
Advanced Materials and
an Exploration of Their Properties**

Journal of Nanomaterials

**Micro/Nanoscale Manufacture of
Advanced Materials and
an Exploration of Their Properties**

Lead Guest Editor: Kausala Mylvaganam

Guest Editors: Haihui Ruan, Weidong Liu, and Chengyuan Wang



Copyright © 2018 Hindawi. All rights reserved.

This is a special issue published in "Journal of Nanomaterials." All articles are open access articles distributed under the Creative Commons Attribution License, which permits unrestricted use, distribution, and reproduction in any medium, provided the original work is properly cited.

Editorial Board

- Domenico Acierno, Italy
Katerina Aifantis, USA
Nageh K. Allam, USA
Margarida Amaral, Portugal
Martin Andersson, Sweden
Raul Arenal, Spain
Ilaria Armentano, Italy
Vincenzo Baglio, Italy
Lavinia Balan, France
Thierry Baron, France
Andrew R. Barron, USA
Hongbin Bei, USA
Stefano Bellucci, Italy
Enrico Bergamaschi, Italy
Debes Bhattacharyya, New Zealand
Sergio Bietti, Italy
Giovanni Bongiovanni, Italy
Mohamed Bououdina, Bahrain
Victor M. Castaño, Mexico
Albano Cavaleiro, Portugal
Bhanu P. S. Chauhan, USA
Shafiq Chowdhury, USA
Yu-Lun Chueh, Taiwan
Elisabetta Comini, Italy
Giuseppe Compagnini, Italy
David Cornu, France
Miguel A. Correa-Duarte, Spain
P. Davide Cozzoli, Italy
Anuja Datta, USA
Loretta L. Del Mercato, Italy
Yong Ding, USA
Zehra Durmus, Turkey
Joydeep Dutta, Oman
Ovidiu Ersen, France
Ana Espinosa, France
Claude Estournès, France
Andrea Falqui, Saudi Arabia
Matteo Ferroni, Italy
Ilaria Fratoddi, Italy
Siddhartha Ghosh, Singapore
Filippo Giubileo, Italy
Fabien Gasset, France
Jean M. Greneche, France
Kimberly Hamad-Schifferli, USA
- Simo-Pekka Hannula, Finland
Michael Harris, USA
Yasuhiko Hayashi, Japan
Michael Z. Hu, USA
Nay Ming Huang, Malaysia
Zafar Iqbal, USA
Balachandran Jeyadevan, Japan
Hassan Karimi-Maleh, Iran
Antonios Kelarakis, UK
Alireza Khataee, Iran
Ali Khorsand Zak, Iran
Philippe Knauth, France
Prashant Kumar, UK
Eric Le Bourhis, France
Jun Li, Singapore
Meiyong Liao, Japan
Shijun Liao, China
Silvia Licoccia, Italy
Nathan C. Lindquist, USA
Zainovia Lockman, Malaysia
Jim Low, Australia
Laura M. Maestro, Spain
Gaurav Mago, USA
Muhamamd A. Malik, UK
Francesco Marotti de Sciarra, Italy
Ivan Marri, Italy
Sanjay R. Mathur, Germany
Tony McNally, UK
Yogendra Mishra, Germany
Paulo Cesar Morais, Brazil
Paul Munroe, Australia
J.-M. Myoung, Republic of Korea
Rajesh R. Naik, USA
Albert Nasibulin, Russia
Toshiaki Natsuki, Japan
Hiromasa Nishikiori, Japan
Natalia Noginova, USA
Sherine Obare, USA
Won-Chun Oh, Republic of Korea
Abdelwahab Omri, Canada
Ungyu Paik, Republic of Korea
Piersandro Pallavicini, Italy
Edward A. Payzant, USA
Alessandro Pegoretti, Italy
- Oscar Perales-Pérez, Puerto Rico
Jorge Pérez-Juste, Spain
Alexey P. Popov, Finland
Thathan Premkumar, Republic of Korea
Helena Prima-García, Spain
Alexander Pyatenko, Japan
Haisheng Qian, China
You Qiang, USA
Philip D. Rack, USA
Peter Reiss, France
Ilker S. Bayer, Italy
Lucien Saviot, France
Sudipta Seal, USA
Shu Seki, Japan
Donglu Shi, USA
Bhanu P. Singh, India
Surinder Singh, USA
Vladimir Sivakov, Germany
Adolfo Speghini, Italy
Marinella Striccoli, Italy
Fengqiang Sun, China
Xuping Sun, Saudi Arabia
Ashok K. Sundramoorthy, India
Angelo Taglietti, Italy
Bo Tan, Canada
Leander Tapfer, Italy
Valeri P. Tolstoy, Russia
Muhammet S. Toprak, Sweden
R. Torrecillas, Spain
Achim Trampert, Germany
Takuya Tsuzuki, Australia
Tamer Uyar, Turkey
Luca Valentini, Italy
Antonio Vassallo, Italy
Ester Vazquez, Spain
Ajayan Vinu, Australia
Ruibing Wang, Macau
Shiren Wang, USA
Yong Wang, USA
Magnus Willander, Sweden
Ping Xiao, UK
Zhi Li Xiao, USA
Yoke K. Yap, USA
Dong Kee Yi, Republic of Korea



Jianbo Yin, China
William Yu, USA

Michele Zappalorto, Italy
Renyun Zhang, Sweden

Jeong-won Kang, Republic of Korea

Contents

Micro/Nanoscale Manufacture of Advanced Materials and an Exploration of Their Properties

Kausala Mylvaganam , Haihui Ruan, Weidong Liu, and Chengyuan Wang
Editorial (2 pages), Article ID 7216409, Volume 2018 (2018)

Effect of Functionalized Carbon Nanotubes and their Citric Acid Polymerization on Mesenchymal Stem Cells *In Vitro*

Rosa L. Garnica-Gutiérrez, Luis A. Lara-Martínez, Eduardo Palacios, Felipe Masso , Alejandra Contreras, Salomón Hernández-Gutiérrez, and Felipe Cervantes-Sodi 
Research Article (12 pages), Article ID 5206093, Volume 2018 (2018)

Fabrication and Characterization of Carbon-Based Nanofluids through the Water Vortex Trap Method

Ching-Min Cheng , Shang-Pang Yu , and Tun-Ping Teng 
Research Article (13 pages), Article ID 3264621, Volume 2018 (2018)

Electronic Pulses from Pulsed Field Emission of CNT Cathodes

Xianqi Wei , Xiaoli Wang, Xin Li , and Weihua Liu
Research Article (6 pages), Article ID 4396430, Volume 2018 (2018)

Vibration Analysis of Bilayered Graphene Sheets for Building Materials in Thermal Environments Based on the Element-Free Method

Zhengtian Wu, Yang Zhang, Fuyuan Hu , Qing Gao , Xinyin Xu, and Ronghao Zheng
Research Article (14 pages), Article ID 6508061, Volume 2018 (2018)

Tunable Multilayers of Self-Organized Silica Nanospheres by Spin Coating

Sofiane Kasmi, Jeanne Solard, Inga Tijunelyte, Alexis P. A. Fischer, Marc Lamy de la Chapelle, and Nathalie Lidgi-Guigui 
Research Article (6 pages), Article ID 6075610, Volume 2018 (2018)

Defect Analysis in Microgroove Machining of Nickel-Phosphide Plating by Small Cross-Angle Microgrooving

Xiaobin Dong, Tianfeng Zhou , Siqin Pang, Zhiqiang Liang, Qian Yu, Benshuai Ruan, and Xibin Wang
Research Article (9 pages), Article ID 1478649, Volume 2018 (2018)

Fast-LPG Sensors at Room Temperature by α -Fe₂O₃/CNT Nanocomposite Thin Films

B. Chaitongrat  and S. Chaisitsak 
Research Article (11 pages), Article ID 9236450, Volume 2018 (2018)

Editorial

Micro/Nanoscale Manufacture of Advanced Materials and an Exploration of Their Properties

Kausala Mylvaganam ¹, Haihui Ruan,² Weidong Liu,³ and Chengyuan Wang⁴

¹University of Sydney, Camperdown, NSW 2006, Australia

²Department of Mechanical Engineering, The Hong Kong Polytechnic University, Hung Hom, Kowloon, Hong Kong

³University of New South Wales, Sydney, Australia

⁴Swansea University, Swansea, UK

Correspondence should be addressed to Kausala Mylvaganam; kausala.mylvaganam@gmail.com

Received 13 June 2018; Accepted 14 June 2018; Published 30 July 2018

Copyright © 2018 Kausala Mylvaganam et al. This is an open access article distributed under the Creative Commons Attribution License, which permits unrestricted use, distribution, and reproduction in any medium, provided the original work is properly cited.

This special issue is focused on the manufacturing of advanced materials at the microscale and nanoscale and an exploration of their properties. Manufacturing at the micro/nanoscale is already an extensive field, leading to the production of improved materials and new products. A significant number of papers were received, and after going through a comprehensive peer review process, seven papers were selected to be included in this special issue. Each paper analyses different properties of nanomaterials, most of which are carbon-based. The papers published in this special issue highlight the original work related to advanced materials and will give the readers a new insight.

In the paper by C.-M. Cheng et al., carbon-based nanofluids are synthesized by a vortex trap method (VTM), with an oxyacetylene flame using different flow rate ratios of oxygen and acetylene, as the carbon source. By investigating the morphology, structure, particle size, stability, and basic physicochemical characteristics of the obtained carbon-based nanomaterials (CBNMs), the authors have identified the flow rate that gives the highest stability CBNMs.

In the paper by X. Wei et al., an infrared-laser-irradiated field-emission electronic pulse system based on carbon nanotube cathodes is demonstrated. Comparing to the present field-emission system based on metallic tips, nanotubes have much lower manufacturing cost yet render much larger tip aspect ratio and stronger field enhancement. Their results extended conventional electron sources and provided a

possibility to realize ultrashort electronic pulses as a high-frequency electron source.

In the paper by R. L. Garnica-Gutiérrez et al., acid-functionalized and poly-citric acid- (PCA-) polymerized carbon nanotubes (CNTs) were placed in contact with the extracellular membrane (ECM) of mesenchymal stem cells (MSC). The authors then examined their effects on the MSC in various biological processes, showing that PCA-polymerized CNTs are less cytotoxic and lead to less apoptotic cell death. The effects of nitrogen-doped CNTs (CNxs) are also reported. Undoped CNTs tend to stimulate cell proliferation, whereas CNxs promote the apoptotic behavior. This pioneering work provides useful guidance for further study of the role of the CNT-ECM interaction on the CNT-MSC structures which are crucial for tissue grafting.

In the paper by Z. Wu et al., vibrations are studied for double-layer graphene sheets (DLGSs) in thermal environments. The vibration equation is derived by incorporating the nonlocal elastic theory into classical plate theory (CLPT). The element-free method is then employed to implement the vibration analyses. The technique used is validated in comparison with existing models in benchmark cases. Subsequently, the authors have conducted a comprehensive study of DLGS vibration and quantified the effects of boundary conditions, nonlocal parameter, elastic foundation parameter, and temperature.

In the paper by B. Chaitongrat and S. Chaisitsak, a room temperature LPG sensor is achieved based on α -Fe₂O₃/CNT

(carbon nanotube) nanocomposite films fabricated via the Fe catalyst particles on CNTs, which were synthesized by chemical vapor deposition (CVD) and then annealed to create α -Fe₂O₃. These simple and cost-efficient methods are suitable for large-scale manufacturing. The structures, surface morphologies, and LPG response are then studied for the films via Raman spectroscopy, XPS analysis, and FE-SEM or AFM. It is shown that the LPG sensors are characterized with high sensitivity and quick response.

In the paper by X. Dong et al., submicron grooves are machined on the surface of crystalline nickel phosphide—a commonly used coating material for precision glass moulding. These subwavelength-scale features could later be replicated onto the surface of optical elements for modulating light path. To achieve the extreme of quality of machining, the nanoscale manufacturing defects such as blurs and pits are studied in detail.

In the paper by S. Kasmi et al., self-organized silica nanosphere (NS) layers are fabricated by a facile spin coating process. The authors further explore the role of the NS diameter, the spin coating acceleration, and the volume fraction in the formation and organization of NS during the coating process. The competition between the sedimentation and viscosity of the solution is recognized as the key factors that control the layer thickness. By selecting proper parameters, one can thus choose to form either a single- or double-layer of closely packed NS.

Acknowledgments

We owe the authors of this special issue, our appreciation for having contributed their research papers for publication. We also thank our expert reviewers for their expeditious and constructive comments and criticisms during their review processes.

*Kausala Mylvaganam
Haihui Ruan
Weidong Liu
Chengyuan Wang*

Research Article

Effect of Functionalized Carbon Nanotubes and their Citric Acid Polymerization on Mesenchymal Stem Cells *In Vitro*

Rosa L. Garnica-Gutiérrez,^{1,2} Luis A. Lara-Martínez,³ Eduardo Palacios,⁴ Felipe Masso ,⁵ Alejandra Contreras,⁶ Salomón Hernández-Gutiérrez,³ and Felipe Cervantes-Sodi ¹

¹Departamento de Física y Matemáticas, Universidad Iberoamericana, Prolongación Paseo de la Reforma 880, 01219 Lomas de Santa Fe, MEX, Mexico

²Facultad de Ingeniería, Universidad Panamericana, Augusto Rodin 498, Benito Juárez, 03920 Insurgentes Mixcoac, MEX, Mexico

³Molecular Biology Laboratory, School of Medicine, Universidad Panamericana, Augusto Rodin 498, Benito Juárez, 03920 Insurgentes Mixcoac, MEX, Mexico

⁴Laboratorio de Microscopía Electrónica de Ultra Alta Resolución, Instituto Mexicano del Petróleo, Eje Central Lázaro Cárdenas Norte 152, 07730 San Bartolo Atepehuacán, MEX, Mexico

⁵Instituto Nacional de Cardiología, Ignacio Chávez, Juan Badiano, Sección XVI, 14080, Mexico

⁶Laboratorio de Investigación en Biología del Desarrollo y Teratogénesis Experimental, Hospital Infantil, Dr. Márquez 162, 06720, Mexico

Correspondence should be addressed to Felipe Cervantes-Sodi; felipe.cervantes@ibero.mx

Received 27 November 2017; Revised 10 May 2018; Accepted 17 May 2018; Published 9 July 2018

Academic Editor: Chengyuan Wang

Copyright © 2018 Rosa L. Garnica-Gutiérrez et al. This is an open access article distributed under the Creative Commons Attribution License, which permits unrestricted use, distribution, and reproduction in any medium, provided the original work is properly cited.

The effects of acid-functionalized and polycitric acid- (PCA-) polymerized carbon nanotubes (CNTs) in contact with the extracellular membrane of mesenchymal stem cells (MSC), a genetically unmodified cell line with differentiation capability, was evaluated with different cellular parameters. The modified CNTs show differences in the analyzed biological behaviors, that is, intracellular incorporation, cell proliferation, apoptosis, and cytotoxicity as compared with those unpolymerized nanotubes. Due to the reduced cellular uptake of polymerized CNTs, PCA-polymerized CNTs are less cytotoxic and are associated with less apoptotic cell death than the acid-functionalized ones. The effects of nitrogen-doped CNTs (CNx) is also reported, showing that functionalized undoped CNTs present strong stimulation of cell proliferation, whereas functionalized and polymerized CNxs stimulate an apoptotic behavior. The study of MSCs in contact with CNTs and PCA is challenging due to the complexity of its various signaling components. Our results provide basis for further studies aimed to understand the relevant role that the interaction of these nanotubes with extracellular membrane could have a crucial structure for tissue grafting.

1. Introduction

Carbon nanotubes (CNTs) show great promise and notable breakthroughs have been done due to their optical [1], electrical [2], and mechanical properties, which have direct applications in biological areas [3] such as trackers for detection in cellular micro environment [4], as vehicles for delivery agents [4–6], or in cell differentiation [7, 8] and tissue regeneration [8, 9].

To obtain biocompatible features from CNTs, and because of their hydrophobic behavior, CNTs are commonly subject to different functionalization processes. The most common of these involves an acid treatment, generating carboxylic groups at the walls of the CNTs, producing functionalized CNTs (fCNT) [10–14]. However, this treatment has been found as the cause of cytotoxic effects in specific cell lines [13–15]. Another way to generate functional groups on CNTs is by modification with dendritic and hyperbranched

biocompatible polymers [16–18] by attaching chains, like molecules of the extracellular matrix, to the CNTs walls [18], allowing biocompatibility and an easier interaction between the polymerized CNTs and the cells. In addition, some polymers also improve the solubility in water and the dispersion in biological fluids [15, 19].

For example, polyethylene terephthalate (PET) and polyurethane (PU) have shown a favorable cellular response in MSCs [19, 20]. Synthetic polyethylene glycol (PEG) together with chondroitin sulfate (CS) has been used as scaffolding on chondrogenesis induced by MCSs [21–23]. Nevertheless, some results of the toxicity of polymerized CNTs with PET, PU, and PEG [20, 21, 24] suggest that these polymerizations cause toxic effects on MSCs, leading to the ongoing search for different, noncytotoxic polymers [25].

Polycitric acid (PCA) [16, 17, 26–30], a hyperbranched polymer with a highly biocompatible surface [16], has been proposed for building biological scaffolding and increasing the hydrophilicity of CNTs [17, 28], reducing their aggregation and size polydispersity, and consequently diminishing their cytotoxicity [16, 29, 31]. Additionally, it has been found that PCA polymerization process does not generate pollutant particles [27].

The polymerization of MWNTs with PCA starts with the acid-functionalized MWNTs (fMWNT) and is followed by the addition of PCA, which covalently joins carboxylic functional groups of PCA and fMWNTs via a cleavable ester, obtaining polycitric acid-MWNTs (PMWNTs), an interesting material for nanomedicine applications [17, 27, 28, 30, 32]. Although in cell therapy, mesenchymal stem cells (MSCs) cultured on scaffolding are a real option in the field of tissue engineering [33] for generate or repair of new tissue [8, 9, 34, 35], one of the major limitations is still the lack of anchoring between the damaged tissue and the cells that are supplied, because the MSCs applied by suspension directly in damaged areas produce little or null improvements on the surrounding damaged tissue [36] by trans-differentiation effect. Thus, the production of adequate scaffolds for proliferation and anchorage of MSCs is a fundamental aspect for future investigation [37]. Despite that polymerized CNTs with other materials have effects on the MSC behavior, promoting adhesion [18, 38–40], changing stem cell's shape [7, 8, 41, 42], and providing signals that may promote proliferation or differentiation [18], it is unknown if polymerized CNTs with PCA could help as intermediaries or structurally could act as a kind of staple between the extracellular matrix of a damaged tissue with the extracellular matrix of MSCs previously treated *in vitro* with PMWNT before injected. However, based on the reports of cytotoxic effects of fCNTs [11, 14, 15, 19, 25] and polymerized CNTs (PCNT), with PEG, PU, and PET [19, 25], prior to considering PMWCNT as biological scaffolding for MSCs, it is mandatory and fundamental to start by performing cytotoxic assays of cells in contact with fCNTs and fPCA-CNTs. Thus, the aim of this work is to generate and characterize a set of functionalized and PCA-polymerized CNTs to evaluate their behavior on a cellular *in vitro* model of MSCs derived from primary cultures (bone marrow). This model ensures a clean and clear genetic background without the presence of genetic

disorders such as those accumulated in cell lines previously preestablished and characterized, like those of traditional cell lines [43]. Therefore, MSCs are an excellent model to evaluate several biological parameters such as proliferation, apoptosis, cytotoxicity [36] changes in their multipotent differentiation patterns [38, 41, 42], and cell proliferation [18]. The CNTs used in this work were fully characterized after functionalization and PCA polymerization. Then, cell viability and apoptosis assays were performed, and by confocal microscopy the cell morphology and presence of CNTs were evaluated.

2. Materials and Methods

2.1. Synthesis of CNTs. MWNTs and nitrogen-doped nanotubes (CNx) were synthesized by chemical vapor deposition (CVD), following a procedure similar to the one reported by Botello-Méndez et al. [44]. Mainly a tubular furnace with a tubular quartz reactor, and quartz substrates (Figure 1(a)), is heated under a 0.2 l/min Ar flow. After reaching 850°C, microdroplets of ferrocene/toluene (3.5/96.5 wt%) or ferrocene/benzylamine (3.5/96.5 wt%) solutions were supplied—as the Fe, C, and N feedstock—by a spray pulverization chamber (Pyrosol 7901, France), at a flow rate of 2.5 l/min. After 15 minutes of CVD reaction, the system is allowed to cool down to room temperature. MWNTs and CNx were obtained from the ferrocene/toluene and ferrocene/benzylamine solutions, respectively. The length of the nanotubes are around 400 μm , growing in a “forest-like” form perpendicular to the quartz substrate surfaces (Figure 1(a)).

2.2. Functionalization. After the CNT synthesis, both types of nanotubes, MWNTs and CNx, were independently acid treated for functionalization (Figure 1(b)) [45]. 0.6 g of the CNTs were sonicated (at 750 W and 20 kHz/kwatts) for 4 hours [46] in 100 ml of an $\text{H}_2\text{SO}_4/\text{HNO}_3$ 3:1 by 3 M acid solution [13]. The solution was filtered and washed with NaOH 3 M and bidistilled water. Finally, solutions of fMWNTs and functionalized CNx (fCNx) in bidistilled water were prepared at 3 different concentrations, 1000 ng/ml, 100 ng/ml, and 10 ng/ml, by ultrasonic processing for 4 hours [46].

2.3. Citric Acid Polymerization onto fMWNTs and fCNxs. A total of 0.1 g of the respective functionalized CNTs, either fMWNTs or fCNxs, was added to a round bottom flask (Figure 1(c)); simulating the polymerization ampule equipment, the flask was set on a water bath, with magnetic stirrer and a low vacuum inlet. Five grams of monohydrate citric acid was added to the flask. The mixture was heated up to 120°C and stirred at this temperature for 30 min. After removing the water with a vacuum line, the reaction temperature was raised to 140°C and stirred at this temperature for 1 h. Again, the produced water was removed by the vacuum line, and the reaction temperature was raised to 160°C [28]. Hence, citric acid could be polymerized onto the fMWNTs or fCNxs through polycondensation reaction. Polymerization was continued in

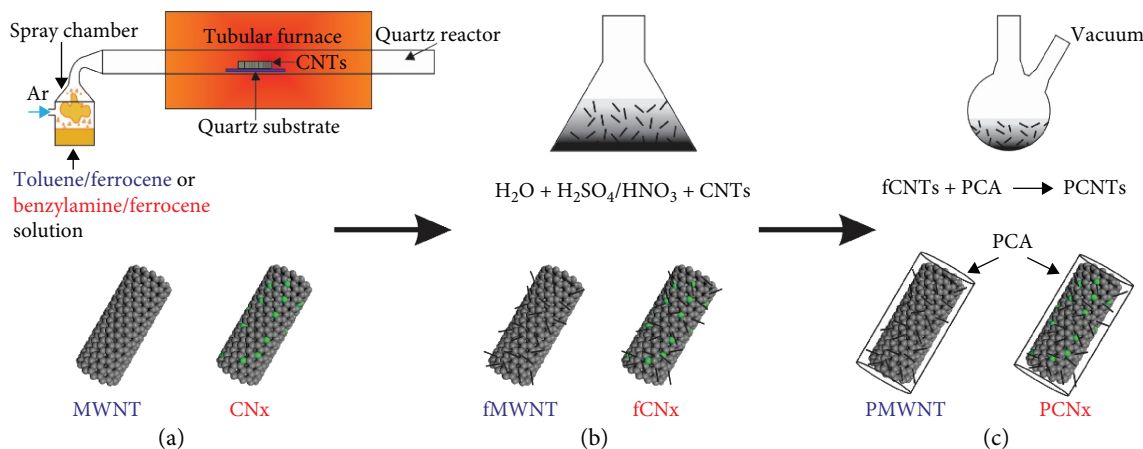


FIGURE 1: Schematic representation of the three steps for the nanotube synthesis (a), acid functionalization (b), and PCA polymerization (c), as described in the methodology. The bottom panels represent a pristine MWNT and a pristine CNx, with green spheres representing the nitrogen dopants. Nanotubes are functionalized, which causes some alteration in their external layer and finally polymerized, covered by a PCA layer.

this temperature under dynamic vacuum for 1.5 h. The procedure was like the one reported Sarlak et al. [26]. Due to the poor solubility of fCNTs and citric acid in the organic solvents, melting esterification is the best method for a polycondensation reaction between fCNTs and citric acid [27, 28]. We used monohydrate citric acid to overcome the problem of the decomposition of citric acid because its melting point is 100°C. At this temperature, polycondensation reaction partially occurs between PCA and fMWNTs or fCNxs. Then, water can be removed, and an increment of the reaction temperature leads to hyperbranched polycitric acid grafted onto fCNTs or fCNxs, obtaining PCAylated MWNTs (PMWNT) and PCAylated CNx (PCNx), respectively (Figure 1(c)). The mixture was cooled and dissolved in acetone, and the product was precipitated in bidistilled water. Finally, for the biological tests, as for fMWNTs and fCNxs, solutions of PMWNTs and PCNxs were prepared at 1000 ng/ml, 100 ng/ml, and 10 ng/ml using bidistilled water in an ultrasonic processor for 4 hours.

2.4. CNT Characterization. For morphological characterization, a dual-beam scanning electron microscope (SEM, Nova 200 Nanolab, USA) was used, coupled with an X-ray Si (Li) ultrathin window energy dispersive spectrometer (EDS) for low atomic number detection. The quantitative estimation of the elemental atomic percent was done with the ZAF method implemented on the EDAX EDS Genesis software, with a maximum accuracy error of 1 wt.%. A transmission electron microscope (TEM, Tecnai G2 F30 S-TWIN, UK) was used to analyze the CNT structure. Statistical evaluation of diameters was carried out on samples containing fMWNTs, fCNx, PMWNTs, and PCNxs. The Raman analysis (Horiba Jobin Yvon, LabRAM HR800, France) was performed with a 633 nm laser. The infrared (IR) spectra were examined with a Fourier-transform IR spectrometer (Thermo Scientific, Nicolet iS5 ID5 ATR, USA) from 1000 to 3500 cm⁻¹. Thermogravimetric analysis (TGA) (Q500,

USA) were performed under a N₂ flow of 50 ml·min⁻¹ following a calibration procedure of an isothermal heating in a heating rate of 2°C/min reaching 100°C for 30 min. Then, thermal analysis started at room temperature reaching 200°C with a heating rate of 2°C/min.

2.5. Cell Culture. MSCs derived from rat bone marrow were isolated and cloned from a heterogeneous culture [47], seeded at 10000 cell/ml suspensions, and grown in 3.0 cm² plate dishes with α -MEM medium (Sigma-Aldrich, USA) with supplemented fetal bovine serum (10%), penicillin (10,000 U), streptomycin (10 mg/ml), and amphotericin B (25 mg/ml) (Sigma-Aldrich, USA). Then, the culture was incubated at 37°C and 5% CO₂ with the three different concentrations of each kind of nanotubes: fMWNTs, PMWNTs, fCNxs, and PCNxs, at 10, 100, and 1000 ng/ml.

2.6. Cellular Proliferation. Following the cell culture preparation, a trypan blue exclusion test (TBET) [14] was performed at 0, 24, 48, 72, and 144 hours. The cells were trypsinized and resuspended in fresh culture medium. Finally, cells were counted on a hemocytometer. The cellular proliferation test was done in triplicate.

2.7. Apoptosis Assay. The cells treated at different concentrations (10, 100, and 1000 ng/ml) of fMWNTs, PMWNTs, fCNxs, PCNxs, and MSCs during 48, 72, and 144 hours were trypsinized and resuspended using an Annexin V/propidium iodide assay kit (ellEvent, USA). The cells were washed with phosphate-buffered saline/bovine serum albumin (PBS/BSA) and incubated at room temperature with a solution of annexin-V-FITC and propidium iodide for 30 min, as suggested by Jiang et al. [47]. The cells were then analyzed by flow cytometry, monitoring the fluorescence emission at 395/525 nm for annexin V-FITC and 483/659 nm for PI in a flow cytometer (FACSCalibur; Becton Dickinson, USA). The cells were seeded by triplicate; the assay was carried on in untreated MSCs as pure control

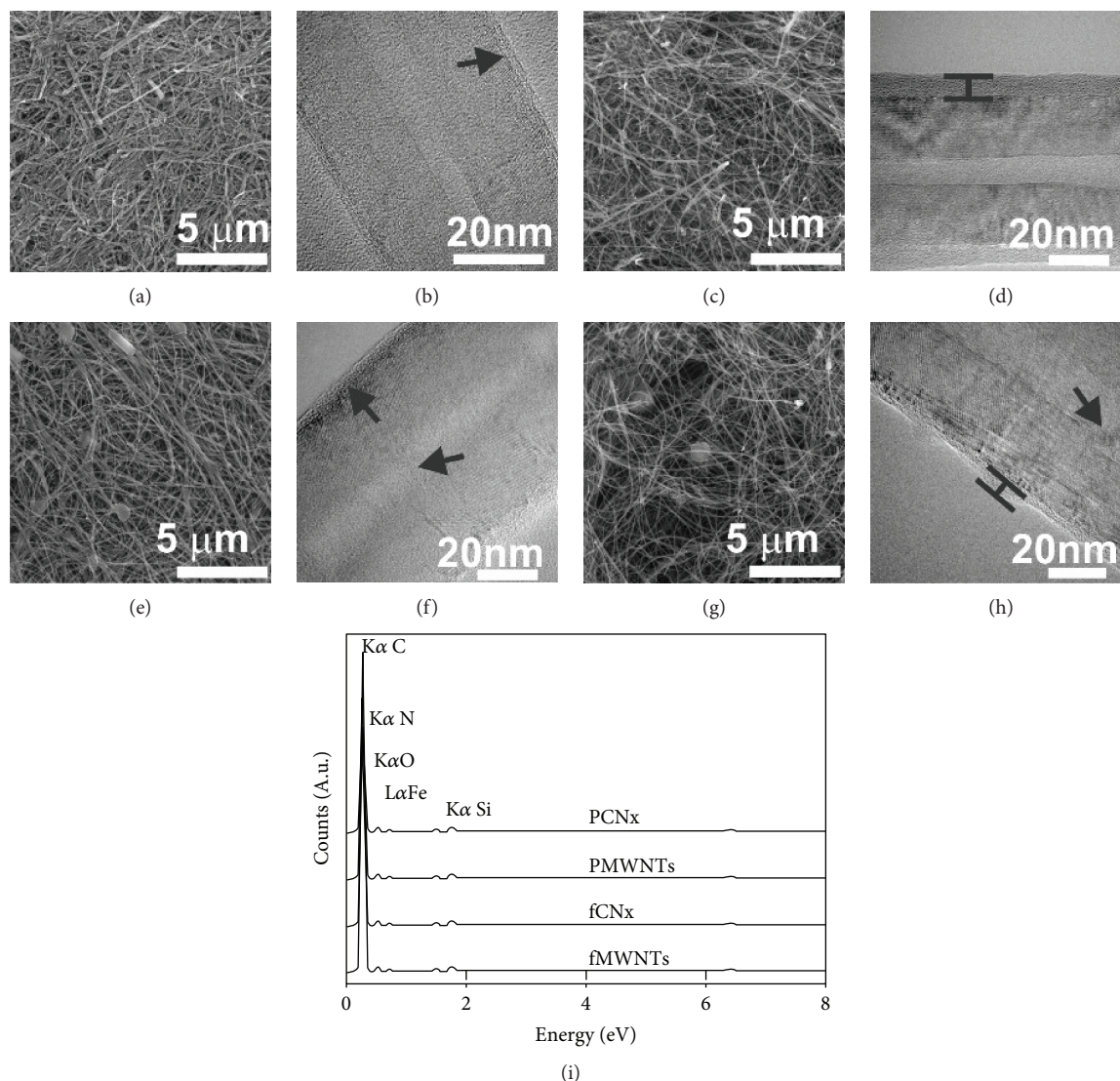


FIGURE 2: Representative SEM micrographs of (a, b) fMWNT, (c, d) PMWNT, (e, f) fCNxs, and (g, h) PCNxs. Black arrows in (b) show the functionalized edge of the CNT, while the arrows in (f, h) indicate the typical bamboo-like structure of the CNx. Arrows also indicate the thin PCA film on the surface of the (d) MWNT and the (h) CNx. The EDS spectra of the four samples are included (i); the quantitative data for C, Fe, N, and O is provided in Table 1, with a faint silicon signal arising from the substrate.

and MSC positive control containing 25, 12.5, and 2.5 μl of hydrogen peroxide, respectively.

2.8. Confocal. Cells were grown on cover slips, treated at 100 ng/ml of each type of nanotubes after 72 hours of incubation time, which was washed with PBS and fixed with 4% w/v paraformaldehyde (PFA) (Sigma-Aldrich, USA). A nuclear immunofluorescence staining was performed with Draq7 (bio status). The presence of nanotubes was revealed by autofluorescence using a laser beam at 488 and an emission filter 505-30 LB, while nuclei were seen also at 488 and 633 LB. Images were captured using a confocal microscopy (Zeiss, Germany) and analyzed by the Zen 2009 software and a confocal microscope Leica Mod. TCS sp 8x with a LAS AF 3.3.0 software.

2.9. Statistics. Three independent repetitions of each biological experimental treatment were done. Data are expressed as a mean standard deviation of the experiments. Statistic analysis was performed by analysis of variance (ANOVA). Statistical significance was inferred at $p < 0.05$.

3. Results

3.1. Nanotubes Characterization. The morphology and structure of fMWNTs, PMWNTs, fCNxs, and PCNxs are shown in the micrographs of Figure 2. The average width of the nanotubes after the functionalization is shown in Table 1, suggesting that PCA increases their diameter by 20% for fMWNTs and 24% for fCNxs. The TEM micrographs in Figures 2(b) and 2(f) show some degree of disorder on the

TABLE 1: Data of the four types of nanotubes including C, N, and Fe wt.% estimated by EDS with an estimated error of 1%; diameter of the CNTs obtained by SEM and the I_D/I_G ratio by Raman spectroscopy.

	(wt% C)	(wt% O)	(wt% N)	(wt% Fe)	Diameter (nm)	I_D/I_G
fMWNTs	94.98	2.6	—	2.44	≈89.2	0.41
PMWNTs	93.96	4.23	—	1.81	≈107.2	0.43
fCNx	92.48	3.3	2.84	1.38	≈69.3	0.89
PCNx	93.22	3.82	1.01	1.94	≈86.4	0.82
METHOD	EDS-SEM	EDS-SEM	EDS-SEM	EDS-SEM	SEM	RAMAN

external walls of the acid-treated CNTs, which complementing with the IR spectroscopy information (Figure 3) indicates the presence of carboxyl functional groups on the walls of the nanotubes, generated during the acid functionalization [45, 46]. A different kind of disorder is also noticeable as bamboo-like structures in the inner part of the fCNxs and PCNxs as shown in Figures 2(f) and 2(h), indicating the presence of nitrogen as a doping agent [48]. During synthesis of CNxs, the nitrogen tends to incorporate pentagons on the hexagonal structure of the nanotube, affecting its crystallinity and inducing curvature on the inner nanotube surfaces, generating the bamboo-shaped structures in the interior [49, 50]. Currently, CNxs are being investigated, since the effects of these irregularities may favor the interaction with polymers [48]. The polymerization of the CNTs by PCA is noticeable in Figures 2(d) and 2(h), where a thin layer of polymer covers the corresponding nanotubes, like those reported by Jiang et al. [47].

The elemental compositions for each of the four types of CNTs are shown in the EDS spectra (bottom of Figure 2 and Table 1), confirming that the nanotubes do not contain enough weight percentage of Fe pollutants that may cause cytotoxicity [15, 48]. The Fe nanoparticles are found inside the CNTs, and thus not in contact with the environment and finally not with the MSCs, avoiding chance of cytotoxicity by Fe. In fact, one of the positive side effects of the functionalization is to remove most of the catalyst nanoparticles or other compounds that are in contact with the nanotube during growth [16]. Raman spectra in Figure 4(a) yield data about the types of nanotubes and their defects [51]. Impurities and defects of carbon nanotubes are usually understood on the basis of the D band at about 1350 cm^{-1} , as reported by Datsyuk et al. [52] where the intensity (I) of the D band is related to the concentration number of defects. In contrast, the G band is associated with the graphitic or crystalline structure of the tubes and is located at 1588 cm^{-1} . The I_D/I_G ratio has been obtained for the four types of nanotubes, and it relates the defects and the crystallinity of the tubes. Functionalization and polymerization increase the amount of disordered carbon caused by the partial alteration of fMWNTs and fCNxs during the exfoliation of bundles and the polymerization treatment [50, 53]. The intensity of the D and G bands is almost constant for the MWNTs and the CNx, respectively (Figure 4); that is, only a small change in the I_D/I_G ratio appears when functionalized nanotubes are polymerized. As expected, fMWNTs and PMWNTs show a higher intensity in G band in comparison with fCNxs

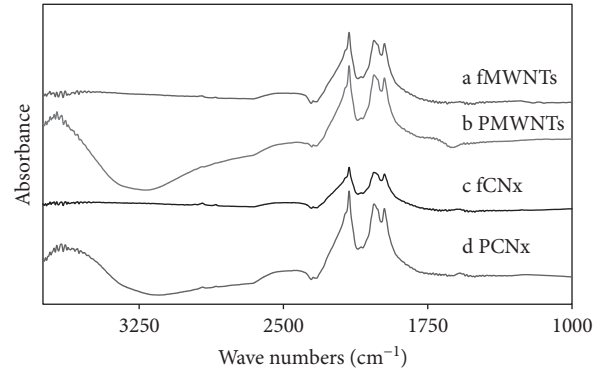


FIGURE 3: Infrared spectra of (a, c) acid-functionalized MWNTs and CNxs, respectively, showing the bands between 1750 and 2200 cm^{-1} related to the C-C bonds. The OH band obtained by functionalization is present at 2500 cm^{-1} . For the polymerized CNTs (b, d), the broad band at 3600 cm^{-1} is related to the OH groups associated to PCA.

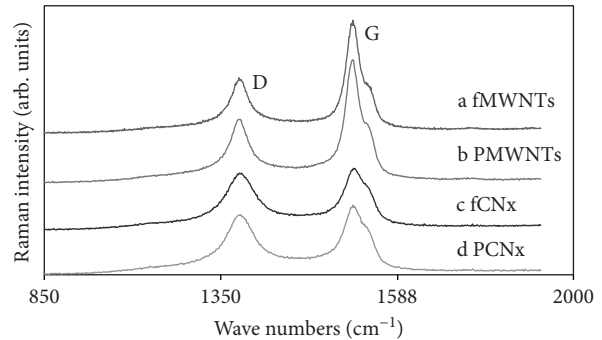


FIGURE 4: Raman spectra of CNTs using a laser exciting line of 633 nm . G and D bands appears in all the samples at around 1588 cm^{-1} and 1350 cm^{-1} , respectively.

and PCNxs. The I_D/I_G ratios of fMWCNTs and fCNxs are ~ 0.41 and ~ 0.89 , respectively, while the ratio of PMWNTs and PCNxs are ~ 0.43 and ~ 0.82 , respectively (Table 1); results derived from the mechanism of oxidation during functionalization, more effective for the external walls of the CNxs.

The chemical compositions of the 4 types of nanotubes were further confirmed by IR spectroscopy (Figure 3). All the samples show the main absorbance bands between 1750 and 2200 cm^{-1} , related to the C-C bonds of the CNT

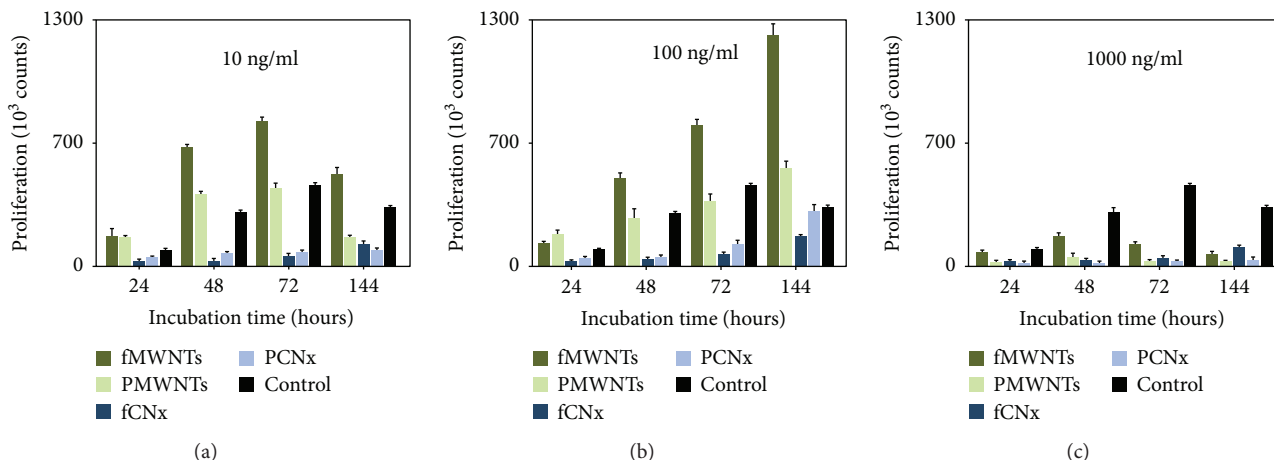


FIGURE 5: Bar plots of the proliferation effects on MSCs versus incubation time at different CNT concentrations for the four types of CNTs and a control sample. At concentrations of 10 and 100 ng/ml, fMWNTs and PMWNTs promote cell proliferation; contrarily, fCNxs and PCNx causes inhibition. A 1000 all CNTs show a cytotoxic effect. The trypan blue escalation was performed to evaluate the cell viability. Data are representative of three independent experiments and are expressed as the mean of at least three experiments with $p < 0.05$.

structure. While an increase in the intensity of this band is found in Figure 3(b) and (d) due to the bonds of the polymer, the carbonyl groups of the OH bands, obtained from the functionalization, are slightly marked at 2500 cm^{-1} in the 4 samples. The broad absorbance bands of PMWNTs and PCNxs (Figure 3(b-c)) around 3200 and 3500 cm^{-1} are related to the OH associated with acidic and alcoholic hydroxyl functional groups of the polymer [28, 29]. After SEM, TEM, and Raman characterization, confirming the structure of the functionalized and polymerized nanotubes, the IR results shown in Figure 3, consistent with the literature [28, 29, 31], further confirm the adequate functionalization and polymerization performed on the CNTs used in this experiment. Furthermore, data from thermal gravimetric analysis (TGA) (not shown) indicates that the amount of carboxylic acid groups and PCA bound to the CNTs do not change with the temperature rise; all the samples keeping a constant weight in the range from 15°C to 200°C with only 1% of variation, consistent with Vicente et al. [45]. Taking into account that the temperature required for the biomedical experiments is between 25 and 45°C , the TGA results ensure that if for some reason there are temperature fluctuations during the process, the chemical conformation of CNTs is not affected.

3.2. Biological Assays. Once the different CNT samples were characterized, we proceeded to carry out the biological assays with derived rat bone marrow MSCs as primary cultures. The effect on cell proliferation of MSCs for different concentrations of CNTs is shown in Figure 5. At 10 ng/ml (Figure 5(a)), the most significant proliferative result comes from fMWNTs, which in comparison with the control sample, almost doubles the amount of cells at 48 and 72 hours. PMWNTs show less proliferation with similar behavior with respect to the control sample at 10 ng/ml for both 48 and 72 hrs. In contrast, fCNxs and PCNxs do not show proliferative capability at 10 ng/ml. At 100 ng/ml (Figure 5(b)), fMWNTs and PMWNTs present a high proliferative

growth behavior. In contrast, fCNxs and PCNxs remain with a lower proliferative capacity than the control sample at all times. Using the highest concentration, 1000 ng/ml (Figure 5(c)), it was remarkable that cell growth was not present in any sample, with the exception of the control one. The results of proliferative analysis for fMWNTs and PMWNTs differ with the behavior reported by Jiang et al. for PEGylated MWNTs in macrophage model cells [47], with our MWNTs showing a higher proliferative rate than the macrophage cells. In order to demonstrate whether cells incubated with fCNxs and PCNxs were dying or not proliferating, an apoptosis assay by flow cytometry using the same concentrations was performed, quantifying annexin V. From the apoptosis results of the 10 ng/ml concentration (Figure 6(a)), it is evident from the beginning of the experiment that fCNxs cause cell death. The effect of the polymer is clear, with PCNxs presenting a lower level of apoptosis than fCNxs. The apoptotic tendency of fCNxs is confirmed by the proliferative assay shown in Figure 5(a), where at the same concentration and time, both fCNxs and PCNxs do not proliferate in comparison with the control sample. The cytotoxicity of CNxs could be related to the high degree of defects confirmed by the I_D/I_G ratio (Table 1). Correspondingly, at 10 ng/ml, fMWNTs generate apoptotic behavior in a similar relation to the control, while PMWNTs present a lower apoptotic behavior; that is, fMWNTs and PMWNTs induces higher proliferative capacity in contrast to fCNxs and PCNxs (Figure 5(a)). The apoptotic behavior of fCNxs at 100 ng/ml is the highest among the four types of CNT solutions (Figure 6(b)), similar to the behavior at 10 ng/ml. PCNxs at 100 ng/ml also present low apoptotic behavior with respect to fCNxs, in comparison with the 10 ng/ml concentration still presenting a higher apoptotic percentage in contrast to the positive control. Accordingly, the proliferative behavior of both fCNxs and PCNxs at 100 ng/ml always presents lower levels than untreated cells. Thus, it is very significant that for all CNxs, when inducing apoptosis, its proliferative capability decreases. In contrast,

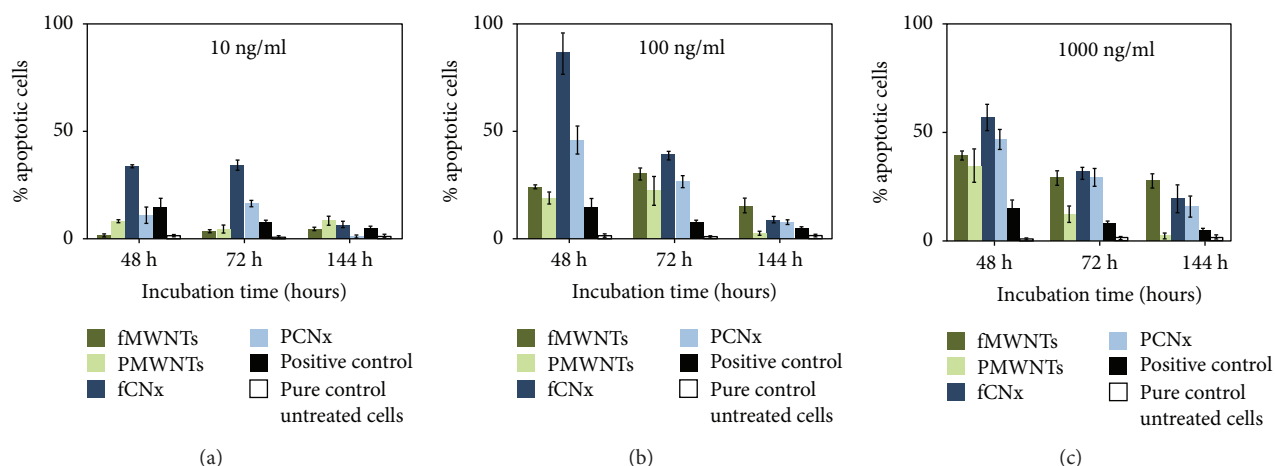


FIGURE 6: Apoptosis evaluation. fMWNTs, PMWNTs, fCNxs, and PCNxs induced apoptosis at the MSCs in comparison with the positive control and the pure control of untreated cells at CNT concentrations of 10 ng/ml (a), 100 ng/ml (b), and 1000 ng/ml (c). Apoptosis was evaluated by an Annexin/propidium iodide assay kit using a flow cytometry, determining death cell by activation of Annexin V.

fMWNTs and PMWNTs, at 100 ng/ml, present a higher apoptotic level than the positive control (still lower than fCNxs and PCNxs). In spite of this, their proliferative tendency does not diminish, increasing at all times; that is, their proliferation is activated in a significant way, particularly for fMWNT treatment. It seems that MSCs at 100 ng/ml of MWNTs show resistance to cell death and even enhance their proliferation. As time passes for the 100 ng/ml concentration, proliferation increases in all cases and the apoptosis decreases (Figures 5(b) and 6(b)). Remarkably, the PMWNT solution presents the lowest apoptotic induction and a high proliferative capacity for all times, including the 144-hour assay. Kroustalli et al. [54] reported similar results, showing that PMWNTs support adhesion and proliferation of hMSCs. Other studies indicate that polymerized CNTs present less impact in the activation of the oxidative responsible for the apoptotic pathway [55–57].

Finally, at the highest concentration of 1000 ng/ml shown in Figures 5(c) and 6(c), all the samples showed the lowest proliferative capacities sharing the same apoptotic tendencies and the same cytotoxic effects. Interestingly, the most significant results for both proliferation and apoptosis assays are at concentrations of 100 ng/ml (shown in Figures 5(b) and 6(b)), respectively, and proved statistically by three independent experiments, showing high proliferation and apoptosis for MWNTs and CNxs, respectively. The next step was to analyze by confocal microscopy the behavior of MSCs in cultures performed with CNTs from each group, focusing mainly in the 100 ng/ml concentration. Figure 7 shows the evaluation of cellular morphology and intracellular incorporation of external agents for the cultured MSCs with CNT solutions at 100 ng/ml. Starting with the behavior of the control sample for reference in Figure 7(a) (i–iv), a standard nuclear morphology is observed in the red fluorescence channel (Figure 7(a) (i)). Since no CNTs are present in the control, no fluorescence from CNTs is observed in the green channel of Figure 7(a) (ii); the match for both channels only presents the red fluorescence with a normal morphology of the whole cell,

observed in the visible light channel of panel (iv) of Figure 7(a)). The effects of 100 ng/ml solutions for all CNTs, fMWNTs, PMWNTs, fCNxs, and PCNxs, are shown in Figures 7(b)–7(e), respectively. Panels (i) of Figures 7(b) and 7(d) correspond to the red fluorescence from fMWNTs and fCNxs, respectively, both showing an apoptotic behavior represented by the nuclear destruction indicated by white circles. In comparison, PMWNTs and PCNxs, in panels (i) of Figures 7(c) and 7(e), respectively, show a well-ordered nucleus, morphologically identical to the control (Figure 7(a) (i)); a clear evidence that the PCA polymerization reduces the apoptotic behavior of fCNx as shown in Figure 6(b)).

Panels (ii) in Figures 7(b)–7(e) show the green fluorescence of the corresponding nanotubes inside the MSCs. Particularly, in the case of fMWNTs and fCNxs, shown in Figures 7(b) and 7(d), there is an evident presence of nanotubes in green, indicated by white arrows.

Panels (iii) in Figure 7 result from merging the red and green channels, corresponding to panels (i) and (ii), illustrating the exact position of the nanotubes with respect to the nucleus. Finally, visible light panels (iv) are included, where the fibrillar structure of fMWNTs and fCNxs are clearly shown inside the cells. In addition to apoptosis decrease in treated cells with PMWNTs, it is interesting that these CNTs in a major quantity remain around and out of cell (Figure 8).

4. Discussion

The uptake mechanism for carbon nanotubes has been explored [58]; seemingly, functionalization impacts directly regarding MWCNTs uptake mechanisms [59]. MWCNTs are internalized according to their diameter and length ratios as well as their size and concentration within the milieu [60]. Accordingly, as shown in Figures 7(b) and 7(d), fMWNTs and fCNxs localize inside the cell, a similar situation to that reported by Adeli et al. However, because of a structural and chemical modification, adding PCA, PMWNTs, and PCNxs is encountered in fewer occasions

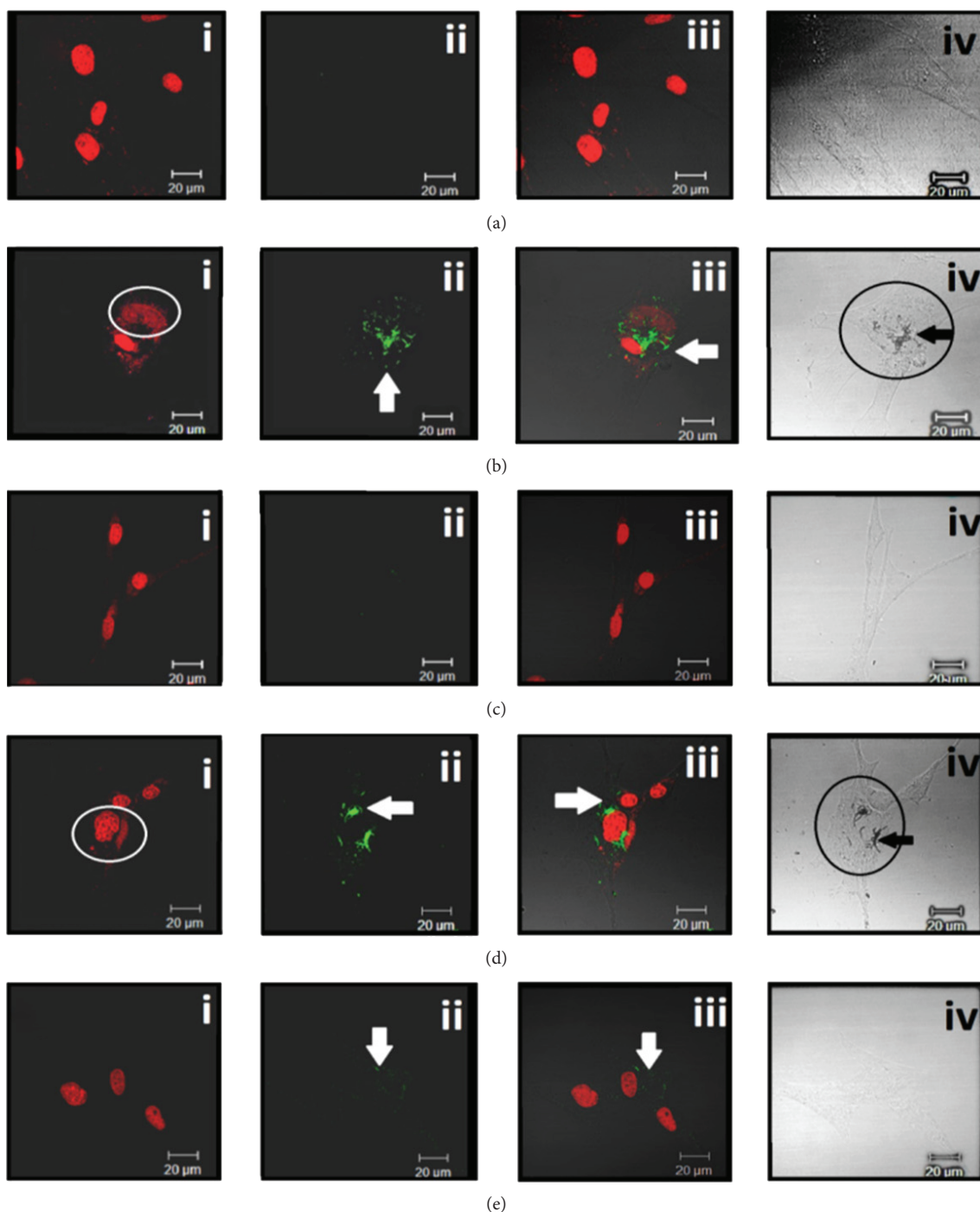


FIGURE 7: Confocal microscope images of the MSC cells incubated during 72 hours in the 100 ng/ml solution for each type of nanotube. (a) Control sample showing the red fluorescence field (at 488 nm) where the nuclei morphology is unaffected (i), the green fluorescence (at 633 nm) of CNTs with no trace of them (ii), the match of (i) and (ii) in (iii), and the bright field of the sample (iv). White arrows in panels (b–e) show the intracellular distribution of fMWNTs (b), PMWNTs (c), fCNxs (d), and PCNxs (e). Panels (i) show the red fluorescence field, illustrating the nuclei morphology; the white circles in (b, i) and (d, i) show apoptotic nuclei. Panels (ii) show green fluorescence of CNTs with clear nanotube presence in the fMWNT and fCNx samples (b, ii) and (d, ii), respectively. Panels (iii) show the match of (i) and (ii). Panels (iv) show the bright field where fMWNTs and fCNxs clearly present the fibrillar structure of the CNTs inside the MSCs.

inside the cells as compared to nonPCAYlated CNTs, although they present the required dimensions to be incorporated. The fact that PMWNTs and PCNxs do not enter the

cell can be attributed to the high presence of oxygenated groups, like those encountered in the hyperbranched PCA surfaces, which interact with proteins of the extracellular

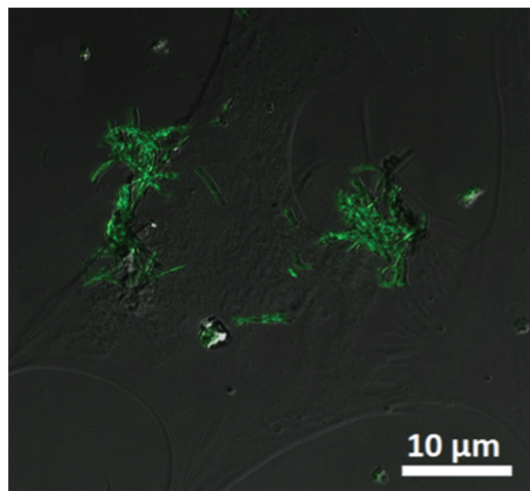


FIGURE 8: PMWNTs in contact with a MSC. Unlike the rest of the CNTs analyzed in cell cultures, the PMWNTs are in contact with the cells and mostly remain outside the cell.

matrix, reducing the cellular endocytosis mechanism [55]. Figure 8 reinforces the fact that the polymerized nanotubes enter the cell in lower amount than functionalized nanotubes, remaining in the periphery. This fact is relevant, because it would allow the MSCs have better capacity to adhere to tissue to which they are intended, once they are pretreated with PWCNT.

The effect on the morphology of the MSCs, in contact with PMWNTs and PCNxs, does not present major changes, contrasting with the results of hyperbranched polymers like PEG, reported by Murphy et al. [18, 61].

A subject of great relevance is to continue the study of the interaction between PCNTs and MSCs, but there are some interesting questions to answer beforehand, for example, can the interaction between PMWNTs and MSCs induce growth factors and secretion of substances from the cells? [18, 62]. Can the polymer interact with molecules found in the extracellular matrix [61–64], such as glycoproteins? Will this allow binding to a range of growth receptors with high affinity [18] or simply increase the adhesive capacity of the material? [54, 65, 66].

Although the initial objective of this work was to evaluate the cytotoxicity of CNT functionalized and polymerized in MSC in culture, as has been done, our study opens new fields in cell biology research for possible CNT applications modified for cell grafts.

Given these results, fCNTs entering the cell [16, 58, 67, 68] adhere to growing evidence for the fCNTs to be used as drug carrier vehicles [58, 67–72] in cancer therapy [55, 67, 70, 72], as well as for studies of cytotoxic effects [55, 58–60, 73–76]. The green fluorescence of the confocal images inside the cells confirms the fCNx uptake, a phenomenon that can be used for optical stimulation of CNTs inside living cells to afford multifunctional biological transporters of CNTs. Thus, the transporting capacity of CNTs combined with a suitable chemistry functionalization and their intrinsic optical properties can lead to novel nanomaterials for drug delivery and cancer therapy.

With the perspective of scaffolding production and design [77–79], CNTs coated with PCA may provide a clear advantage for the design of scaffolds; coated CNTs do not cause intracellular damage, because the PMWNTs cannot be internalized inside cells. So, scaffolds produced with PCNTs could be able to promote novel tissue formation, favoring cell adhesion and proliferation. Related to our results is the suggestion to use nanotube-based films linked by a bi- or tridimensional network of PCA to prevent individual nanotubes from being dislodged and entering the cell, expecting to resemble the tissue extracellular matrix [77–79], providing adequate structural support and favoring a good biomedical development.

Finally, to continue the analysis of carbon materials with the presence of MSCs, the use of PCA-polymerized graphene structures could be proposed as a biomaterial [80], hoping that graphene properties could provide different and interesting cellular responses.

5. Conclusion

This is the first time that PCA-polymerized CNTs have been used with MSCs to fix to the cellular matrix, whose result is positive and offers stability scaffold on MCS cells, having ample possibilities to generate a bridge between cells and tissues through which could facilitate the adherence of MSC directly to tissue in cell regeneration processes. An additional advantage is that nanotubes do not interfere on morphological process because the MSCs in contact with PMWNTs and PCNxs do not present major changes, in comparison with other type of hyperbranched polymerized CNTs. Our results show that apoptotic and proliferative behavior is similar between cells treated with fCNxs and PCNxs (Figure 5), presenting the lowest proliferative rates and the highest apoptotic levels (Figure 6). Functionalized and polymerized MWNTs present a higher proliferative rate and relatively low apoptotic behavior (at 100 ng/ml). According to the results, possible applications of the tested nanotubes in this work are proposed: fCNxs and PCNxs possibly suitable for the transport of substances inside the cell. fMWNTs and PMWNTs were proposed as viable materials for possible biomedical applications as cellular scaffolding.

Conflicts of Interest

The authors declare that they have no conflicts of interest.

Acknowledgments

Rosa L. Garnica-Gutiérrez thanks Felix Martínez and the Engineering Faculty of Universidad Panamericana for their support during the project. Salomón Hernández-Gutiérrez thanks funding from the CONACYT-Project 101596. Felipe Cervantes-Sodi thanks funding from the Physics and Mathematics Department, the Research Direction and FICSAC, UIA. Authors are thankful to S. Rosas-Meléndez, M. Ballesteros-Villareal, F. A. Iñiguez-Rábago, S. Macias, R. Estrada, and V. Garibay-Febles for fruitful discussions and support with experiments and characterization.

References

- [1] F. Cardano, M. Frasconi, and S. Giordani, "Photo-responsive graphene and carbon nanotubes to control and tackle biological systems," *Frontiers in Chemistry*, vol. 6, p. 102, 2018.
- [2] S. Gupta, C. N. Murthy, and C. R. Prabha, "Recent advances in carbon nanotube based electrochemical biosensors," *International Journal of Biological Macromolecules*, vol. 108, pp. 687–703, 2018.
- [3] N. L. Teradal and R. Jelinek, "Carbon nanomaterials in biological studies and biomedicine," *Advanced Healthcare Materials*, vol. 6, no. 17, 2017.
- [4] U. A. Ashfaq, M. Riaz, E. Yasmeen, and M. Z. Yousaf, "Recent advances in nanoparticle-based targeted drug-delivery systems against cancer and role of tumor microenvironment," *Critical Reviews in Therapeutic Drug Carrier Systems*, vol. 34, no. 4, pp. 317–353, 2017.
- [5] J. Pardo, Z. Peng, and R. Leblanc, "Cancer targeting and drug delivery using carbon-based quantum dots and nanotubes," *Molecules*, vol. 23, no. 2, p. 378, 2018.
- [6] M. Mir, S. Ishtiaq, S. Rabia et al., "Nanotechnology: from in vivo imaging system to controlled drug delivery," *Nanoscale Research Letters*, vol. 12, no. 1, p. 500, 2017.
- [7] L. Krishna, K. Dhamodaran, C. Jayadev et al., "Nanostructured scaffold as a determinant of stem cell fate," *Stem Cell Research & Therapy*, vol. 7, no. 1, p. 188, 2016.
- [8] E.-S. Kang, D. S. Kim, I. R. Suhito et al., "Guiding osteogenesis of mesenchymal stem cells using carbon-based nanomaterials," *Nano Convergence*, vol. 4, no. 1, p. 2, 2017.
- [9] C. Gao, P. Feng, S. Peng, and C. Shuai, "Carbon nanotube, graphene and boron nitride nanotube reinforced bioactive ceramics for bone repair," *Acta Biomaterialia*, vol. 61, pp. 1–20, 2017.
- [10] H. P. Boehm, "Surface oxides on carbon and their analysis: a critical assessment," *Carbon*, vol. 40, no. 2, pp. 145–149, 2002.
- [11] M. Kovochich, C.-C. D. Fung, R. Avansi, and A. K. Madl, "Review of techniques and studies characterizing the release of carbon nanotubes from nanocomposites: implications for exposure and human health risk assessment," *Journal of Exposure Science and Environmental Epidemiology*, vol. 28, no. 3, pp. 203–215, 2017.
- [12] A. O. Elzoghby, A. L. Hemasa, and M. S. Freag, "Hybrid protein-inorganic nanoparticles: from tumor-targeted drug delivery to cancer imaging," *Journal of Controlled Release*, vol. 243, pp. 303–322, 2016.
- [13] M. A. Correa-Duarte, N. Wagner, J. Rojas-Chapana, C. Morszeck, M. Thie, and M. Giersig, "Fabrication and biocompatibility of carbon nanotube-based 3d networks as scaffolds for cell seeding and growth," *Nano Letters*, vol. 4, no. 11, pp. 2233–2236, 2004.
- [14] D. Gutiérrez-Praena, S. Pichardo, E. Sánchez, A. Grilo, A. M. Cameán, and A. Jos, "Influence of carboxylic acid functionalization on the cytotoxic effects induced by single wall carbon nanotubes on human endothelial cells (huvec)," *Toxicology In Vitro*, vol. 25, no. 8, pp. 1883–1888, 2011.
- [15] H. Isobe, T. Tanaka, R. Maeda et al., "Preparation, purification, characterization, and cytotoxicity assessment of water-soluble, transition-metal-free carbon nanotube aggregates," *Angewandte Chemie*, vol. 118, no. 40, pp. 6828–6832, 2006.
- [16] M. Adeli, R. Soleyman, Z. Beiranvand, and F. Madani, "Carbon nanotubes in cancer therapy: a more precise look at the role of carbon nanotube-polymer interactions," *Chemical Society Reviews*, vol. 42, no. 12, pp. 5231–5256, 2013.
- [17] M. Adeli, N. Mirab, M. S. Alavidjeh, Z. Sobhani, and F. Atyabi, "Carbon nanotubes-graft-polyglycerol: biocompatible hybrid materials for nanomedicine," *Polymer*, vol. 50, no. 15, pp. 3528–3536, 2009.
- [18] W. L. Murphy, T. C. McDevitt, and A. J. Engler, "Materials as stem cell regulators," *Nature Materials*, vol. 13, no. 6, pp. 547–557, 2014.
- [19] M. Assali, A. N. Zaid, N. Kittana, D. Hamad, and J. Amer, "Covalent functionalization of swcnt with combretastatin a4 for cancer therapy," *Nanotechnology*, vol. 29, no. 24, article 245101, 2018.
- [20] Y. Gustafsson, J. Haag, P. Jungebluth et al., "Viability and proliferation of rat mscs on adhesion protein-modified pet and pu scaffolds," *Biomaterials*, vol. 33, no. 32, pp. 8094–8103, 2012.
- [21] S. Varghese, N. S. Hwang, A. C. Canver, P. Theprungsirikul, D. W. Lin, and J. Elisseeff, "Chondroitin sulfate based niches for chondrogenic differentiation of mesenchymal stem cells," *Matrix Biology*, vol. 27, no. 1, pp. 12–21, 2008.
- [22] C. Zhao, H. Andersen, B. Ozyilmaz, S. Ramaprabhu, G. Pastorin, and H. K. Ho, "Spontaneous and specific myogenic differentiation of human mesenchymal stem cells on polyethylene glycol-linked multi-walled carbon nanotube films for skeletal muscle engineering," *Nanoscale*, vol. 7, no. 43, pp. 18239–18249, 2015.
- [23] K. Bhattacharya, C. Sacchetti, P. M. Costa et al., "Nitric oxide dependent degradation of polyethylene glycol-modified single-walled carbon nanotubes: implications for intra-articular delivery," *Advanced Healthcare Materials*, vol. 7, no. 6, 2018.
- [24] T. R. Nayak, L. Jian, L. C. Phua, H. K. Ho, Y. Ren, and G. Pastorin, "Thin films of functionalized multiwalled carbon nanotubes as suitable scaffold materials for stem cells proliferation and bone formation," *ACS Nano*, vol. 4, no. 12, pp. 7717–7725, 2010.
- [25] H. Ahmadi, M. Ramezani, R. Yazdian-Robati et al., "Acute toxicity of functionalized single wall carbon nanotubes: a biochemical, histopathologic and proteomics approach," *Chemico-Biological Interactions*, vol. 275, pp. 196–209, 2017.
- [26] N. Sarlak, M. Adeli, M. Karimi, M. Bordbare, and M. A. Farahmandnejad, "Quantitative study on the interaction of ag⁺ and pd²⁺ with cnt-graft-pca (polycitric acid) in aqueous solution," *Journal of Molecular Liquids*, vol. 180, pp. 39–44, 2013.
- [27] A. Bahari, H. Hekmatara, R. Sepahvand, and M. Adeli, "Carbon nanotube-graft-poly (citric acid) containing silver and palladium nanoparticles," *Nano*, vol. 4, no. 4, pp. 217–223, 2009.
- [28] M. Adeli, A. Bahari, and H. Hekmatara, "Carbon nanotube-graft-poly (citric acid) nanocomposites," *Nano*, vol. 3, no. 1, pp. 37–44, 2008.
- [29] R. K. Kainthan, S. R. Hester, E. Levin, D. V. Devine, and D. E. Brooks, "In vitro biological evaluation of high molecular weight hyperbranched polyglycerols," *Biomaterials*, vol. 28, no. 31, pp. 4581–4590, 2007.
- [30] F. Atyabi, Sobhani, M. Adeli, R. Dinarvand, and Ghahremani, "Increased paclitaxel cytotoxicity against cancer cell lines using a novel functionalized carbon nanotube," *International Journal of Nanomedicine*, vol. 6, pp. 705–719, 2011.

- [31] B. Zhao, H. Hu, A. Yu, D. Perea, and R. C. Haddon, "Synthesis and characterization of water soluble single-walled carbon nanotube graft copolymers," *Journal of the American Chemical Society*, vol. 127, no. 22, pp. 8197–8203, 2005.
- [32] E. Heister, E. W. Brunner, G. R. Dieckmann, I. Jurewicz, and A. B. Dalton, "Are carbon nanotubes a natural solution? Applications in biology and medicine," *ACS Applied Materials & Interfaces*, vol. 5, no. 6, pp. 1870–1891, 2013.
- [33] M. J. Dalby, N. Gadegaard, R. Tare et al., "The control of human mesenchymal cell differentiation using nanoscale symmetry and disorder," *Nature Materials*, vol. 6, no. 12, pp. 997–1003, 2007.
- [34] Y. Cho, N. Shin, D. Kim, J. Y. Park, and S. Hong, "Nanoscale hybrid systems based on carbon nanotubes for biological sensing and control," *Bioscience Reports*, vol. 37, no. 2, article BSR20160330, 2017.
- [35] A. J. Engler, S. Sen, H. L. Sweeney, and D. E. Discher, "Matrix elasticity directs stem cell lineage specification," *Cell*, vol. 126, no. 4, pp. 677–689, 2006.
- [36] C. P. Hodgkinson, J. A. Gomez, M. Mirosou, and V. J. Dzau, "Genetic engineering of mesenchymal stem cells and its application in human disease therapy," *Human Gene Therapy*, vol. 21, no. 11, pp. 1513–1526, 2010.
- [37] J. Lee, A. A. Abdeen, D. Zhang, and K. A. Kilian, "Directing stem cell fate on hydrogel substrates by controlling cell geometry, matrix mechanics and adhesion ligand composition," *Biomaterials*, vol. 34, no. 33, pp. 8140–8148, 2013.
- [38] P. Bot, I. Hoefler, J. Piek, and G. Pasterkamp, "Hyaluronic acid: targeting immune modulatory components of the extracellular matrix in atherosclerosis," *Current Medicinal Chemistry*, vol. 15, no. 8, pp. 786–791, 2008.
- [39] E. Beltrán-Partida, B. Valdéz-Salas, A. Moreno-Ulloa et al., "Improved in vitro angiogenic behavior on anodized titanium dioxide nanotubes," *Journal of Nanobiotechnology*, vol. 15, no. 1, p. 10, 2017.
- [40] M. Sheikholeslam, S. D. Wheeler, K. G. Duke, M. Marsden, M. Pritzker, and P. Chen, "Peptide and peptide-carbon nanotube hydrogels as scaffolds for tissue & 3d tumor engineering," *Acta Biomaterialia*, vol. 69, pp. 107–119, 2018.
- [41] P. Tsimbouri, N. Gadegaard, K. Burgess et al., "Nanotopographical effects on mesenchymal stem cell morphology and phenotype," *Journal of Cellular Biochemistry*, vol. 115, no. 2, pp. 380–390, 2014.
- [42] S. Khetan, M. Guvendiren, W. R. Legant, D. M. Cohen, C. S. Chen, and J. A. Burdick, "Degradation-mediated cellular traction directs stem cell fate in covalently crosslinked three-dimensional hydrogels," *Nature Materials*, vol. 12, no. 5, pp. 458–465, 2013.
- [43] S. Miyagawa, Y. Sawa, S. Sakakida et al., "Tissue cardiomyoplasty using bioengineered contractile cardiomyocyte sheets to repair damaged myocardium: their integration with recipient myocardium," *Transplantation*, vol. 80, no. 11, pp. 1586–1595, 2005.
- [44] A. Botello-Méndez, J. Campos-Delgado, A. Morelos-Gómez et al., "Controlling the dimensions, reactivity and crystallinity of multiwalled carbon nanotubes using low ethanol concentrations," *Chemical Physics Letters*, vol. 453, no. 1–3, pp. 55–61, 2008.
- [45] J. L. Vicente, A. Albesa, J. Lianos et al., "Effect of acid oxidation treatment on adsorption properties of arc-discharge synthesized multiwall carbon nanotubes," *Journal of the Argentine Chemical Society*, vol. 98, pp. 29–38, 2011.
- [46] J. Liu, A. G. Rinzler, H. Dai et al., "Fullerene pipes," *Science*, vol. 280, no. 5367, pp. 1253–1256, 1998.
- [47] Y. Jiang, H. Zhang, Y. Wang et al., "Modulation of apoptotic pathways of macrophages by surface-functionalized multi-walled carbon nanotubes," *PLoS One*, vol. 8, no. 6, article e65756, 2013.
- [48] M. Terrones, A. G. Souza Filho, and A. M. Rao, "Doped carbon nanotubes: synthesis, characterization and applications," in *Carbon nanotubes*, pp. 531–566, Springer, 2007.
- [49] K. Gong, F. Du, Z. Xia, M. Durstock, and L. Dai, "Nitrogen-doped carbon nanotube arrays with high electrocatalytic activity for oxygen reduction," *Science*, vol. 323, no. 5915, pp. 760–764, 2009.
- [50] C. Bower, A. Kleinhammes, Y. Wu, and O. Zhou, "Intercalation and partial exfoliation of single-walled carbon nanotubes by nitric acid," *Chemical Physics Letters*, vol. 288, no. 2–4, pp. 481–486, 1998.
- [51] M. S. Dresselhaus, G. Dresselhaus, and P. C. Eklund, *Science of Fullerenes and Carbon Nanotubes: Their Properties and Applications*, Elsevier, 1996.
- [52] V. Datsyuk, M. Kalyva, K. Papagelis et al., "Chemical oxidation of multiwalled carbon nanotubes," *Carbon*, vol. 46, no. 6, pp. 833–840, 2008.
- [53] U. Kuhlmann, H. Jantoljak, N. Pfänder, P. Bernier, C. Journet, and C. Thomsen, "Infrared active phonons in single-walled carbon nanotubes," *Chemical Physics Letters*, vol. 294, no. 1–3, pp. 237–240, 1998.
- [54] A. A. Kroustalli, S. N. Kourkouli, and D. D. Deligianni, "Cellular function and adhesion mechanisms of human bone marrow mesenchymal stem cells on multi-walled carbon nanotubes," *Annals of Biomedical Engineering*, vol. 41, no. 12, pp. 2655–2665, 2013.
- [55] Y. Zhang, Y. Xu, Z. Li et al., "Mechanistic toxicity evaluation of uncoated and pegylated single-walled carbon nanotubes in neuronal pc12 cells," *ACS Nano*, vol. 5, no. 9, pp. 7020–7033, 2011.
- [56] X. Wang, T. Xia, S. Addo Ntim et al., "Dispersal state of multiwalled carbon nanotubes elicits profibrogenic cellular responses that correlate with fibrogenesis biomarkers and fibrosis in the murine lung," *ACS Nano*, vol. 5, no. 12, pp. 9772–9787, 2011.
- [57] L. Tabet, C. Bussy, A. Setyan et al., "Coating carbon nanotubes with a polystyrene-based polymer protects against pulmonary toxicity," *Particle and Fibre Toxicology*, vol. 8, no. 1, p. 3, 2011.
- [58] C. Caoduro, E. Hervouet, C. Girard-Thernier et al., "Carbon nanotubes as gene carriers: focus on internalization pathways related to functionalization and properties," *Acta Biomaterialia*, vol. 49, pp. 36–44, 2017.
- [59] C. L. Ursini, R. Maiello, A. Ciervo et al., "Evaluation of uptake, cytotoxicity and inflammatory effects in respiratory cells exposed to pristine and -OH and -COOH functionalized multi-wall carbon nanotubes," *Journal of Applied Toxicology*, vol. 36, no. 3, pp. 394–403, 2016.
- [60] K. Maruyama, H. Haniu, N. Saito et al., "Endocytosis of multiwalled carbon nanotubes in bronchial epithelial and mesothelial cells," *BioMed Research International*, vol. 2015, Article ID 793186, 9 pages, 2015.
- [61] D. D. Deligianni, "Multiwalled carbon nanotubes enhance human bone marrow mesenchymal stem cells' spreading but

- delay their proliferation in the direction of differentiation acceleration,” *Cell Adhesion & Migration*, vol. 8, no. 6, pp. 558–562, 2014.
- [62] W. Bai, Z. Wu, S. Mitra, and J. M. Brown, “Effects of multi-walled carbon nanotube surface modification and purification on bovine serum albumin binding and biological responses,” *Journal of Nanomaterials*, vol. 2016, Article ID 2159537, 10 pages, 2016.
- [63] C. Del Gaudio, S. Baiguera, F. Ajalloueiian, A. Bianco, and P. Macchiaroni, “Are synthetic scaffolds suitable for the development of clinical tissue-engineered tubular organs?,” *Journal of Biomedical Materials Research Part A*, vol. 102, no. 7, pp. 2427–2447, 2014.
- [64] L. Liu, W. Wu, X. Tuo et al., “Novel strategy to engineer trachea cartilage graft with marrow mesenchymal stem cell macroaggregate and hydrolyzable scaffold,” *Artificial Organs*, vol. 34, no. 5, pp. 426–433, 2010.
- [65] D.-W. Kang, F. Sun, Y. J. Choi et al., “Enhancement of primary neuronal cell proliferation using printing-transferred carbon nanotube sheets,” *Journal of Biomedical Materials Research Part A*, vol. 103, no. 5, pp. 1746–1754, 2015.
- [66] A. M. Kloxin, A. M. Kasko, C. N. Salinas, and K. S. Anseth, “Photodegradable hydrogels for dynamic tuning of physical and chemical properties,” *Science*, vol. 324, no. 5923, pp. 59–63, 2009.
- [67] A. Sanginario, B. Miccoli, and D. Demarchi, “Carbon nanotubes as an effective opportunity for cancer diagnosis and treatment,” *Biosensors*, vol. 7, no. 4, p. 9, 2017.
- [68] C.-M. Tilmaciu and M. C. Morris, “Carbon nanotube biosensors,” *Frontiers in Chemistry*, vol. 3, 2015.
- [69] H. Wang, Q. Chen, and S. Zhou, “Carbon-based hybrid nanogels: a synergistic nanoplatform for combined biosensing, bioimaging, and responsive drug delivery,” *Chemical Society Reviews*, vol. 47, no. 11, pp. 4198–4232, 2018.
- [70] J. Zhang, H. Tang, Z. Liu, and B. Chen, “Effects of major parameters of nanoparticles on their physical and chemical properties and recent application of nanodrug delivery system in targeted chemotherapy,” *International Journal of Nanomedicine*, vol. 12, pp. 8483–8493, 2017.
- [71] A. Alibakhshi, F. Abarghooi Kahaki, S. Ahangarzadeh et al., “Targeted cancer therapy through antibody fragments-decorated nanomedicines,” *Journal of Controlled Release*, vol. 268, pp. 323–334, 2017.
- [72] F. u. Din, W. Aman, I. Ullah et al., “Effective use of nanocarriers as drug delivery systems for the treatment of selected tumors,” *International Journal of Nanomedicine*, vol. 12, pp. 7291–7309, 2017.
- [73] S. F. Larner, J. Wang, J. Goodman, M. B. O’Donoghue Altman, M. Xin, and K. K. W. Wang, “In vitro neurotoxicity resulting from exposure of cultured neural cells to several types of nanoparticles,” *Journal of Cell Death*, vol. 10, 2017.
- [74] A. Ali, M. Suhail, S. Mathew et al., “Nanomaterial induced immune responses and cytotoxicity,” *Journal of Nanoscience and Nanotechnology*, vol. 16, no. 1, pp. 40–57, 2016.
- [75] J. K. Fard, S. Jafari, and M. A. Eghbal, “A review of molecular mechanisms involved in toxicity of nanoparticles,” *Advanced Pharmaceutical Bulletin*, vol. 5, no. 4, pp. 447–454, 2015.
- [76] J. Dong and Q. Ma, “Advances in mechanisms and signaling pathways of carbon nanotube toxicity,” *Nanotoxicology*, vol. 9, no. 5, pp. 658–676, 2015.
- [77] N. Huebsch, P. R. Arany, A. S. Mao et al., “Harnessing traction-mediated manipulation of the cell/matrix interface to control stem-cell fate,” *Nature Materials*, vol. 9, no. 6, pp. 518–526, 2010.
- [78] B. Trappmann, J. E. Gautrot, J. T. Connelly et al., “Extracellular-matrix tethering regulates stem-cell fate,” *Nature Materials*, vol. 11, no. 7, pp. 642–649, 2012.
- [79] X. Li, H. Liu, X. Niu et al., “The use of carbon nanotubes to induce osteogenic differentiation of human adipose-derived mscs in vitro and ectopic bone formation in vivo,” *Biomaterials*, vol. 33, no. 19, pp. 4818–4827, 2012.
- [80] N. Li, Q. Zhang, S. Gao et al., “Three-dimensional graphene foam as a biocompatible and conductive scaffold for neural stem cells,” *Scientific Reports*, vol. 3, no. 1, p. 1604, 2013.

Research Article

Fabrication and Characterization of Carbon-Based Nanofluids through the Water Vortex Trap Method

Ching-Min Cheng ¹, Shang-Pang Yu ¹, and Tun-Ping Teng ²

¹Department of Mechatronic Engineering, National Taiwan Normal University, No. 162, Sec. 1, Heping E. Road, Da'an District, Taipei City 10610, Taiwan

²Department of Industrial Education, National Taiwan Normal University, No. 162, Sec. 1, Heping E. Road, Da'an District, Taipei City 10610, Taiwan

Correspondence should be addressed to Shang-Pang Yu; ysb@ntnu.edu.tw

Received 29 December 2017; Revised 2 April 2018; Accepted 8 April 2018; Published 15 May 2018

Academic Editor: Kausala Mylvaganam

Copyright © 2018 Ching-Min Cheng et al. This is an open access article distributed under the Creative Commons Attribution License, which permits unrestricted use, distribution, and reproduction in any medium, provided the original work is properly cited.

This study designed an efficient one-step method for synthesizing carbon-based nanofluids (CBNFs). The method employs the vortex trap method (VTM) and an oxygen-acetylene flame, serving as a carbon source, in a manufacturing system of the VTM (MSVTM). The flow rate ratio of O₂ and C₂H₂ was adjusted to form suitable combustion conditions for the reduced flame. Four flow rate ratios of O₂ and C₂H₂ were used: 1.5 : 2.5 (V1), 1.0 : 2.5 (V2), 0.5 : 2.5 (V3), and 0 : 2.5 (V4). The morphology, structure, particle size, stability, and basic physicochemical characteristics of the obtained carbon-based nanomaterials (CBNMs) and CBNFs were investigated using transmission electron microscopy, field-emission scanning electron microscopy, X-ray diffraction, Raman spectrometry, ultraviolet-visible-near-infrared spectrophotometry, and a particle size-zeta potential analyzer. The static positioning method was utilized to evaluate the stability of the CBNFs with added EP dispersants. The evaluation results revealed the morphologies, compositions, and concentrations of the CBNFs obtained using various process parameters, and the relation between processing time and production rate was determined. Among the CBNMs synthesized, those obtained using the V4-0 flow rate ratio had the highest stability when no EP dispersant was added. Moreover, the maximum enhancement ratios of the viscosity and thermal conductivity were also obtained for V4-0: 4.65% and 1.29%, respectively. Different types and concentrations of dispersants should be considered in future research to enhance the stability of CBNFs for further application.

1. Introduction

Nanofluids (NFs) are solid-liquid mixtures containing nanoscale materials such as nanoparticles (NPs), nanofibers, nanotubes, nanowires, nanorods, nanosheets, and droplets. The base fluids are commonly used fluids such as ethylene glycol (EG), mineral oil, or a mixture of various liquids (e.g., EG and water or water and propylene glycol) [1, 2]. The primary advantage of NFs is that they have superior thermophysical properties to conventionally used fluids. These superior thermophysical properties result in higher efficiency of their heat exchange [3, 4]. Moreover, the addition of nanoscale particles to NFs can result in considerably lower pressure drops, blocks, wear, and energy consumption in heat exchange system pipelines, thereby improving the availability

of NFs. Therefore, NFs have numerous potential applications in engineering, especially in the fields of electromechanics, air conditioning, automobiles, manufacturing, machining, solar energy, building structures, and biomedicine [5–10].

The NF synthesis methods can be divided into two categories—one-step and two-step methods. In the one-step method, NPs are directly synthesized in base fluids; thus, the synthesized NFs have high stability. However, the geometric appearance and size of the NPs and the concentration of the NFs are limited. In the two-step method, NPs are synthesized in advance and then distributed in the base fluid to form an NF. The concentration and particle size distribution of the NFs produced in the two-step method can be easily controlled; however, these NFs have low stability. Therefore, it is crucial to improve the long-term stability of NFs by adding

dispersants and conducting pH control, mechanical stirring, and dispersion [5, 11].

The one-step methods for producing NFs, such as sputtering arc discharge, laser ablation, water-assisted synthesis, and flame synthesis, are the most common. Ishida et al. [12] prepared thiolate-protected fluorescent silver NPs by conducting sputtering deposition onto a liquid matrix. Nguyen et al. [13, 14] synthesized Ag–Au alloy NPs in a liquid by utilizing a novel approach known as double target sputtering. This method allows the manipulation of NP composition, size, and optical properties by controlling the sputter parameters for each metal target. Farajimotlagh et al. [15] synthesized η -Al₂O₃ NPs by conducting direct-current arc discharge in ethanol and methanol, which are environmentally friendly liquid carrier media. The size of the synthesized NPs was between 37 and 50 nm. Hayashi et al. [16] prepared hydrophilic carbon NPs (CNPs) from amino acids by conducting pulsed arc discharge over an aqueous solution surface under pressurized argon at 4 MPa. This method produced CNPs that were highly dispersible in water because the amino acids provided hydrophilic groups. Zhang et al. [17] efficiently prepared silver NPs by using large-area arc discharge in a liquid. The minimum size of the synthesized silver NPs was 33 nm. Amans et al. [18] reviewed the nanocarbon material preparation methods that employed a pulse laser in a liquid. Palazzo et al. [19] prepared “naked” gold NPs (AuNPs) in the absence of capping agents by performing pulsed laser ablation in a liquid; these AuNPs were stabilized by negative charges. Krstulović et al. [20] prepared colloidal Al-doped ZnO NPs by using Nd:YAG pulsed laser ablation of a ZnO:Al₂O₃ target with two laser wavelengths (1064 and 532 nm) in a water medium. The size of the synthesized Al-doped ZnO NPs was between 20 and 30 nm. Sathya et al. [21] presented a simple, one-step approach named microwave-assisted synthesis for the preparation of water-dispersible magnetic nanoclusters (MNCs) of superparamagnetic iron oxide; this method involved reducing Fe₂(SO₄)₃ in sodium acetate, polyethylene glycol, and EG within a microwave reactor. The average size of the MNCs increased from 27 to 52 nm as the reaction time was increased from 10 to 600 s. Golestan et al. [22, 23] studied nanocatalysts that were synthesized through a hydrothermal procedure in a fixed-bed reactor. Teng et al. [24] fabricated nanocarbon-based NFs using the oxygen-acetylene flame synthesis method. By adjusting the oxygen-acetylene ratio, the size of the synthesized CNPs was varied between 20 and 30 nm. In the present study, the oxygen-acetylene flame synthesis method was employed to produce CNPs, and hybrid NFs were collected using vortex trap equipment. This method is a fast, efficient, simple, and energy-conserving approach to the synthesis of carbon NFs.

In recent years, numerous studies of materials such as nanocarbons, carbon nanotubes, and graphene have been conducted and have discovered that these materials have high thermal conductivity [25–28], excellent heat transfer performance [29, 30], and physical properties that are unique for such materials [21–34]. Therefore, carbon-based nanomaterials are one of the most popular research areas. This study employed the vortex trap method (VTM) with an oxygen (O₂)–acetylene (C₂H₂) flame as the carbon source

to develop a manufacturing system of the VTM (MSVTM) for fabricating carbon-based NFs (CBNFs) through the one-step synthesis method. The MSVTM has features such as a simplistic system design, low-cost production, convenient and safe manufacturing procedures, and no requirement of additional chemicals. Moreover, the CBNFs produced using the one-step synthesis method generally have high suspension performance because of the optimal surface wettability of the suspended nanoparticles. The MSVTM was used at various flow rate ratios of O₂ and C₂H₂ to produce varying combustion conditions of the reduced flame. The morphology, structure, particle size, suspension performance, and basic physicochemical characteristics of the carbon-based nanomaterials (CBNMs) and CBNFs were investigated by utilizing appropriate techniques such as transmission electron microscopy (TEM), field-emission scanning electron microscopy (FE-SEM), X-ray diffraction (XRD), Raman spectrometry, ultraviolet–visible–near-infrared spectrophotometry (UV–Vis–NIR), and a particle size-zeta potential analyzer. Moreover, the feasibility of manufacturing CBNFs by using the MSVTM was evaluated.

2. Preparation of CBNFs

The one-step synthesis method known as the VTM was employed to prepare CBNFs. The layout of the MSVTM for synthesizing CBNFs is displayed in Figure 1. An O₂–C₂H₂ flame was utilized as the carbon source. The MSVTM comprised curved baffles, baffles with a labyrinth structure, a jagged baffle, a smoke cover, a collection tank, an exhaust fan, a digital mass flow controller (MFC), an electromagnetic stirrer, and an O₂–C₂H₂ torch. As shown in Figure 1, filtered tap water was placed in the collection tank. Subsequently, the electromagnetic stirrer (HMS-102, FARGO, Taiwan) was turned on at approximately 500 rpm to create a disturbance in the water and to increase the cooling and collection efficiency on the water surface for suspended particles in air at stage 1. Finally, the exhaust fan was switched on to produce air flow (approximately 0.2 m³/s), which generated negative pressure in the MSVTM and sucked air from the front of the jagged baffle. Due to the asymmetric shape of the jagged baffle's holes and the change in the internal structure and configuration of the jagged baffle, a strong disturbance was caused in the intake air of the MSVTM. Moreover, the strong disturbance in the intake air produced a vortex that splashed the water to cool and collect the suspended particles in the air. An MFC was used to control the flow rate and O₂–C₂H₂ ratio, while a flame was produced using the O₂–C₂H₂ torch. The O₂–C₂H₂ flame was used as a carbon source and was lit under a smoke cover over the water surface. The smoke generated by the O₂–C₂H₂ flame was sucked into the MSVTM. Therefore, the smoke was cooled and condensed by the disturbed water (stage 1) and splashing water (stages 2 and 3) to form a CBNM. When the mixture of CBNM and water had flowed into the collection tank, CBNFs were produced. This CBNF manufacturing technology has considerable potential.

The manufacturing process parameters of the MSVTM for yielding CBNFs are detailed as follows. The amount of water in the collection tank was 2 L for each process; the C₂H₂

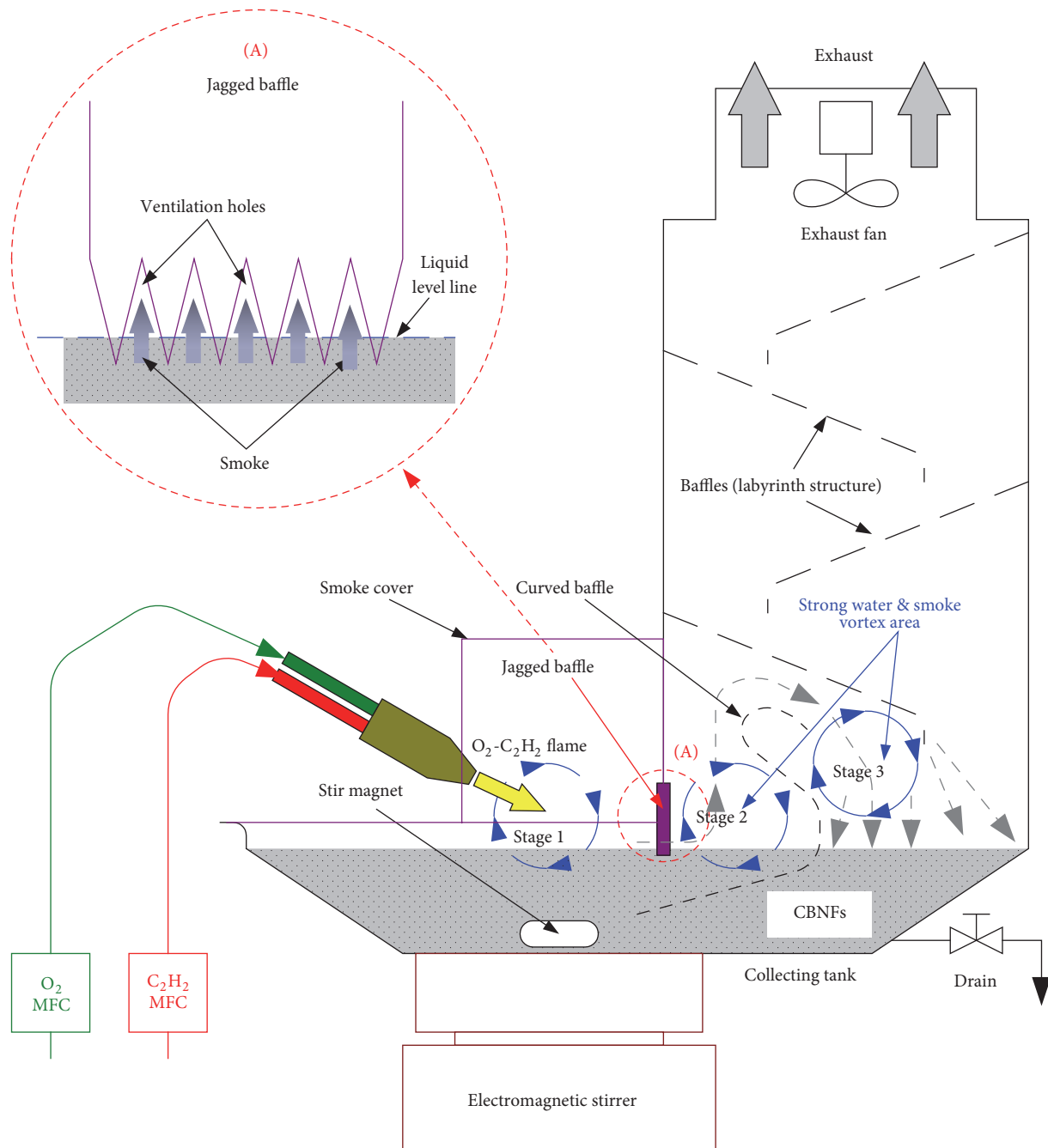


FIGURE 1: Schematic of the MSVTM for preparing CBNFs.

flow rate was fixed at 2.5 L/min at a pressure of 1.5 kg/cm²; and the O₂ flow rate was controlled in the range 0–1.5 L/min at a pressure of 3.0 kg/cm². The flow ratio and pressure settings of C₂H₂ and O₂ were based on the settings used in previous studies [24]. The O₂–C₂H₂ fuel was employed in four flow ratio configurations—V1 (1.5 : 2.5), V2 (1.0 : 2.5), V3 (0.5 : 2.5), and V4 (0 : 2.5). The flame was a reduction flame because the O₂ proportion was lower than the C₂H₂ proportion. An increase in the proportion of oxygen in the O₂–C₂H₂ flame was expected to result in more complete combustion, less smog, and less CBNM. In this study, each flow ratio

configuration was employed for 3, 6, 9, and 12 min; thus, a total of 16 CBNF samples were obtained. In the combustion process, some water vaporized; thus, water was frequently replenished to maintain the water level in the tank. When the CBNFs were removed from the collection tank, 1 L of water was slowly poured into the collection tank to drain the carbon attached to the collection tank. The volume of CBNFs yielded per process parameter and time configuration was approximately 3 L.

To improve the suspension and dispersion performance of the CBNMs in water, the collected CBNFs were stirred

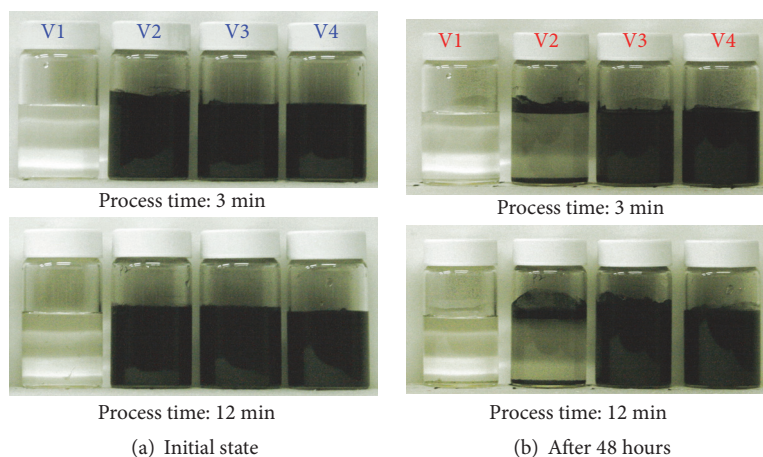


FIGURE 2: Photographs of CBNFs obtained using various process parameter configurations.

using a stirrer/hot plate (PC420D, Corning, USA) operated at 450 rpm for 2 h, after which they were homogenized at 5000 rpm for 20 min using a homogenizer (YOM300D, Yotec, Taiwan). Subsequently, the CBNFs were bathed in an ultrasonic bath (5510R-DTH, Branson, USA) for 30 min and then subjected to an intermittent oscillation process (35% amplitude, on/off duty cycle was 30/10 s) by using an ultrasonic liquid processor (Q700, Qsonica, USA) for 10 min. By using these dispersing devices consecutively and three times for short periods, temperature increases in the dispersing devices and the CBNFs were effectively prevented, thus achieving excellent dispersion. This technique was employed on the basis of the authors' research experience. Figure 2(a) displays photographs of the CBNFs fabricated using various process configurations. In contrast to the V1 CBNFs, which were almost transparent, the other CBNFs were dark. Figure 2(b) displays all the samples that were statically placed for 48 h to evaluate their suspension status; the V2 CBNFs exhibited obvious sedimentation. After dispersed CBNFs were produced, they were subjected to a series of examinations for determining their characteristics.

3. Evaluation of the Characteristics of the CBNFs

3.1. Morphology, Crystallization, and Structure Analyses. TEM (H-7100, Hitachi, Japan) and FE-SEM (JSM-7610F, JEOL, Japan) were used to identify the morphologies of the obtained CBNMs in the CBNFs. The shapes and sizes of the CBNMs were determined. The crystallization of the CBNMs was analyzed using XRD (D8 Advanced, Bruker, Germany) with Cu K α radiation. Raman spectroscopy (532.15 nm, NRS 4100, Jasco, Japan) was employed to detect the Raman shift in the D and G peaks of the CBNM spectra. The CBNFs were placed on glass sheets (20 \times 20 \times 0.6 mm³) and dried by heating to form carbon films in advance of conducting XRD and Raman spectroscopy. Because the concentrations of the V1 CBNFs were extremely low, a vacuum concentrator was used to increase the concentration of the test samples for all the aforementioned measurements.

3.2. Production Rate Analysis. The CBNM production rate for each process parameter configuration was measured for determining the concentration of CBNMs in the CBNFs [24]. A moisture analyzer (MX-50, A&D, Japan) was used to remove moisture from a 25 g sample of each CBNF by heating, and the remaining weight was utilized (weighing method) to estimate the CBNM concentration in the CBNF sample. Samples were weighed before and after drying. Because the highest resolution of the moisture analyzer was only 1.0 mg, a high-precision electronic balance (0.01 mg/42 g, GR202, A&D, Japan) was employed to improve the weighing accuracy. The entire weighing procedure was repeated four times, and the average value of test data was calculated to determine the CBNM content weight of a CBNF for each process parameter configuration. Finally, the actual weight concentration in each CBNF was obtained from the CBNM content weight and CBNF sample weight.

3.3. Stability Analysis. To appropriately employ the stability test and facilitate the stability comparison (suspension and dispersion performance), samples that were synthesized using various process parameters were adjusted to the same concentration by diluting with water or concentrating with a vacuum concentrator, because the concentrations of all the CBNFs were not equal. Moreover, if a CBNF had poor stability, the accuracy and reliability of the characteristic measurements were affected. Figure 2 displays that V2 had poor stability, and obvious sedimentation was observed through static positioning. Hence, the stability of each sample was tested by adding a nonionic dispersant (EP dispersant, polyoxyethylene alkyl ether; EP9050, First Chemical, Taiwan) in various concentrations. The samples with optimal stability were subjected to the following measurements of particle size (d_p), zeta potential (ζ), and basic physicochemical characteristics. To determine their stability, the CBNFs were mainly tested using static positioning and UV-Vis-NIR (V670, Jasco, Japan). An elaborate account of the static positioning method is provided as follows. First, a CBNF was placed into a transparent sample bottle, and the sediment difference was visually observed after 120 h. To measure the difference

in the absorbance at the initial (ABS_i) and static position for each CBNF after 48 h (ABS_{48h}), UV–Vis–NIR combined with static positioning (2.5-mL CBNF sample in a transparent cuvette) was performed. The absorbance difference ratio (R_{ABS}) was calculated using (1) and utilized to determine the stability of the CBNF. A lower R_{ABS} represents a higher CBNF stability.

$$R_{ABS} = \left[\frac{(ABS_i - ABS_{48h})}{ABS_i} \right] \times 100\%. \quad (1)$$

Moreover, the stability of a CBNF can be evaluated using the suspended d_p distribution, average suspended d_p , and ζ . The suspended d_p of CBNMs is similar to the d_p observed using electron microscopy, thus indicating the favorable dispersion of the CBNMs in the CBNFs. Moreover, the larger the absolute value of ζ , the higher the stability of an CBNF. The ζ values of the colloidal dispersions were within the ranges 0 to ± 10 , ± 10 to ± 30 , ± 30 to ± 40 , and ± 40 to ± 60 mV; these values indicated rapid coagulation or flocculation, incipient instability, moderate stability, and favorable stability, respectively. When the magnitude of the ζ of a NF is greater than 60 mV, the colloidal dispersion has excellent stability [35, 36]. The dynamic light-scattering method was conducted for d_p and ζ analysis. A CBNF into which a 6 mm gold-plated electrode cell was placed was simultaneously measured by using a nanoparticle analyzer (SZ-100, HORIBA, Japan) to evaluate the average d_p , the d_p distribution, and ζ . The d_p and ζ values for each CBNF were measured five times, and the average d_p and ζ were then calculated.

3.4. Basic Physicochemical Characteristic Measurements. The basic physicochemical characteristics measured for the CBNFs were pH, electrical conductivity (E), density (ρ), viscosity (μ), and thermal conductivity (k), which were measured using a pH meter (SensION+ MM374, Hack, USA) with an accuracy of ± 0.002 pH and $\pm 0.5\%$, an electrical conductivity meter (SensION+ MM374), a liquid density meter (DA-130N, KEM, Japan) with an accuracy of ± 0.001 g/mL, a viscosity meter (T15-3, Hydramotion, England) with an accuracy of $\pm 1.0\%$, and a thermal properties analyzer (KD-2 Pro, Decagon Devices, USA) with an accuracy of $\pm 5.0\%$, respectively. These measurements were made in an isothermal bath (P-20, YSC, Taiwan) to provide individual sample temperature control of 30, 40, or 50°C within $\pm 0.5^\circ\text{C}$. To increase the experimental accuracy, these experiments were conducted six times, and the four most similar values were used to obtain the average.

In a high-purity nitrogen (5 N) atmosphere, the specific heat (c_p) of the test samples was measured using a differential scanning calorimeter (DSC, Q20, TA, USA) with a mechanical refrigeration system (RCS40, TA, USA). The temperature and calorimetric accuracies of the DSC were $\pm 0.1^\circ\text{C}$ and $\pm 1.0\%$, respectively. The c_p test method used was the standard reference approach, and the standard reference was pure water [37]. The experimental temperature was between 10 and 80°C, and the heating rate was maintained at 10°C/min. To increase the measurement accuracy, the experiments were conducted thrice for each CBNF, and the average c_p value of the CBNF was then calculated.

3.5. Data Analysis. The experimental results were transformed into a change ratio (CR) for comparison of water with the CBNFs; the CR can be expressed as

$$CR = \left[\frac{(D_{\text{CBNFs}} - D_w)}{D_w} \right] \times 100\%. \quad (2)$$

4. Results and Discussion

Figures 3 and 4 display TEM and FE-SEM images of the CBNMs obtained using the four process flow ratio configurations (V1–V4) and processing times of 3 and 12 min. Spherical CBNMs (d_p : approximately 20–50 nm) were synthesized mostly when the V2–V4 configurations were used, whereas flaky CBNMs were mostly obtained using V1. Flaky CBNMs were thus obtained when the proportion of O_2 was increased. Conversely, a high proportion of C_2H_2 contributed to the formation of CBNMs with more spherical particles. Moreover, the processing time of the MSVTM was not discovered to affect the particle size and morphology of the CBNMs. The FE-SEM and TEM images of CBNMs indicate that processing time did not affect d_p for parameter configurations V2–V4, but differences were observed when V1 was employed. Although FE-SEM and TEM images can partially display d_p and morphology, a nanoparticle analyzer was required to confirm the d_p distribution and average d_p of the suspended CBNMs in CBNFs. Moreover, XRD and Raman spectroscopy were necessary to identify the material in the follow-up tests.

Figure 5 displays XRD patterns of the CBNMs that were synthesized by employing V1–V4. The CBNMs could barely be distinguished. However, dissimilarities existed within the composition and crystalline state of the samples. By using XRD, we observed that the (001) diffraction peak was located at a 2θ value of 11° and that graphene oxide (GO) was the primary constituent of most of the CBNMs. The peaks at 2θ between 21° and 27° suggest that this range overlaps the (002) diffraction peak of graphite, which has a 2θ of 26.5° . A broad diffraction peak at 2θ between 23° and 24° is observed in Figure 5. In some materials, most of the functional groups had been removed, which provides clear evidence that some amount of reduced GO (RGO) was present in these CBNMs [38–40]. The CBNMs were generated by using an O_2 – C_2H_2 reduction flame, and reduction gases such as carbon monoxide were present in the combustion products of the reduction flame. Moreover, a very small amount of free oxygen was present to produce different degrees of reduction reactions. The reduction reaction caused the functional groups in the internal layers of GO to gradually disappear, and thus, GO was gradually reduced to RGO [38–40]. Furthermore, the crystallization of the CBNMs for various process parameters was inferior due to the broad range of the (002) diffraction peak. Hence, in this study, amorphous carbon (AC) was included, and different proportions of GO, RGO, and AC were required to synthesize CBNMs by using different process parameter configurations.

The Raman spectra displayed in Figure 6 were used to determine the structure of the CBNMs synthesized using V1–V4. The test samples had three test points, and one of the three test points was chosen for Figure 6. Table 1 presents the

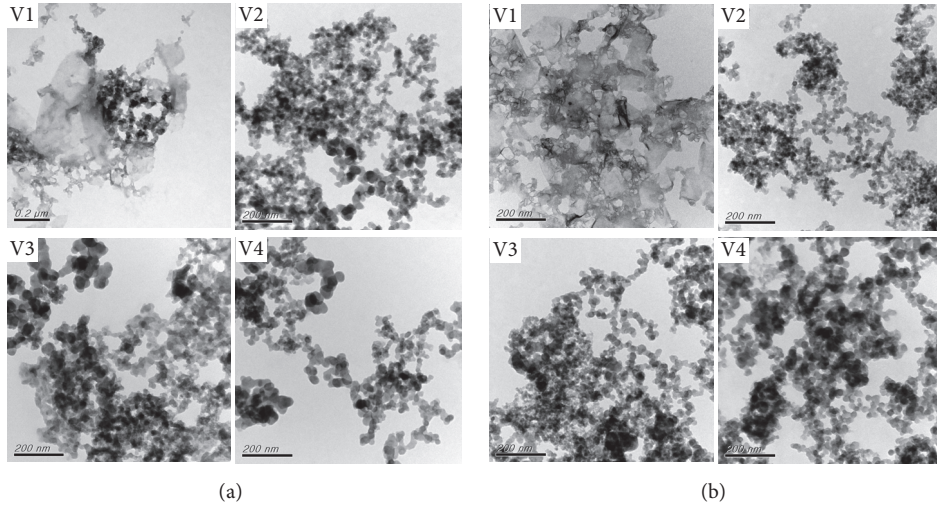


FIGURE 3: TEM images of CBNMs obtained using various process parameters for processing time durations of (a) 3 and (b) 12 min.

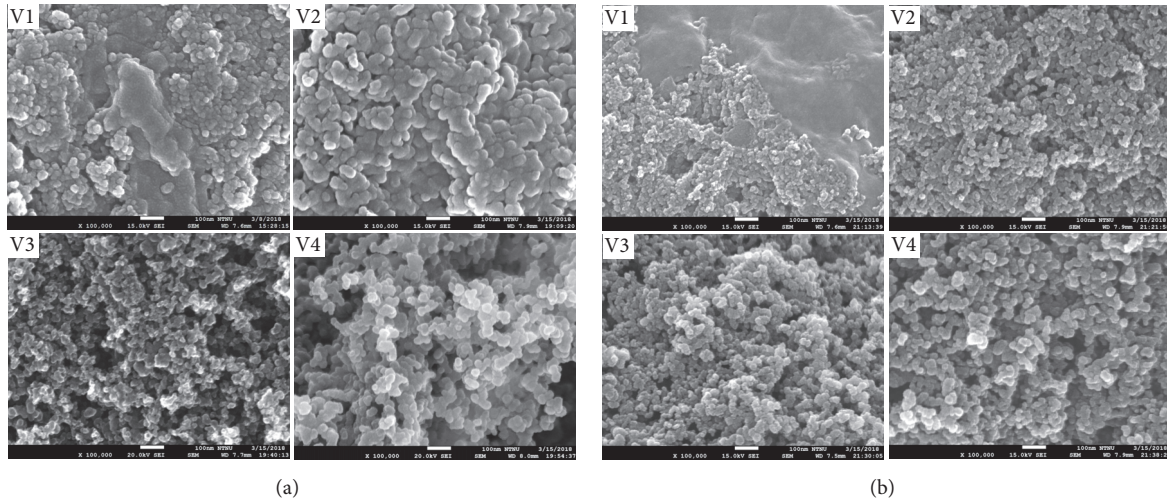


FIGURE 4: FE-SEM images of CBNMs obtained using various process parameters for processing time durations of (a) 3 and (b) 12 min.

TABLE 1: Averaged Raman spectroscopy data for the CBNFs obtained using various process parameter configurations.

Item	3 min				12 min			
	V1	V2	V3	V4	V1	V2	V3	V4
I_D								
cm^{-1}	1346.65	1336.04	1339.41	1349.34	1344.86	1337.61	1340.95	1342.19
Int.	230.48	184.43	118.52	51.25	194.21	205.81	297.88	71.23
I_G								
cm^{-1}	1592.65	1590.37	1589.41	1595.34	1589.86	1592.28	1587.61	1600.86
Int.	308.35	143.41	140.69	83.85	261.63	163.47	288.46	121.64
I_{2D}								
cm^{-1}	2639.65	2649.70	2634.74	2636.67	2651.86	2651.61	2638.95	2633.53
Int.	10.54	25.63	10.23	10.06	7.17	21.01	21.73	13.45
I_D/I_G	0.75	1.29	0.84	0.61	0.74	1.26	1.03	0.59
I_{2D}/I_G	0.03	0.18	0.07	0.12	0.03	0.13	0.08	0.11

Note. Data are the average of three measurement points for each sample.

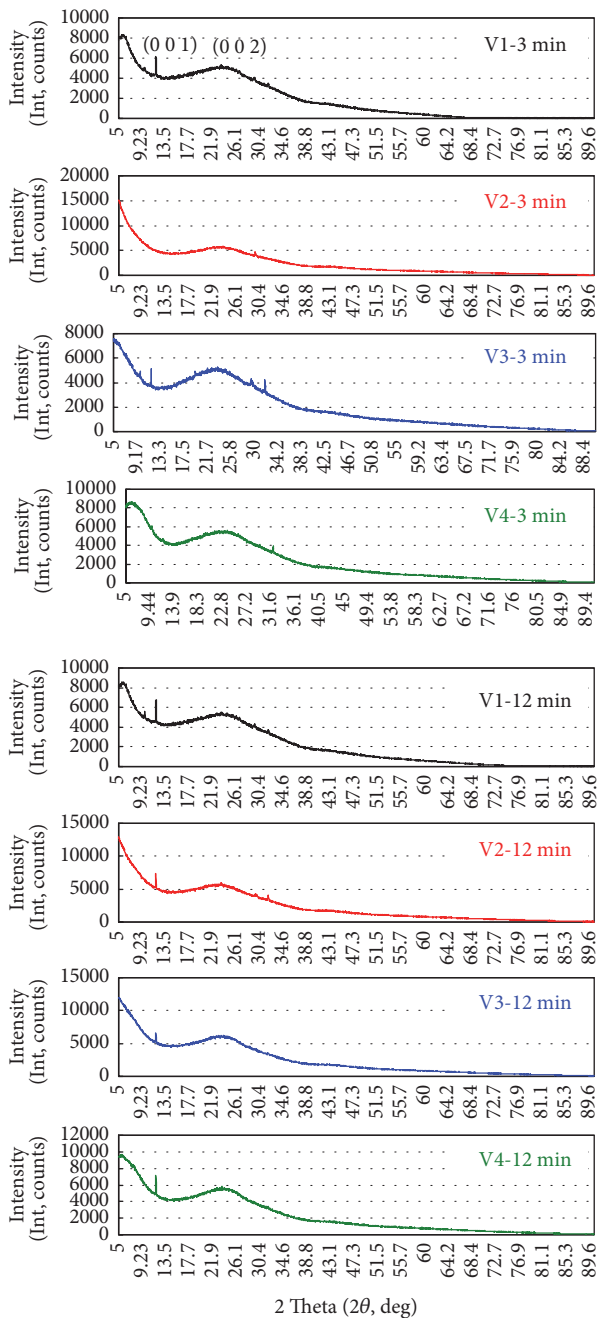


FIGURE 5: XRD patterns of CBNMs obtained using various process parameter configurations.

average data obtained from the Raman spectra for the three test points. In the Raman spectra, the D and G peaks, located at approximately $1324\text{--}1346\text{ cm}^{-1}$ and $1490\text{--}1691\text{ cm}^{-1}$, respectively, are the predominant features [7, 41–44]. In general, the spectrum of pristine graphite has a prominent G peak at 1584.5 cm^{-1} that corresponds to first-order scattering of the E_{2g} mode in the Brillouin zone. This indicates that the structure of graphite is regular [7, 42–45]. In the Raman spectrum of GO, the G peak is broadened and the D peak is prominent, thus indicating that the C=C bonds in the graphite layers are destroyed by oxidation and that several

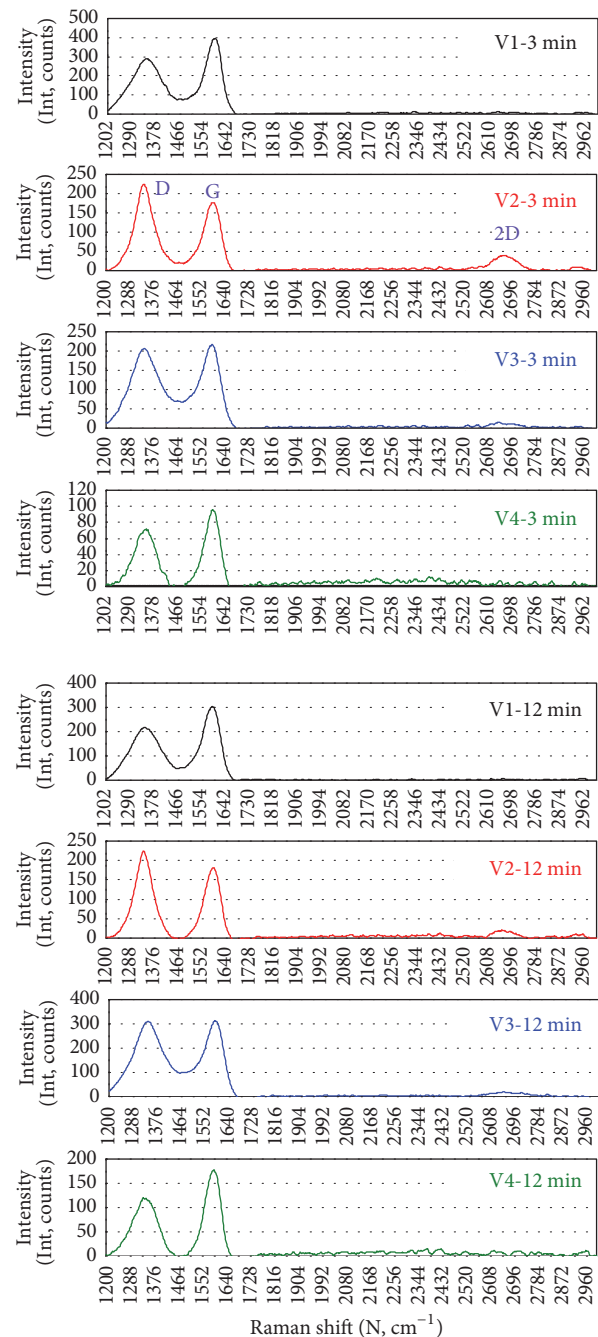


FIGURE 6: Raman spectra of CBNMs obtained using various process parameter configurations.

carbon atoms change from sp^2 - to sp^3 -hybridized carbon. The intensity I_D/I_G represents the ratio of sp^3 - and sp^2 -hybridized carbon atoms. In RGO, I_D/I_G is directly proportional to the number of sp^3 -hybridized atoms but inversely proportional to the number of sp^2 -hybridized atoms. Theoretically, I_D/I_G declines as GO is reduced to RGO. Moreover, a smaller I_D/I_G indicates more complete reduction of GO to RGO [41, 46]. However, when GO is incompletely reduced, I_D is greater than I_G . In addition, some studies have demonstrated that the reduction of GO to RGO by utilizing the chemical

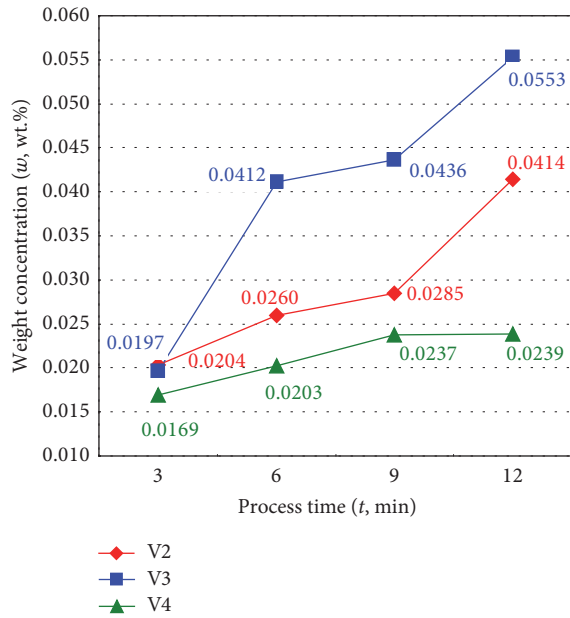


FIGURE 7: Concentrations of CBNFs obtained using various process parameter configurations.

reduction method caused an increase in I_D/I_G [47–50]. This mainly occurs because reduction increases the number of small aromatic domains in GO, leading to an increase in the I_D/I_G ratio [47]. As shown in Figure 6 and Table 1, regardless of the processing time (3 or 12 min) and parameter configuration (V1–V4), the I_D/I_G ratio first increased and then decreased (the highest I_D/I_G ratio was obtained for V2).

This phenomenon may be attributed to the decreasing O_2 ratio in the reduction flame. Reducing gases were increasingly generated due to the accumulation of combustion products. Thus, the GO reduction effect became stronger, and the proportion of RGO increased simultaneously. However, a reduction in the O_2 ratio of the reduction flame weakens the GO reduction effect by causing a decrease in the flame temperature. Moreover, the I_{2D} of GO and RGO is mostly negligible or zero. However, in this study, CBNMs should also consist of AC in terms of a clear and broad range of I_{2D} observing in the CBNMs produced by some of the process parameters. Moreover, the CBNMs contained different ratios of GO, RGO, and AC, which is inferred by simultaneously considering the Raman spectra and XRD patterns. In addition, for a specific ratio of O_2 and C_2H_2 , the processing time only affected the production rate of CBNMs (CBNF concentration).

Figure 7 displays the concentrations of the CBNMs in the CBNFs, as measured using the weighing method for V2–V4. Despite utilization of the vacuum concentration method, the weighing equipment in the authors' laboratory could not accurately detect the concentration of V1 CBNFs because this concentration was extremely low. Therefore, in the subsequent related experiments, the V1 CBNF samples were excluded. The V2, V3, and V4 configurations produced CBNM concentrations in the CBNFs of 0.0414, 0.0553, and 0.0239 wt.%, respectively, at a processing time of 12 min. The results revealed that, in addition to V4, the production rate

(concentration in the CBNF) of CBNMs and the O_2 flow rate were inversely proportional. Moreover, the production rate of all samples was directly proportional to the processing time. In the preparation procedure, the V4 configuration resulted in the most black smoke (V4 with the minimum addition of O_2) and the highest CBNM production rate, despite the production rate being lower than that when V2 and V3 were used. The V4 configuration resulted in the generation of considerable smoke and the rapid formation of numerous carbon particles that aggregated on the water surface. While the liquid was being stirred with a magnetic stirrer (stage 1), it was challenging to dissolve these floating carbon particles on the water surface, which hindered the collection efficiency. Subsequently, the carbon particles were collected efficiently by the water vortex in stage 2. However, in stages 2 and 3, obtaining suitable collection efficiency for the V4 configuration was challenging because the carbon particles generated could not be appropriately collected in stage 1. The material analysis results indicated that processing time had no influence on the material obtained. In subsequent experiments, the V2–V4 samples obtained using a processing time of 12 min were adjusted to the same concentration (0.024 wt.%) for testing and comparison.

Figure 8 displays a photograph of the experimental results obtained after 120 h of static positioning for the V2–V4 samples at various dispersant concentrations. The CBNM concentrations for V2–V4 were 0.024 wt.%, and the numbers 0–5 in each process parameter in the figure represent EP dispersant concentrations of 0, 0.05, 0.1, 0.2, 0.4, and 0.8 wt.%, respectively. As shown in Figure 8, V2-0 had the worst stability, followed by V3-0. For the sample V4-0, the difference between before and after the static positioning cannot be identified by visual inspection. Hence, a spectrometer was required to investigate the stability differences of all samples. Figure 9 plots the absorbance R_{Abs} (at a wavelength of 600 nm) of the CBNFs synthesized using the V2–V4 configurations with various concentrations of EP dispersant. The samples were statically positioned for 48 h to calculate their stability using (1). A high R_{Abs} value represents more severe sedimentation. The samples with the highest stability for the V2, V3, and V4 configurations were V2-5, V3-5, and V4-0, respectively; however, the stability enhancement had to be investigated further. Further research on the addition of different types and concentrations of dispersants should be considered. The results of XRD and Raman spectroscopy confirmed that the CBNMs prepared using V2–V4 were very similar but that EP dispersant addition had different effects on the materials' stability. This was primarily due to the particle size in the CBNMs, the pH of the CBNFs, and the interfacial effect between a CBNM and its base fluid. The estimation of suspended particle size distribution, zeta potential, and basic physicochemical characteristics requires a long time; thus, the poor stability of the samples that was observed during the measurements caused a large measurement deviation. Therefore, follow-up experiments were only performed on the samples with the highest stability for each of the V2–V4 configurations (V2-5, V3-5, and V4-0).

Figure 10 depicts the d_p distribution of V2-5, V3-5, and V4-0 and reveals that their average d_p was 771.1 (274.4 and

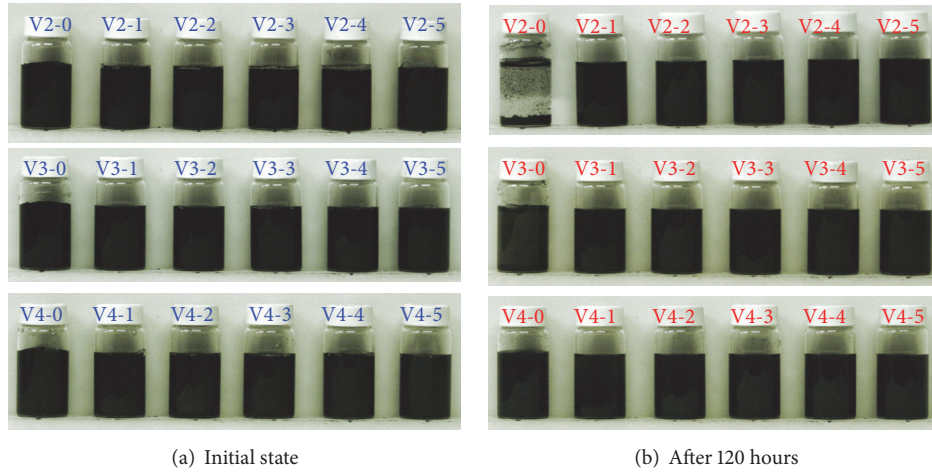


FIGURE 8: Photographs of the experimental results obtained using the static positioning method.

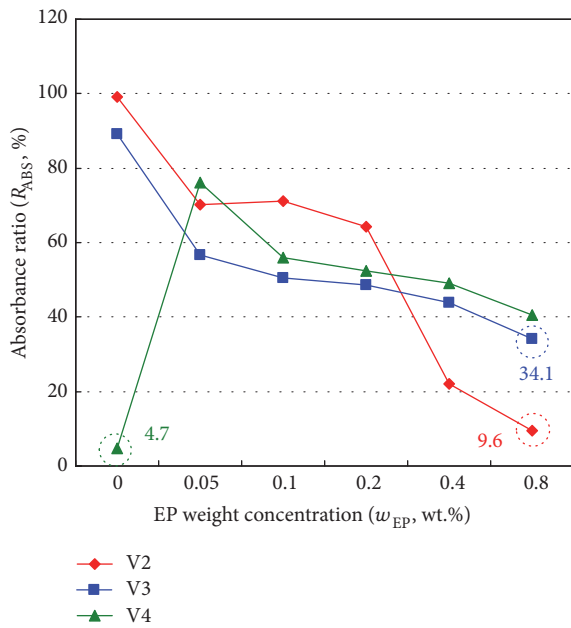


FIGURE 9: Absorbance ratios obtained using the static positioning method applied to the CBNFs obtained using various process parameter configurations.

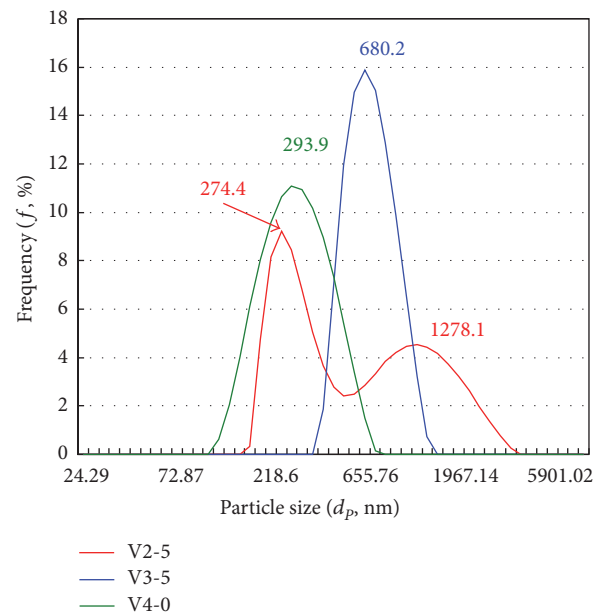


FIGURE 10: Particle size distributions of the CBNFs obtained using various process parameter configurations.

1278.1 nm), 680.2, and 293.9 nm, respectively. The results are consistent with those of the stability experiment. The minimum d_p was obtained for a V4 sample, and this sample was highly stable even when no dispersant was added. The d_p distribution for the V2 sample was a bimodal distribution, which is associated with the existence of a flaky material and causes a wide d_p distribution. Figure 10 displays only one of five test results that were obtained for the d_p distribution; the average d_p of the five test results for each sample is listed in Table 2.

Table 2 lists the average d_p , ζ , ρ , pH, E , μ , c_p , and k of the CBNFs synthesized using the various processing parameters and optimal EP dispersant concentration configurations. The values of d_p and ζ were individually measured five times, and

then the average was calculated. The lowest d_p was that of V4-0, followed by V3-5 and V2-5. Although the differences in the samples with the same configuration parameter existed, the types of d_p distribution were similar. The higher the absolute value of ζ , the better the stability of a CBNF. The highest ζ was that for V4-0, followed by V3-5 and V2-5. In general, the ζ of an NF is within the range of ± 10 to ± 30 mV, which indicates that the NF has incipient instability [35, 36]. In this experiment, CBNFs were obtained by using various process parameters. The ζ of the CBNFs and the optimal EP dispersant concentrations of the MSVTM were within the range -12.86 to -29.80 mV. The stability results indicated that the stability of these materials should be further improved. Further research will provide more details on what

TABLE 2: Basic physicochemical characteristics of the CBNFs.

Item	Experimental data						CR (%)	
	T ($^{\circ}\text{C}$)	Water	V2-5	V3-5	V4-0	V2-5	V3-5	V4-0
Mean particle size (d_p , nm)	25	—	749.56	692.05	269.90	—	—	—
Zeta potential (ζ , mV)	25	—	-12.86	-13.98	-29.80	—	—	—
Density (ρ , kg/m ³)	30	996.27	996.07	996.43	996.17	-0.02	0.02	-0.01
	40	991.87	992.97	993.00	992.70	0.11	0.11	0.08
	50	987.33	987.70	988.70	987.60	0.04	0.14	0.03
pH	30	8.00	7.29	7.06	7.17	-8.83	-11.75	-10.42
	40	7.62	7.37	7.01	7.25	-3.32	-8.05	-4.90
	50	7.56	7.38	7.26	7.33	-2.38	-3.97	-3.04
Electrical conductivity (E , $\mu\text{S}/\text{cm}$)	30	110.70	257.00	280.50	190.50	132.16	153.39	72.09
	40	113.70	261.67	285.17	193.32	130.14	150.81	70.02
	50	120.80	266.50	286.67	193.92	120.61	137.31	60.53
Viscosity (μ , mPa s)	30	0.80	0.83	0.82	0.80	4.17	2.50	0.00
	40	0.72	0.78	0.75	0.75	9.30	4.65	4.65
	50	0.65	0.70	0.73	0.65	7.69	12.82	0.70
Specific heat (c_p , kJ/kg $^{\circ}\text{C}$)	30	4.183	4.082	4.165	4.197	-2.40	-0.42	0.34
	40	4.182	4.083	4.172	4.196	-2.36	-0.24	0.33
	50	4.182	4.091	4.175	4.191	-2.17	-0.17	0.22
Thermal conductivity (k , W/m K)	30	0.618	0.615	0.623	0.622	-0.44	0.87	0.73
	40	0.629	0.643	0.633	0.638	2.21	0.56	1.29
	50	0.644	0.658	0.654	0.652	2.26	1.63	1.29

types and concentrations of dispersants can be added. Such addition can improve the stability when CBNFs are used in heat exchange systems, which require long-term stability.

The density test results for the CBNFs revealed that ρ and temperature were inversely proportional. Hence, there was no significant difference between the ρ of a CBNF and that of water (within the instrumental error) due to the low concentration of CBNM in a CBNF. The highest CRs of ρ for V2-5, V3-5, and V4-0 were, respectively, 0.11%, 0.14%, and 0.08% compared with water for the entire range of sample temperature.

The pH test results indicated that the pH of the CBNFs was lower than that of water because CO_2 dissolved in the water to form carbonic acid during the combustion process, which slightly lowered the pH of the CBNFs. The highest CRs of the pH for V2-5, V3-5, and V4-0 were -8.83%, -11.75%, and -10.42%, respectively, compared with water for the entire range of sample temperature.

Increasing the concentration of solid particles in an NF generally increases the E of that NF. Moreover, the addition of ionic dispersants (e.g., SDBS or SDS) can cause E to increase several times. The rapid movement of ions and suspended particles in NFs also increases the E of NFs at a high temperature. In this study, the EP dispersant employed was a nonionic dispersant and thus minimally affected E . The EP dispersant was less effective than an ionic dispersant

with regard to the effect of dispersant addition on E . The highest CRs of E for V2-5, V3-5, and V4-0 were 132.16%, 153.39%, and 72.09%, respectively, compared with water for the entire range of sample temperature. The experimental results revealed that the EP dispersant had a considerable effect on the E of the CBNFs. However, the effect was weaker than that of an ionic dispersant.

CBNFs have a higher μ than their base fluids (single-phase fluid) because CBNFs are solid-liquid mixtures (two-phase fluids). In general, the pressure drop and transport energy consumption in the pipeline increase as the μ of the working fluid is increased. However, most NFs are non-Newtonian fluids with shear thinning behavior, which causes μ to decrease at high flow rates or limits its increase. Consequently, rheological experiments were required to understand the relationships between μ , pressure drop, and flow rate. The highest CRs of μ for V2-5, V3-5, and V4-0 were 9.30%, 12.82%, and 4.65%, respectively, compared with water for the entire range of sample temperature.

On the basis of the concept of a solid-liquid mixture, adding a material with a c_p lower than that of water forms a suspension that has a c_p lower than that of water. The experimental results revealed that the c_p of V2-5 to V3-5 were lower than that of water; however, the c_p of V4-0 were slightly higher than that of water. This may be attributed to the EP dispersant, the solid-liquid interface, and experimental

deviation. The highest CRs of c_p for V2-5, V3-5, and V4-0 were -2.40% , -0.42% , and 0.34% , respectively, compared with water for the entire range of sample temperature.

Most studies indicate that the k of an NF is higher than that of the NF's base fluid. The k of the CBNFs in this study was slightly higher than that of water under most sample temperatures and process parameters. Nonetheless, the difference between the k of the CBNFs was small. This was primarily due to the low concentration of CBNMs and the only weak effect that the CBNFs had on the enhancement of k under instrumental deviation. The highest CRs of k for V2-5, V3-5, and V4-0 were 2.26% , 1.63% , and 1.29% , respectively, compared with water for the entire range of the sample temperature.

5. Conclusions

In this study, an MSVTM was used to fabricate CBNFs by using a one-step synthesis process. The CBNFs were synthesized using $O_2-C_2H_2$ combustion flames with different flow rate ratios of $O_2-C_2H_2$ (V1-V4). The characteristics of the CBNFs and suspended CBNMs were examined using suitable instruments and test methods. The findings of this study are summarized as follows:

- (i) The CBNMs in the CBNFs were mainly spherical. Flaky CBNMs were also observed. The d_p of the spherical CBNMs was approximately 20–50 nm. For V1-V4, the CBNMs consisted of GO, RGO, and AC.
- (ii) The CBNM production rate was affected by the processing time. Moreover, the processing time did not influence the morphology and material of CBNM. For a processing time of 12 min, the V2, V3, and V4 configurations resulted in CBNM concentrations of 0.0414, 0.0553, and 0.0239 wt.%, respectively.
- (iii) The CBNFs prepared using the V4 configuration had optimal stability without the requirement of adding an EP dispersant. The ζ of the CBNFs indicated that the materials had incipient instability ($\zeta < 30$ mV) even with the addition of the EP dispersant. Hence, further research is required on the addition of different types and concentrations of dispersants to enhance the feasibility of practical application of CBNFs.
- (iv) The highest enhancement ratios of μ for V2-5, V3-5, and V4-0 were 9.30%, 12.82%, and 4.65%, respectively, higher than that of water for the entire range of sample temperatures. In addition, addition of EP dispersant considerably increased the μ of the CBNFs.
- (v) The highest enhancement ratios of k for V2-5, V3-5, and V4-0 were 2.26%, 1.63%, and 1.29%, respectively, higher than that of water for the entire range of sample temperatures.

Conflicts of Interest

The authors declare that they have no conflicts of interest.

Authors' Contributions

Ching-Min Cheng and Shang-Pang Yu designed and planned the MSVTM. Ching-Min Cheng and Shang-Pang Yu designed the experiment and fabricated the samples. Shang-Pang Yu and Tun-Ping Teng carried out the measurements. Ching-Min Cheng, Shang-Pang Yu, and Tun-Ping Teng analyzed the measurements. Ching-Min Cheng, Shang-Pang Yu, and Tun-Ping Teng wrote and revised the paper. All authors read and approved the final manuscript.

Acknowledgments

The authors would like to thank the Ministry of Science and Technology of Republic of China (Taiwan) for their financial support to this research under Contract nos. MOST 104-2221-E-003-019-MY2 and MOST 106-2221-E-003-021-MY3.

References

- [1] V. Fuskele and R. M. Sarviya, "Recent developments in nanoparticles synthesis, preparation and stability of nanofluids," *Materials Today: Proceedings*, vol. 4, no. 2, Part A, pp. 4049–4060, 2017.
- [2] A. K. Sharma, A. K. Tiwari, and A. R. Dixit, "Rheological behaviour of nanofluids: A review," *Renewable & Sustainable Energy Reviews*, vol. 53, pp. 779–791, 2016.
- [3] S. Lee, S. U. Choi, S. Li, and J. A. Eastman, "Measuring thermal conductivity of fluids containing oxide nanoparticles," *Journal of Heat Transfer*, vol. 121, no. 2, pp. 280–289, 1999.
- [4] Babita, S. K. Sharma, and S. M. Gupta, "Preparation and evaluation of stable nanofluids for heat transfer application: A review," *Experimental Thermal and Fluid Science*, vol. 79, pp. 202–212, 2016.
- [5] N. A. Che Sidik, M. Mahmud Jamil, W. M. A. Aziz Japar, and I. Muhammad Adamu, "A review on preparation methods, stability and applications of hybrid nanofluids," *Renewable & Sustainable Energy Reviews*, vol. 80, pp. 1112–1122, 2017.
- [6] R. K. Singh, A. K. Sharma, A. R. Dixit, A. K. Tiwari, A. Pramanik, and A. Mandal, "Performance evaluation of alumina-graphene hybrid nano-cutting fluid in hard turning," *Journal of Cleaner Production*, vol. 162, pp. 830–845, 2017.
- [7] H. Yang, H. Cui, W. Tang, Z. Li, N. Han, and F. Xing, "A critical review on research progress of graphene/cement based composites," *Composites Part A: Applied Science and Manufacturing*, vol. 102, pp. 273–296, 2017.
- [8] M. N. A. W. M. Yazid, N. A. C. Sidik, and W. J. Yahya, "Heat and mass transfer characteristics of carbon nanotube nanofluids: A review," *Renewable & Sustainable Energy Reviews*, vol. 80, pp. 914–941, 2017.
- [9] N. A. C. Sidik, M. N. A. W. M. Yazid, and S. Samion, "A review on the use of carbon nanotubes nanofluid for energy harvesting system," *International Journal of Heat and Mass Transfer*, vol. 111, pp. 782–794, 2017.
- [10] R. Geetha Bai, N. Ninan, K. Muthoosamy, and S. Manickam, "Graphene: A versatile platform for nanotheranostics and tissue engineering," *Progress in Materials Science*, vol. 91, pp. 24–69, 2018.
- [11] K. Y. Leong, K. Z. Ku Ahmad, H. C. Ong, M. J. Ghazali, and A. Baharum, "Synthesis and thermal conductivity characteristic of hybrid nanofluids – A review," *Renewable & Sustainable Energy Reviews*, vol. 75, pp. 868–878, 2017.

- [12] Y. Ishida, S. Udagawa, and T. Yonezawa, "Understanding the primary and secondary aggregation states of sputtered silver nanoparticles in thiolate matrix and their immobilization in resin," *Colloids and Surfaces A: Physicochemical and Engineering Aspects*, vol. 504, pp. 437–441, 2016.
- [13] M. T. Nguyen, T. Yonezawa, Y. Wang, and T. Tokunaga, "Double target sputtering into liquid: A new approach for preparation of Ag-Au alloy nanoparticles," *Materials Letters*, vol. 171, pp. 75–78, 2016.
- [14] M. T. Nguyen, H. Zhang, L. Deng, T. Tokunaga, and T. Yonezawa, "Au/Cu Bimetallic Nanoparticles via Double-Target Sputtering onto a Liquid Polymer," *Langmuir*, vol. 33, no. 43, pp. 12389–12397, 2017.
- [15] M. Farajimotlagh, R. Poursalehi, and M. Aliofkhazraei, "Synthesis mechanisms, optical and structural properties of η - Al_2O_3 based nanoparticles prepared by DC arc discharge in environmentally friendly liquids," *Ceramics International*, vol. 43, no. 10, pp. 7717–7723, 2017.
- [16] Y. Hayashi, N. Takada, Wahyudiono, H. Kanda, and M. Goto, "Synthesis of hydrophilic carbon nanoparticles from amino acids by pulsed arc discharge over aqueous solution in argon under near-critical pressure," *The Journal of Supercritical Fluids*, vol. 120, pp. 403–407, 2017.
- [17] H. Zhang, G. Zou, L. Liu et al., "Synthesis of silver nanoparticles using large-area arc discharge and its application in electronic packaging," *Journal of Materials Science*, vol. 52, no. 6, pp. 3375–3387, 2017.
- [18] D. Amans, M. Diouf, J. Lam, G. Ledoux, and C. Dujardin, "Origin of the nano-carbon allotropes in pulsed laser ablation in liquids synthesis," *Journal of Colloid and Interface Science*, vol. 489, pp. 114–125, 2017.
- [19] G. Palazzo, G. Valenza, M. Dell'Aglio, and A. De Giacomo, "On the stability of gold nanoparticles synthesized by laser ablation in liquids," *Journal of Colloid and Interface Science*, vol. 489, pp. 47–56, 2017.
- [20] N. Krstulović, P. Umek, K. Salamon, and I. Capan, "Synthesis of Al-doped ZnO nanoparticles by laser ablation of ZnO:Al₂O₃ target in water," *Materials Research Express*, vol. 4, no. 10, 2017.
- [21] A. Sathya, S. Kalyani, S. Ranoo, and J. Philip, "One-step microwave-assisted synthesis of water-dispersible Fe₃O₄ magnetic nanoclusters for hyperthermia applications," *Journal of Magnetism and Magnetic Materials*, vol. 439, pp. 107–113, 2017.
- [22] S. Golestan, A. A. Mirzaei, and H. Atashi, "Fischer-Tropsch synthesis over an iron-cobalt-manganese (ternary) nanocatalyst prepared by hydrothermal procedure: Effects of nanocatalyst composition and operational conditions," *International Journal of Hydrogen Energy*, vol. 42, no. 15, pp. 9816–9830, 2017.
- [23] S. Golestan, A. A. Mirzaei, and H. Atashi, "Kinetic and mechanistic studies of Fischer-Tropsch synthesis over the nano-structured iron-cobalt-manganese catalyst prepared by hydrothermal procedure," *Fuel*, vol. 200, pp. 407–418, 2017.
- [24] T.-P. Teng, W.-P. Wang, and Y.-C. Hsu, "Fabrication and Characterization of Nanocarbon-Based Nanofluids by Using an Oxygen-Acetylene Flame Synthesis System," *Nanoscale Research Letters*, vol. 11, no. 1, article no. 288, 2016.
- [25] T. X. Phuoc, M. Massoudi, and R. H. Chen, "Viscosity and thermal conductivity of nanofluids containing multi-walled carbon nanotubes stabilized by chitosan," *International Journal of Thermal Sciences*, vol. 50, no. 1, pp. 12–18, 2011.
- [26] S. Harish, K. Ishikawa, E. Einarsson et al., "Enhanced thermal conductivity of ethylene glycol with single-walled carbon nanotube inclusions," *International Journal of Heat and Mass Transfer*, vol. 55, no. 13-14, pp. 3885–3890, 2012.
- [27] F.-C. Li, J.-C. Yang, W.-W. Zhou, Y.-R. He, Y.-M. Huang, and B.-C. Jiang, "Experimental study on the characteristics of thermal conductivity and shear viscosity of viscoelastic-fluid-based nanofluids containing multiwalled carbon nanotubes," *Thermochimica Acta*, vol. 556, pp. 47–53, 2013.
- [28] D. K. Agarwal, A. Vaidyanathan, and S. Sunil Kumar, "Experimental investigation on thermal performance of kerosene-graphene nanofluid," *Experimental Thermal and Fluid Science*, vol. 71, pp. 126–137, 2016.
- [29] T. Maré, S. Halefadi, O. Sow, P. Estellé, S. Duret, and F. Bazantay, "Comparison of the thermal performances of two nanofluids at low temperature in a plate heat exchanger," *Experimental Thermal and Fluid Science*, vol. 35, no. 8, pp. 1535–1543, 2011.
- [30] T.-P. Teng and C.-C. Yu, "Heat dissipation performance of MWCNTs nano-coolant for vehicle," *Experimental Thermal and Fluid Science*, vol. 49, pp. 22–30, 2013.
- [31] W.-W. Liu, S.-P. Chai, A. R. Mohamed, and U. Hashim, "Synthesis and characterization of graphene and carbon nanotubes: a review on the past and recent developments," *Journal of Industrial and Engineering Chemistry*, vol. 20, no. 4, pp. 1171–1185, 2014.
- [32] S. M. S. Murshed and C. A. Nieto De Castro, "Superior thermal features of carbon nanotubes-based nanofluids - A review," *Renewable & Sustainable Energy Reviews*, vol. 37, pp. 155–167, 2014.
- [33] N. Arora and N. N. Sharma, "Arc discharge synthesis of carbon nanotubes: comprehensive review," *Diamond & Related Materials*, vol. 50, pp. 135–150, 2014.
- [34] M.-S. Lee, J. Kim, J. Park, and J.-U. Park, "Studies on the mechanical stretchability of transparent conductive film based on graphene-metal nanowire structures," *Nanoscale Research Letters*, vol. 10, no. article no. 27, 2015.
- [35] R. Greenwood and K. Kendall, "Selection of suitable dispersants for aqueous suspensions of zirconia and titania powders using acoustophoresis," *Journal of the European Ceramic Society*, vol. 19, no. 4, pp. 479–488, 1999.
- [36] D. Hanaor, M. Michelazzi, C. Leonelli, and C. C. Sorrell, "The effects of carboxylic acids on the aqueous dispersion and electrophoretic deposition of ZrO₂," *Journal of the European Ceramic Society*, vol. 32, no. 1, pp. 235–244, 2012.
- [37] ASHRAE Inc., "Chapter 30 Thermophysical properties of refrigerants," in *2009 ASHRAE Handbook-Fundamentals (SI)*, ASHRAE Inc, 2009.
- [38] H.-J. Shin, K. K. Kim, A. Benayad et al., "Efficient reduction of graphite oxide by sodium borohydride and its effect on electrical conductance," *Advanced Functional Materials*, vol. 19, no. 12, pp. 1987–1992, 2009.
- [39] L. Zhao, X. Guo, C. Ge et al., "Investigation of the effectiveness of PC@GO on the reinforcement for cement composites," *Construction and Building Materials*, vol. 113, pp. 470–478, 2016.
- [40] J. Zhang, H. Yang, G. Shen, P. Cheng, J. Zhang, and S. Guo, "Reduction of graphene oxide vial-ascorbic acid," *Chemical Communications*, vol. 46, no. 7, pp. 1112–1114, 2010.
- [41] X. Mei, X. Meng, and F. Wu, "Hydrothermal method for the production of reduced graphene oxide," *Physica E: Low-dimensional Systems and Nanostructures*, vol. 68, pp. 81–86, 2015.
- [42] K. K. H. De Silva, H.-H. Huang, R. K. Joshi, and M. Yoshimura, "Chemical reduction of graphene oxide using green reductants," *Carbon*, vol. 119, pp. 190–199, 2017.

- [43] H. Wang, T. Maiyalagan, and X. Wang, "Review on recent progress in nitrogen-doped graphene: synthesis, characterization, and its potential applications," *ACS Catalysis*, vol. 2, no. 5, pp. 781–794, 2012.
- [44] C. Castiglioni and M. Tommasini, "Raman spectroscopy of disordered and nano-structured carbon materials: The molecular approach," *Óptica Pura y Aplicada*, vol. 40, no. 2, pp. 169–174, 2007.
- [45] F. Tuinstra and J. L. Koenig, "Raman spectrum of graphite," *The Journal of Chemical Physics*, vol. 53, no. 3, pp. 1126–1130, 1970.
- [46] W. Chen, L. Yan, and P. R. Bangal, "Preparation of graphene by the rapid and mild thermal reduction of graphene oxide induced by microwaves," *Carbon*, vol. 48, no. 4, pp. 1146–1152, 2010.
- [47] S. Stankovich, D. A. Dikin, R. D. Piner et al., "Synthesis of graphene-based nanosheets via chemical reduction of exfoliated graphite oxide," *Carbon*, vol. 45, no. 7, pp. 1558–1565, 2007.
- [48] V. C. Tung, M. J. Allen, Y. Yang, and R. B. Kaner, "High-throughput solution processing of large-scale graphene," *Nature Nanotechnology*, vol. 4, no. 1, pp. 25–29, 2009.
- [49] J. I. Paredes, S. Villar-Rodil, P. Solís-Fernández, A. Martínez-Alonso, and J. M. D. Tascón, "Atomic force and scanning tunneling microscopy imaging of graphene nanosheets derived from graphite oxide," *Langmuir*, vol. 25, no. 10, pp. 5957–5968, 2009.
- [50] S. Villar-Rodil, J. I. Paredes, A. Martínez-Alonso, and J. M. D. Tascón, "Preparation of graphene dispersions and graphene-polymer composites in organic media," *Journal of Materials Chemistry*, vol. 19, no. 22, pp. 3591–3593, 2009.

Research Article

Electronic Pulses from Pulsed Field Emission of CNT Cathodes

Xianqi Wei ^{1,2,3}, Xiaoli Wang,¹ Xin Li ^{1,4} and Weihua Liu¹

¹Department of Microelectronics, School of Electronics and Information Engineering, Xi'an Jiaotong University, Xi'an, Shaanxi 710049, China

²Science School, Huaihai Institute of Technology, Lianyungang, Jiangsu 222005, China

³Research Institute of Xi'an Jiaotong University, No. 328 Wenming Road, Xiaoshan District, Hangzhou City, Zhejiang Province 311215, China

⁴Guangdong Shunde Xi'an Jiaotong University Academy, No. 3 Deshengdong Road, Daliang, Shunde District, Foshan City, Guangdong Province 528300, China

Correspondence should be addressed to Xianqi Wei; wei.wxq@163.com

Received 14 November 2017; Revised 17 January 2018; Accepted 26 February 2018; Published 16 April 2018

Academic Editor: Haihui Ruan

Copyright © 2018 Xianqi Wei et al. This is an open access article distributed under the Creative Commons Attribution License, which permits unrestricted use, distribution, and reproduction in any medium, provided the original work is properly cited.

We presented a demonstration of infrared laser irradiated field emission electronic pulse based on carbon nanotube (CNT) cathodes. Electronic pulses greatly depended on pulsed infrared laser and were almost synchronous with laser pulses. We have designed a pulsed field emission cathode based on CNTs and investigated correlation between electronic pulse and laser pulse, acquiring the shortest width of electronic pulses about 50 ms and turn-on field less than $0.14 \text{ V}/\mu\text{m}$. Besides, we have studied the thermal effect on the pulsed field emission of CNT cathodes caused by laser heating. Interestingly, the thermal effect has caused an enhancement of emission current but resulted in a waveform distortion on short electronic pulses. The application of laser pulses on CNT cathodes would extend conventional electron sources to a pulsed electron source and offered a possibility of pulsed field emission. These results were encouraging us to prepare further studies of ultrafast electronic pulses for high-frequency electron sources.

1. Introduction

In the applications of ultrafast electron microscopy, free electron laser, satellite communication, picosecond cathodoluminescence, particle accelerators and THz vacuum microelectronics, and electron sources are limited to ultrafast electron pulses with the stringent requirements of high-power and high-frequency [1–7]. However, with the advent of electron beam from Nanometer-scale metallic tip of cathode emitters induced by femtosecond laser, conventional continuous electron sources are gradually replaced by ultrafast pulsed electron sources [8–13]. Sharp metallic tip of cathode emitters irradiated by laser pulses has represented a feasibility and implementation of the method for realizing ultrafast pulsed electron sources in recent years [14]. With the generation of pulsed electron source, much attention has been paid to explore cathode emitters of pulsed field emission in the related subjects, such as electron rescattering at sharp metallic tips, emission spectrum of laser-matter interaction, coherent field

emission images, laser acceleration of relativistic electrons, and emission mechanism [15–19]. Although conventional metallic nanotip of cathode emitters takes advantage of an electric field enhancement both in the static and optical electric field, it is certainly worth considering that the complicated process of manufacture and thermal ablation of metallic nanotips served as cathode emitters of pulsed field emission. To extend the studies on conventional metallic nanotip of cathode emitters, we studied the pulsed electron cathode emitters in a popular material of carbon nanotubes (CNTs).

The sharp apex of individual CNTs is an intrinsic property as a nanomaterial, while conventional metallic tips, for example, tungsten, gold, molybdenum, or copper, were produced by electrochemical etching [16–19]. Contrasting to the tip apex of individual CNTs, the diameter of metallic tips is much larger and has to employ a complicated manufacturing process. The nanometer-sized tip apex of CNTs and their high aspect ratio result in a strong field enhancement at the sharp tip of cathode emitter. Besides, another key advantage

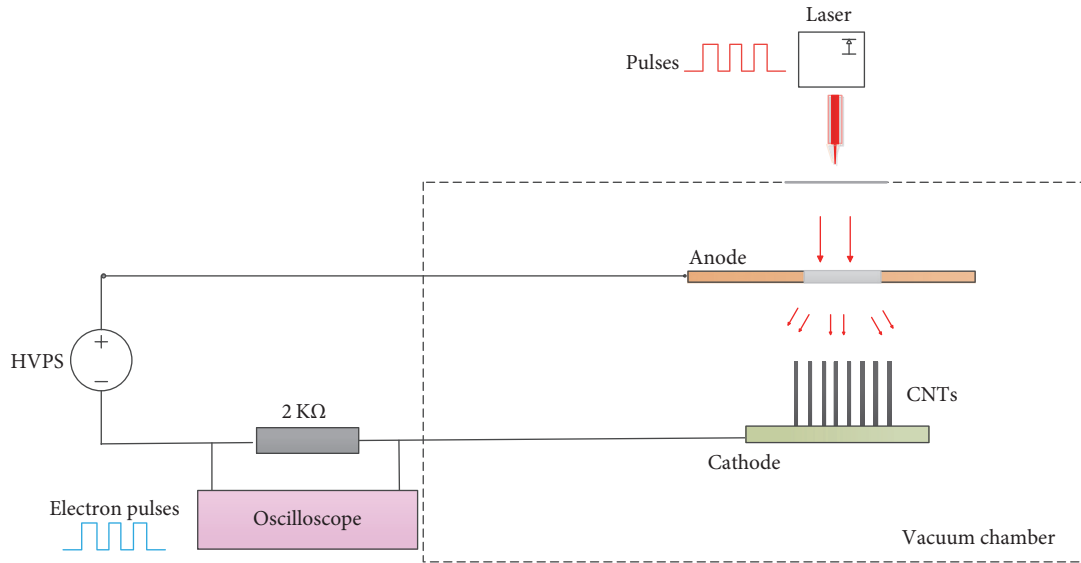


FIGURE 1: Schematic diagram of pulsed field emission system experimental set-up based on carbon nanotube (CNT) cathode emitters.

of CNTs is that of providing a new method to control surface morphology of the cathode emitters by doping with other elements on the growth process [20]. And CNTs are a desired flexibility material with the convenient and simply preparation process, which has started to receive significant interest in application of flexible display, flexible sensor, radio frequency identification, bullet-proof vest, spacesuit, wearable devices, and other smart electronic devices in comparison with metallic material [21–24]. Capitalizing on the atomic/macroscopic duality of structure of the nanotip of cathode emitters, CNTs can be modeled from an atomic point of view, unlike conventional metallic tip of cathode emitters which can only be modeled in bulk [19], giving great help to theoretical research. In this paper, we have designed a pulsed field emission system in which CNT cathodes are irradiated by pulsed laser and investigated the property of emission electronic pulses so as to gain insight into the pulsed field emission mechanism for preparing ultrafast pulsed electron source.

2. Experimental

CNTs were synthesized on SiO_2 substrate by chemical vapor deposition (CVD) using iron phthalocyanine. The detailed information about the growth of CNTs was reported in our previous research [25]. Field emission tests were performed in a vacuum chamber with pressure about 5×10^{-5} Pa. A DC bias voltage was applied between the anode and cathode to establish a static electric field by Stanford Research Systems MODEL PS325. The emission current was monitored by a Keithley 2000 multimeter or an Oscilloscope TDS 3014B. The cathodes of CNT arrays were irradiated by Ytterbium Fiber Laser to realize the pulsed field emission when the bias voltage was applied. In the experiment, we presented the pulsed field emission system based on photofield emission mechanism. Irradiating CNT cathodes with infrared laser pulses

led to pulsed field emission [10, 18, 26]. Figure 1 shows the experimental set-up of pulsed field emission system based on CNT cathodes. The output from an Ytterbium Fiber Laser was focused on the anode plate with 2 mm spot size and faced the cathode plate in an ultrahigh vacuum chamber of 5×10^{-5} Pa. The laser operated at 1 watt with a center wavelength of 1064 nm and produced a train of pulse from 50 ms to 10000 ms which could be tuned by a control panel. The CNT cathodes were mounted on the cathode plate in the ultrahigh vacuum chamber and located $350 \mu\text{m}$ away from the anode plate. The intensity and width of laser pulse which propagated through anode plate were carefully controlled by the collimation system and control panel. And then the collimated laser was used to irradiate CNT cathodes of area $2 \text{ mm} \times 2 \text{ mm}$ to excite electrons by absorbing photons for emitting electronic pulses, when the applied voltage was on.

3. Results and Discussions

In field emission, electron emission happens when the tip bias voltage of cathode emitters is sufficiently large for electrons in the vicinity of Fermi-level to tunnel through the barrier. By applying a bias voltage to the tip of cathode emitters, a tunneling barrier is formed and tunneling electron emission occurs. In the photofield emission, electrons are excited to an intermediate state by one or several photons absorption and subsequent tunneling through the surface barrier into vacuum by field emission, when a laser irradiates the cathodes [14, 19, 26, 27]. Figure 2 shows electronic pulses curve from the pulsed field emission of CNT cathodes, when the width of laser pulses (defined as the pulse-on T_1) and off-time interval (defined as the pulse-off T_2) are both 10000 ms. Interestingly, the width of electronic pulses is also 10000 ms or so, almost synchronous with laser pulses. The average amplitude of electronic pulses is 0.027 mA/cm^2 and the fluctuation is less than 20% on applied voltage of 50 V. More important, the

TABLE 1: Amplitude ($I_{\text{on}} - I_{\text{off}}$) of electronic pulses on applied voltage of 50 V, 100 V, 400 V, 700 V, and 1000 V, respectively. $T_1 = T_2 = 10000$ ms.

Voltage (V)	50	100	400	700	1000
Amplitude (mA/cm^2) $I_{\text{on}} - I_{\text{off}}$	0.23	0.53	1.05	0.45	≈ 0

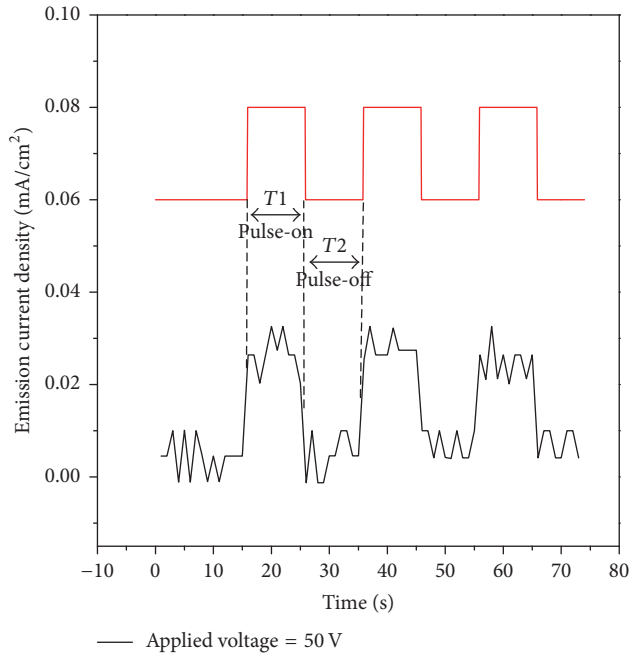


FIGURE 2: Plot of field emission electronic pulses on CNT cathodes irradiated by pulsed laser, on applied voltage of 50 V. Black line represents the emission electronic pulse profile with width of 10000 ms ($T_1 = T_2$). Red line represents a train of laser pulses with the width of 10000 ms.

emission current density is nearly zero on laser pulse-off with applied voltage of 50 V, proving that electron emissions are excited only on the condition of laser pulse-on (T_1). The preliminary results show the realization of electron emission pulses from CNT cathodes and turn-on electric field less than $0.14 \text{ V}/\mu\text{m}$ (turn-on electric field is defined as the electric field required to produce a current density of $0.01 \text{ mA}/\text{cm}^2$), which is incomparable with reference to previous studies, such as CNTs on nickel foam ($0.53 \text{ V}/\mu\text{m}$) [28], graphene-CNT ($0.73 \text{ V}/\mu\text{m}$) [29], CNTs on silicon pillars ($2.16 \text{ V}/\mu\text{m}$) [30], and multilayer graphene-CNTs ($0.93 \text{ V}/\mu\text{m}$) [31]. Actually, the turn-on voltage of the CNT cathodes was about 80 V ($0.23 \text{ V}/\mu\text{m}$) by field emission. On applied voltage of 50 V ($0.14 \text{ V}/\mu\text{m}$), electron emission would not happen if without laser. This result definitely proved the photofield emission mechanism of which electrons were excited to an intermediate state by laser and subsequently tunneled through barrier into vacuum by field emission.

Figure 3 shows electronic pulses curve from pulsed field emission of CNT cathodes irradiated by laser pulses, on the same working condition of laser pulses except different applied voltage of 100 V, 400 V, 700 V, and 1000 V, respectively, contrasting to the insert of emission current density of cathodes without laser illumination by field emission without laser illumination. With applied voltage increase,

the amplitude ($I_{\text{on}} - I_{\text{off}}$) of electronic pulses increases on lower applied voltage of 100 V and 400 V, as shown in Figures 3(a) and 3(b). However, the amplitude decreases with the applied voltage continuously increasing to 700 V and 1000 V, as shown in Figures 3(c) and 3(d). The corresponding values of amplitude are listed in Table 1. I_{on} is the average amplitude of emission electronic pulses on electron pulse-on, and I_{off} is the average valley value on electron pulse-off. The electronic pulses signals appear obviously on low applied voltages, while the pulses cannot be distinguished on the high applied voltage of 1000 V ($I_{\text{on}} - I_{\text{off}} \approx 0$). Interestingly, the amplitude of $I_{\text{on}} - I_{\text{off}}$ increases firstly and then decreases until electronic pulses signals are gradually buried in the DC signal of emission current with applied voltage continuous increase, as showed in Table 1. Practically, the emission current of fabricated CNT cathodes was the result of the combined effect of infrared laser and applied voltage but not the simple sum of emission current caused by photofield emission and field emission. On low applied voltage, photofield emission was dominated in emission process, and applied voltage just narrowed the potential barrier in the vicinity of threshold. On high voltages, emission mechanism was dominated by conventional field emission rather than pulsed field emission. Nevertheless, the laser field instantaneously wiggled the barrier. Emission electrons caused by laser pulses just led to a fluctuation for emission current of the field emission. With the applied voltage continuing to increase, emission electrons caused by laser pulses could be ignored due to being too weak comparing with emission current caused by the field emission. The obtained results helped to understand and realize the emission mechanism of pulsed field emission from CNT cathode.

To increase the frequency of electronic pulses, shortening the period of electronic pulses is one of popular methods for pulsed field emission as an ultrafast pulsed electron source, especially in decreasing width of electronic pulses. Figure 4 shows electronic pulses curve from CNT cathodes irradiated by the laser pulse of $T_1 = 50$ ms, while T_2 are 1000 ms and 100 ms, respectively. The results showed the width of electronic pulses was about 50 ms, and electronic pulse-off was 1000 ms as shown in Figure 4(a) and 100 ms in Figure 4(b), respectively. However, pulse broadening was obviously observed as shown in Figure 4(b). For the further study, the response time was investigated, and the results showed the pulse broadening arose from the thermal effect. Thermal effect which came from laser heating up tips of CNT cathodes existed in the pulsed field emission and could enhance the emission current. By virtue of the very fast sampling rate of 2.5 GS/s, oscilloscope was used to detect response time of electronic pulses. Figure 5 shows a single electronic pulse with the laser pulse-on of $T_1 = 5000$ ms and applied voltage of 400 V. It is found that emission current increases sharply when the laser pulse of $T_1 = 5000$ ms is on and remarkably drops down when the laser pulse is off. Moreover, the evolution process of emission current is not instantaneous on

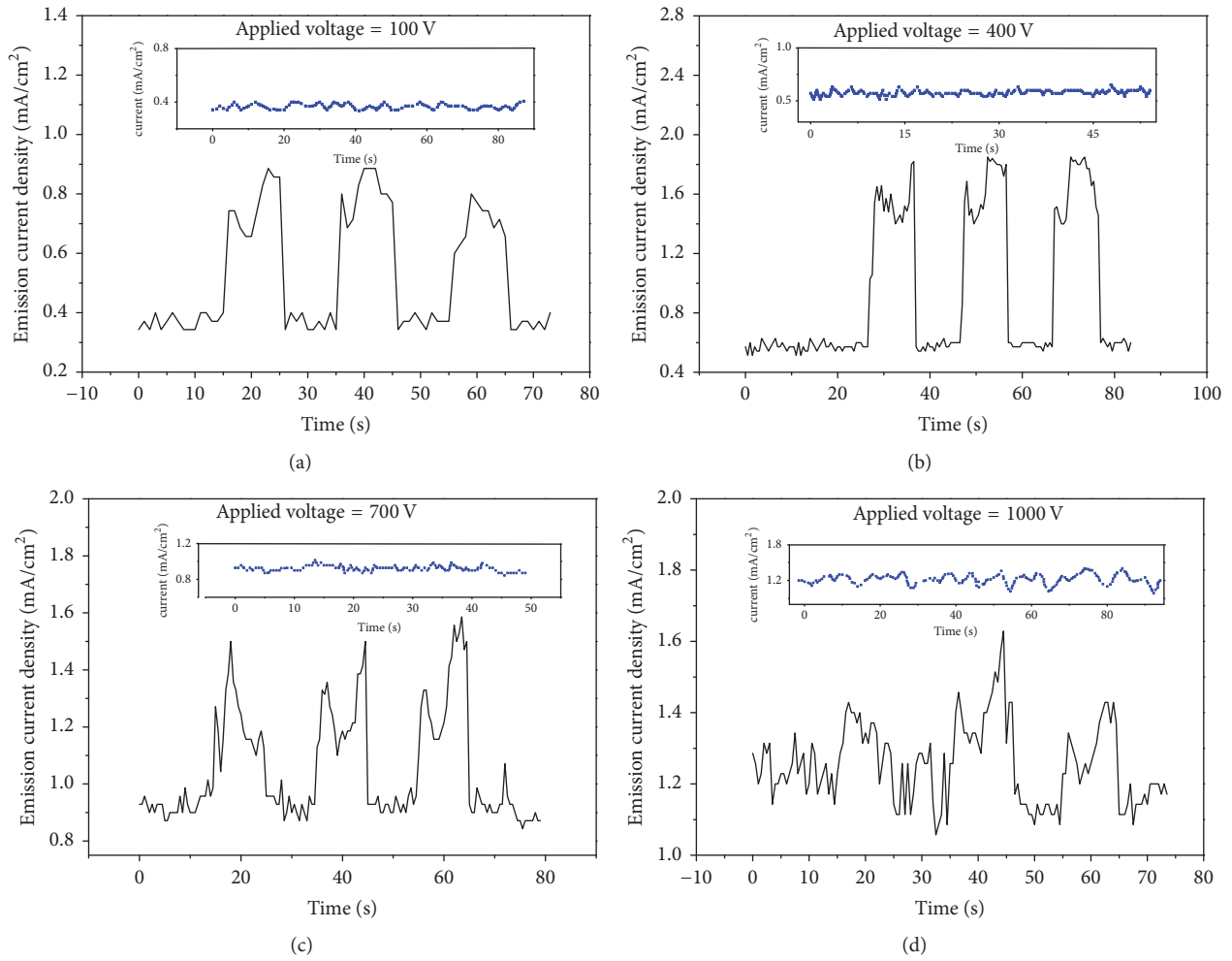


FIGURE 3: (Black line) Plots of field emission electronic pulses profile on CNT cathodes irradiated by pulsed laser on different applied voltage of 100 V, 400 V, 700 V, and 1000 V, respectively. The width of emission electronic pulse is 10000 ms. The laser working condition is that the pulse width of T_1 and laser pulse-off of T_2 are both 10000 ms. The insert (blue squares) is corresponding to the emission current density without laser illumination by field emission.

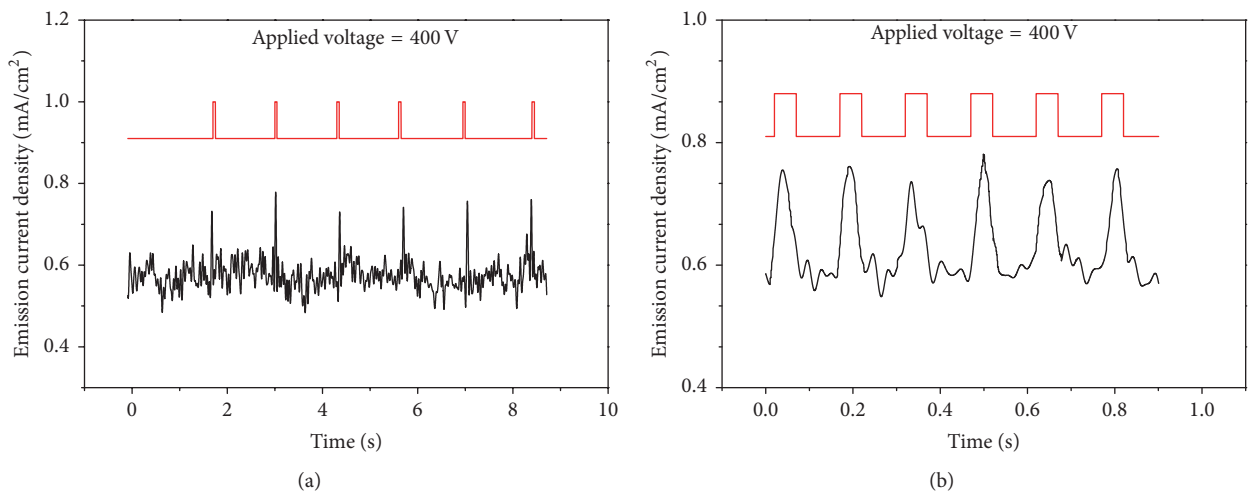


FIGURE 4: (Black line) Plots of field emission electronic pulses profile with the width of 50 ms on CNT cathodes irradiated by pulsed laser on 400 V ($T_1 \neq T_2$). (a) T_1 width of laser pulses (red line) is 50 ms and T_2 is 1000 ms. (b) T_1 width is 50 ms and T_2 is 100 ms.

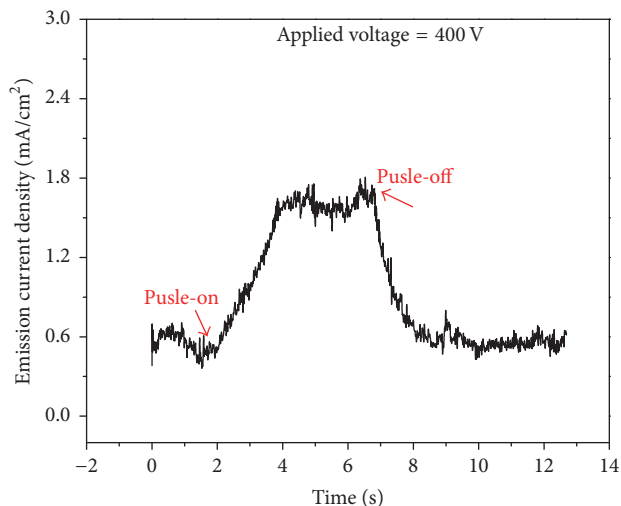


FIGURE 5: Plot of one period of electronic pulse from pulsed field emission of CNT cathodes irradiated by pulsed laser of 400 V ($T_1 = 5000$ ms, $T_2 = 10000$ ms).

laser pulse-on and pulse-off. The rise time of emission current jumping to plateau takes 2 s or so when laser pulse is on, and the fall time spends more than 2 s when laser pulse is off. Besides, the amplitude is much higher than that of value in Figure 4 on the same applied voltage 400 V. Working conditions of the electronic pulse in Figure 4 ($T_1 = 50$ ms; $T_2 = 1000$ ms, 100 ms) and Figure 5 ($T_1 = 5000$ ms; $T_2 = 10000$ ms) are mainly associated with T_1 and T_2 of laser pulses on the same applied voltage, but the amplitudes are quite different. Irradiating of the CNT cathodes by laser pulses heated the tips and caused the apex electron temperature to evolve periodically in time [9], so thermally enhanced field emission increased drastically obeying laser excitation and caused the pulse broadening.

A major reason for pulse broadening was thermal effect which played an important role in the field emission mechanism, especially in short electronic pulses occurring. In Figure 5, the electronic pulse had enough time to reach to the saturation value on laser pulse-on of $T_1 = 5000$ ms. However, electronic pulses were compelled to drop down before reaching to the saturation value on the short laser pulse-on of $T_1 = 50$ ms in Figure 4(b) and compelled to rise up before dropping to the valley value on condition of $T_2 = 100$ ms. After repeatedly verifying, the optimum working condition of laser pulse irradiated CNT cathodes was that the laser pulse-off T_2 was greater than or equal to 2 times the laser pulse-on T_1 for realizing ultrafast electronic pulses. These results showed that thermal effect enhanced the pulsed field emission of CNT cathodes irradiating by pulsed infrared laser and resulted in a pulse broadening especially on short electronic pulses.

4. Conclusion

Irradiating CNT cathodes with laser pulses led to pulsed field emission. We investigated the emission electronic pulses from

pulsed field emission of carbon nanotube (CNT) cathodes by tuning the pulsed laser field and attained the short electronic pulses of 50 ms and turn-on field below 0.14 V/ μ m. With the applied voltage increase, electronic pulses amplitude increased firstly and then decreased till it was gradually buried in the emission current. With the width of electronic pulses decrease, pulse broadening existed in the pulsed field emission caused by thermal effect which played an important role in the field emission mechanism, especially in short electronic pulses occurring. To reduce the electronic pulse distortion, the optimum working condition of laser pulse irradiated CNT cathodes was $T_2 \geq T_1$ for realizing short electronic pulses. These results extended conventional electron sources and provided a possibility of realizing ultrashort electronic pulses as a high-frequency electron source.

Conflicts of Interest

The authors declare that they have no conflicts of interest.

Acknowledgments

This work was financially supported by grants from the National Natural Science Foundation of China (nos. 91123018, 51625504, and 61671368), Shaanxi Natural Science Foundation (2014JM7277), Science and Technology Planning Project of Zhejiang Province, China (2017C31087), and Science and Technology Planning Project of Guangdong Province, China (2017A010103004).

References

- [1] V. Ortolan and A. H. Zewail, "4D scanning transmission ultrafast electron microscopy: single-particle imaging and spectroscopy," *Journal of the American Chemical Society*, vol. 133, no. 28, pp. 10732–10735, 2011.
- [2] A. Adhikari, J. K. Eliason, J. Sun, R. Bose, D. J. Flannigan, and O. F. Mohammed, "Four-dimensional ultrafast electron microscopy: insights into an emerging technique," *ACS Applied Materials & Interfaces*, vol. 9, no. 1, pp. 3–16, 2017.
- [3] R. Bormann, S. Strauch, S. Schäfer, and C. Ropers, "An ultrafast electron microscope gun driven by two-photon photoemission from a nanotip cathode," *Journal of Applied Physics*, vol. 118, no. 17, Article ID 173105, pp. 1108–1116, 2015.
- [4] J. P. Hall, F. E. Poynton, P. M. Keane et al., "Monitoring one-electron photo-oxidation of guanine in DNA crystals using ultrafast infrared spectroscopy," *Nature Chemistry*, vol. 7, no. 12, pp. 961–967, 2015.
- [5] H. Yoneda, Y. Inubushi, K. Nagamine et al., "Atomic inner-shell laser at 1.5-ångström wavelength pumped by an X-ray free-electron laser," *Nature*, vol. 524, no. 7566, pp. 446–449, 2015.
- [6] C. Behrens, F.-J. Decker, Y. Ding et al., "Few-femtosecond time-resolved measurements of X-ray free-electron lasers," *Nature Communications*, vol. 5, pp. 3762–3769, 2014.
- [7] J. Duris, P. Musumeci, M. Babzien et al., "High-quality electron beams from a helical inverse free-electron laser accelerator," *Nature Communications*, vol. 5, pp. 4928–4935, 2014.
- [8] B. D. Patterson, R. Abela, H.-H. Braun et al., "Coherent science at the SwissFEL x-ray laser," *New Journal of Physics*, vol. 12, pp. 035012–035029, 2010.

- [9] C. Kealhofer, S. M. Foreman, S. Gerlich, and M. A. Kasevich, "Ultrafast laser-triggered emission from hafnium carbide tips," *Physical Review B: Condensed Matter and Materials Physics*, vol. 86, no. 3, Article ID 035405, pp. 165–173, 2012.
- [10] C. Ropers, D. R. Solli, C. P. Schulz, C. Lienau, and T. Elsaesser, "Localized multiphoton emission of femtosecond electron pulses from metal nanotips," *Physical Review Letters*, vol. 98, no. 4, pp. 043907–043912, 2007.
- [11] J. Hoffrogge, J. Paul Stein, M. Krüger et al., "Tip-based source of femtosecond electron pulses at 30 keV," *Journal of Applied Physics*, vol. 115, no. 9, pp. 094506–094515, 2014.
- [12] W. Luo, T. P. Yu, M. Chen et al., "Generation of bright attosecond X-ray pulse trains via Thomson scattering from laser-plasma accelerators," *Optics Express*, vol. 22, pp. 32098–32106, 2014.
- [13] Y. Jiang, L. C. Liu, H. M. Müller-Werkmeister et al., "Femtosecond electron diffraction study of the spin crossover dynamics of single crystal $[\text{Fe}(\text{PM-AzA})_2](\text{NCS})_2$," *Ultrafast Phenomena XIX*, vol. 162, pp. 283–286, 2015.
- [14] M. Krüger, M. Schenk, M. Förster, and P. Hommelhoff, "Attosecond physics in photoemission from a metal nanotip," *Journal of Physics B: Atomic, Molecular and Optical Physics*, vol. 45, no. 7, pp. 074006–074012, 2012.
- [15] T. Qi, L. Dong, Y. Qiao et al., "Enhanced electron field emission of Cu implanted microcrystalline diamond films after annealing," *Vacuum*, vol. 134, pp. 141–149, 2016.
- [16] X. Q. Yang, Y. Hu, J. L. Zhang, Y. Q. Wang, C. M. Pei, and F. Liu, "Preparation of boron nanowires using AuPd nanoparticles as catalyst and their field emission behaviors," *Acta Physica Sinica*, vol. 63, pp. 048102–048191, 2014.
- [17] S. Tsujino, F. Le Pimpec, J. Raabe et al., "Static and optical field enhancement in metallic nanotips studied by two-photon photoemission microscopy and spectroscopy excited by picosecond laser pulses," *Applied Physics Letters*, vol. 94, no. 9, pp. 093508–093512, 2009.
- [18] B. Piglosiewicz, S. Schmidt, D. J. Park et al., "Carrier-envelope phase effects on the strong-field photoemission of electrons from metallic nanostructures," *Nature Photonics*, vol. 8, no. 1, pp. 37–42, 2014.
- [19] M. R. Bionta, B. Chalopin, A. Masseboeuf, and B. Chatel, "First results on laser-induced field emission from a CNT-based nanotip," *Ultramicroscopy*, vol. 159, pp. 152–155, 2015.
- [20] B. A. Kakade, V. K. Pillai, D. J. Late et al., "High current density, low threshold field emission from functionalized carbon nanotube bucky paper," *Applied Physics Letters*, vol. 97, no. 7, pp. 073102–073105, 2010.
- [21] P. Ilanchezhian, A. S. Zakirov, G. M. Kumar et al., "Highly efficient CNT functionalized cotton fabrics for flexible/wearable heating applications," *RSC Advances*, vol. 5, no. 14, pp. 10697–10702, 2015.
- [22] S. Huang, C. Zhao, W. Pan, Y. Cui, and H. Wu, "Direct writing of half-meter long CNT based fiber for flexible electronics," *Nano Letters*, vol. 15, no. 3, pp. 1609–1614, 2015.
- [23] Z. Ahmad, K. S. Karimov, and F. Touati, "Flexible impedance and capacitive tensile load Sensor based on CNT composite," *Chinese Physics B*, vol. 25, no. 2, pp. 028801–028806, 2016.
- [24] R. Kumar, R. K. Singh, D. P. Singh, A. R. Vaz, R. R. Yadav, and C. S. Rout, "Synthesis of self-assembled and hierarchical palladium-CNTs-reduced graphene oxide composites for enhanced field emission properties," *Mater & Design*, vol. 122, pp. 110–117, 2017.
- [25] X. Wei, Y. Zhu, X. Xia, X. Wang, W. Liu, and X. Li, "Carbon nanotube cathodes covered on the cylindrical surface of a fiber," *RSC Advances*, vol. 5, no. 22, pp. 17049–17053, 2015.
- [26] P. G. Chavan, S. S. Badadhe, I. S. Mulla, M. A. More, and D. S. Joag, "Synthesis of single crystalline CdS nanocombs and their application in photo-sensitive field emission switches," *Nanoscale*, vol. 3, no. 3, pp. 1078–1083, 2011.
- [27] P. Hommelhoff, Y. Sortais, A. Aghajani-Talesh, and M. A. Kasevich, "Field emission tip as a nanometer source of free electron femtosecond pulses," *Physical Review Letters*, vol. 96, no. 7, Article ID 077401, pp. 077401–077405, 2006.
- [28] M. Song, P. Xu, L. Han et al., "Enhanced field-emission performance from carbon nanotube emitters on nickel foam cathodes," *Journal of Electronic Materials*, vol. 45, no. 4, pp. 2299–2304, 2016.
- [29] J.-H. Deng, G.-A. Cheng, R.-T. Zheng et al., "Catalyst-free, self-assembly, and controllable synthesis of graphene flake-carbon nanotube composites for high-performance field emission," *Carbon*, vol. 67, pp. 525–533, 2014.
- [30] H. S. Uh and S. Park, "Improved field emission properties from carbon nanotubes grown onto micron-sized arrayed silicon pillars with pyramidal bases," *Diamond and Related Materials*, vol. 54, no. 1, pp. 74–78, 2015.
- [31] J.-H. Deng, B. Yu, G.-Z. Li et al., "Self-assembled growth of multi-layer graphene on planar and nano-structured substrates and its field emission properties," *Nanoscale*, vol. 5, no. 24, pp. 12388–12393, 2013.

Research Article

Vibration Analysis of Bilayered Graphene Sheets for Building Materials in Thermal Environments Based on the Element-Free Method

Zhengtian Wu,¹ Yang Zhang,² Fuyuan Hu ,¹ Qing Gao ,³
Xinyin Xu,¹ and Ronghao Zheng⁴

¹School of Electronic and Information Engineering, Suzhou University of Science and Technology, Suzhou 215009, China

²School of Science, Nanjing University of Science and Technology, Nanjing 210094, China

³Institute for Automatic Control and Complex Systems (AKS), Faculty of Engineering, University of Duisburg-Essen, Duisburg, Germany

⁴College of Electrical Engineering, Zhejiang University, Hangzhou 310027, China

Correspondence should be addressed to Fuyuan Hu; fuyuanhu@mail.usts.edu.cn and Qing Gao; qing.gao.chance@gmail.com

Received 26 September 2017; Revised 12 December 2017; Accepted 16 January 2018; Published 11 April 2018

Academic Editor: Chengyuan Wang

Copyright © 2018 Zhengtian Wu et al. This is an open access article distributed under the Creative Commons Attribution License, which permits unrestricted use, distribution, and reproduction in any medium, provided the original work is properly cited.

Graphene sheets are widely applied due to their unique and highly valuable properties, such as energy conservation materials in buildings. In this paper, we investigate the vibration behavior of double layer graphene sheets (DLGSs) in thermal environments which helps probe into the mechanism of energy conservation of graphene sheets in building materials. The nonlocal elastic theory and classical plate theory (CLPT) are used to derive the governing equations. The element-free method is employed to analyze the vibration behaviors of DLGSs embedded in an elastic medium. The accuracy of the solutions in this study is demonstrated by comparison with published results in the literature. Furthermore, a number of numerical results are presented to investigate the effects of various parameters (boundary conditions, nonlocal parameter, aspect ratio, side length, elastic foundation parameter, and temperature) on the frequency of DLGSs.

1. Introduction

In 2004, Novoselov and Geim in [1], physicists at the University of Manchester, successfully stripped off graphene sheets from the graphite. Graphene sheets (GSs) have carbon atomic structure of the monolayer or multilayer atomic thickness. DLGSs in which the interlayer width is 0.34 nm [2] have specific chemical, mechanical, thermal, and electronic properties [3–10] and have been applied as constituent in nanoelectromechanical systems (NEMS) and microelectromechanical systems (MEMS). DLGSs used in these applications generally rest on the elastic medium rather than being suspended. Due to the increasing applications of graphene sheets, understanding the vibration of DLGSs embedded in the elastic media is essential to optimize the design and manufacture in engineering.

Applications of DLGSs depend on clear knowledge of their mechanical behavior. In recent years, world-wide researchers have engaged in the study of GSs using experimental, numerical, and theoretical tools. However, it is of difficulty to carry out experimental research due to the very small dimensions of the nanostructure elements [11]. Thus, theoretical research is becoming increasingly important for studying nanostructures. The theoretical tools can be divided into three categories [12]: atomistic modeling, continuum mechanics (CM), and the hybrid method. Generally, the atomistic modeling consists of classic tight-binding molecular dynamics (TBMD) and molecular dynamics (MD). Mirparizi and Aski [13] studied the interlayer shear effect on vibrational behavior for DLGSs using the MD simulation. Gajbhiye and Singh [14] studied the nonlinear frequency response of SLGSs via the atomistic finite element method

(FEM). The MD simulation is still the most sophisticated and reliable approach which provides deep insight into nanomaterials and their properties. However, MD simulation is limited to the analysis of GSs with few atoms and time scales because of high computational cost. Thus, unlike MD simulations, the CM has a lower computational cost [15] and has been adopted by numerous researchers to deal with nanoscale structures. Therefore, some relatively large nanostructures can be analyzed by this method [16, 17]. The classical continuum approach is however a kind of scale-free theory which cannot account for the small scale effect arising in the nanostructures. Therefore, the mechanical behavior of nanostructures cannot be successfully captured by the classical continuum approach. It behooves us to modify the classical continuum model which can describe precise mechanical behaviors of the nanostructures. Some improved continuum methods such as couple stress theory [18], surface elasticity theory [19], nonlocal theory, and strain gradient theory [20] were used in the simulation of the size-dependent materials. It is found that the nonlocal theory has provided good matching results compared with lattice dynamics. Recent literature indicates that the theory of nonlocal elasticity is being increasingly used [21–23]. Peddieson et al. [24] were the first ones who adopted the nonlocal elasticity theory to analyze the static deformation behavior of Euler-Bernoulli nanobeams. Duan and Wang [25] firstly formulated the nonlocal continuum plate model to study the small scale effect in the bending regarding circular nanoplates. Dastjerdi and Jabbarzadeh [26] studied the multilayer orthotropic circular GSs nonlinear bending using nonlocal elasticity theory. Liew et al. [27] investigated the effect of polymer matrix on the vibration response of GSs. Zhang et al. [12] studied the free vibration behaviors of DLGSs employing nonlocal elasticity theory. Zhang et al. [28] analyzed the vibration of quadrilateral graphene sheets subjected to an in-plane magnet using nonlocal elasticity theory. Pradhan and Phadikar [29] conducted the vibration analysis of double-layered GSs resting on a polymer matrix utilizing the nonlocal continuum mechanics. Malekzadeh et al. [21] investigated the small scale effect on the thermal buckling characteristic of orthotropic arbitrary straight-sided quadrilateral nanoplates embedded in an elastic medium. Asemi et al. [30] presented an axisymmetric buckling analysis of circular SLGS using Eringen's theory. Additionally, Asemi et al. [31] used nonlocal theory of Eringen to simulate postbuckling response of orthotropic SLGS.

Numerical techniques are important for theoretical analysis. Various numerical tools have been utilized to analyze the mechanical behaviors of nanostructure [32, 33]. Ansari et al. [34] proposed a nonlocal FEM model to simulate the vibration behaviors of multilayered GSs based on the Mindlin plate theory. As a numerical technique, the meshless method has been successfully applied in solving engineering problems. Because of its advantage of not relying on elements, it has good adaptability [35–39].

In this work, we study the vibration behavior of DLGSs resting on a Pasternak elastic medium employing the nonlocal theory and established the meshless framework to obtain the solution. The effects of nonlocal parameter, temperature,

aspect ratio, side length, stacking types, and foundation parameters on the vibration frequency of DLGSs are examined. Additionally, the accuracy of the solutions in this study is demonstrated through comparison with published results in the literature.

2. Nonlocal Elasticity Theory and Model of Elastic Medium

2.1. Nonlocal Elasticity Theory. Eringen [36] proposed the nonlocal theory through experiment and the theoretical analysis in which the stress depends on the strain of all the points in the domain. Therefore, it can reflect the small scale effect. The most widely applied constitutive relation of the differential form is written as

$$\left[1 - (e_0 a)^2 \nabla^2\right] \sigma_{ij}(x) = C_{ijkl} \varepsilon_{kl}(x), \quad (1)$$

in which $e_0 a$ is the nonlocal parameter and ∇^2 is the Laplacian operator defined by $\nabla^2 = \partial^2/\partial x^2 + \partial^2/\partial y^2$.

2.2. Model of Elastic Medium. In nanoscale devices, vibration behaviors can be observed, which affect the performance significantly. As mentioned above, graphene based products are usually resting on an elastic medium. In the present study, the Pasternak-type foundation [40] is adopted. Pasternak-type foundation model is modeled with two parameters. The mathematical expressions of Pasternak-type foundation are written as

$$q_{\text{pasternak}} = k_w w - k_g \nabla^2 w, \quad (2)$$

where k_w is the Winker modulus and k_g is the shear modulus.

2.3. Temperature Field Distribution Type. In this paper, the temperature field can be divided into three types as linear, nonlinear, and uniform. The temperature changes along the thickness of the GSs. The temperature change obeys the following law [22]:

$$\Delta T(z) = \left(\frac{z + h/2}{z}\right)^\varphi T, \quad -\frac{h}{2} \leq z \leq \frac{h}{2}, \quad (3)$$

where φ is the temperature distribution coefficient. When $\varphi > 1$, there is a nonlinear temperature distribution along the thickness of the GSs; for $\varphi = 1$ we have a linear temperature distribution, for $\varphi = 0$ the temperature distribution is uniform, and the temperature change is $T = T_b - T_r$, where T_b is the temperature value when the buckling occurs, while T_r is the referent temperature. The thermal load caused by temperature change satisfies the following formulation:

$$\begin{aligned} N_T &= -\frac{\alpha E}{1-\nu} \int_{-h/2}^{h/2} \left(\frac{z + h/2}{z}\right)^\varphi T dz \\ &= -\frac{\alpha h E}{(1-\nu)(1+\varphi)} T. \end{aligned} \quad (4)$$

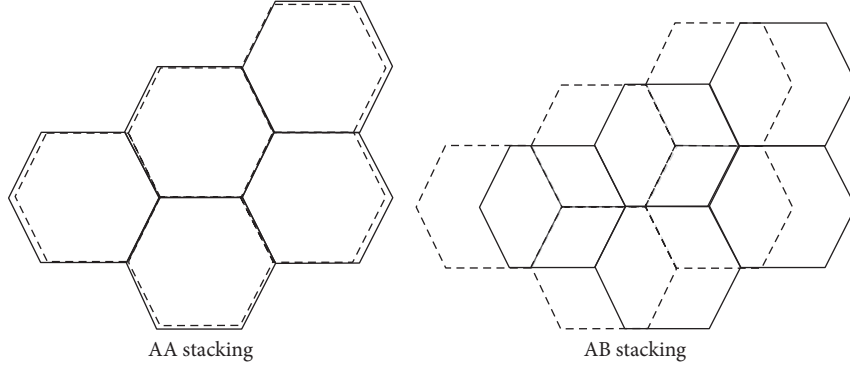


FIGURE 1: Two stacking types of DLGSs.

3. Theoretical Approach

3.1. The Van der Waals (vdW) Force Expression. In DLGSs, the interaction force between layers is the vdW force which is a nonbonded interaction. By neglecting the nonlinear terms, the vdW's interaction can be expressed as [41]

$$q_{ij} = c_{ij}(w_i - w_j), \quad i, j = 1, 2 \quad (5)$$

in which c_{ij} represents the vdW coefficient. Generally, DLGSs consist of two types in terms of the relative positions of the upper and lower layers. The one with the upper graphene layer stacking directly on lower layer is called AA-type whereas the other is called AB-type [41]. Figure 1 depicts these two categories of DLGSs. According to [41], the vdW coefficient is

$$\begin{aligned} c_{ij} &= -27.3546 \text{ Gpa/nm} \quad (\text{for AA-type}), \\ c_{ij} &= -146.8247 \text{ Gpa/nm} \quad (\text{for AB-type}). \end{aligned} \quad (6)$$

If there is no special description, the vdW coefficient is taken as AB-type in the following simulations.

3.2. Governing Equations. The DLGSs resting on elastic foundation are demonstrated in Figure 2 in which they are in the thermal condition. The external foundation is modeled as Pasternak-type. L_x and L_y , respectively, denote the length and width of GSs. The thickness of graphene is h . Transverse displacements of the top-GSs and bottom-GSs for the buckling analysis are represented by $w_1(x, y, t)$ and $w_2(x, y, t)$, respectively.

The displacement field of DLGSs according to CLPT can be written as

$$\begin{aligned} u(x, y, z; t) &= \frac{-z\partial w_1(x, y; t)}{\partial x} \\ v(x, y, z; t) &= \frac{-z\partial w_1(x, y; t)}{\partial y} \\ w(x, y, z; t) &= w_1(x, y; t) \end{aligned} \quad (7)$$

in which (u, v, w) , respectively, denote the displacements along the axes (x, y, z) . w_1 is the displacement along z -axis of a mid-plane material point. According to the strain-displacement relations

$$\varepsilon_{1xx} = \frac{-z\partial^2 w_1(x, y; t)}{\partial x^2} \quad (8)$$

$$\varepsilon_{1yy} = \frac{-z\partial^2 w_1(x, y; t)}{\partial y^2} \quad (9)$$

$$\gamma_{1xy} = \frac{-2z\partial^2 w_1(x, y; t)}{\partial x\partial y} \quad (10)$$

$$\varepsilon_{1zz} = \gamma_{1xz} = \gamma_{1yz} = 0 \quad (11)$$

the constitutive relationship is given by

$$\begin{aligned} & \left[1 - (e_0 a)^2 \nabla^2 \right] \begin{Bmatrix} \sigma_{1xx} \\ \sigma_{1yy} \\ \sigma_{1xy} \end{Bmatrix} \\ &= \begin{bmatrix} \frac{E}{(1-\nu^2)} & \frac{\nu E}{(1-\nu^2)} & 0 \\ \frac{\nu E}{(1-\nu^2)} & \frac{E}{(1-\nu^2)} & 0 \\ 0 & 0 & G \end{bmatrix} \begin{bmatrix} \varepsilon_{1xx} - \alpha\Delta T \\ \varepsilon_{1yy} - \alpha\Delta T \\ \varepsilon_{1xy} \end{bmatrix}, \end{aligned} \quad (12)$$

where $G = E/2(1 + \nu)$.

According to (10), the nonlocal moments can be written as

$$\begin{aligned} & \left[1 - (e_0 a)^2 \nabla^2 \right] M_{1xx} \\ &= -D \left(\frac{\partial^2 w_1(x, y; t)}{\partial x^2} + \frac{\nu \partial^2 w_1(x, y; t)}{\partial y^2} \right), \end{aligned} \quad (13)$$

$$\begin{aligned} & \left[1 - (e_0 a)^2 \nabla^2 \right] M_{1yy} \\ &= -D \left(\frac{\partial^2 w_1(x, y; t)}{\partial y^2} + \frac{\nu \partial^2 w_1(x, y; t)}{\partial x^2} \right), \end{aligned} \quad (14)$$

$$\left[1 - (e_0 a)^2 \nabla^2 \right] M_{1xy} = \frac{-D(1-\nu)\partial^2 w_1(x, y; t)}{\partial x\partial y}, \quad (15)$$

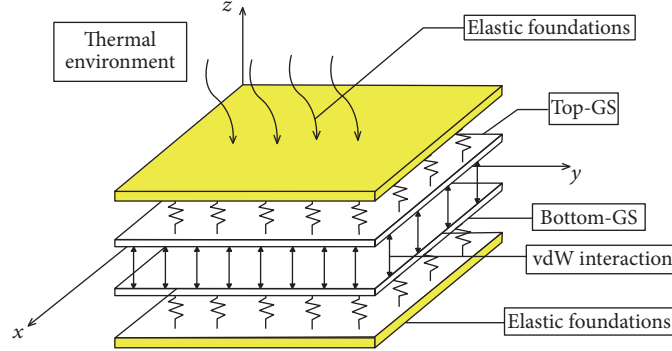


FIGURE 2: DLGSs resting on Pasternak-type elastic foundation under thermal environment.

where $(M_{1xx}, M_{1yy}, M_{1xy}) = \int (\sigma_{1xx}, \sigma_{1yy}, \sigma_{1xy})z dz$. D is the bending stiffness of the plate and $D = Eh^3/12(1 - \nu^2)$.

With the principle of virtual work, the equilibrium equation can be derived as

$$\begin{aligned} & -M_{1xx,xx} - M_{1yy,yy} - 2M_{1xy,xy} - q_{12} + k_w w_1 \\ & - k_g \nabla^2 w_1 - N_T \nabla^2 w_1 - I_2 (\ddot{w}_{1,xx} + \ddot{w}_{1,yy}) \\ & + I_0 \ddot{w}_1 = 0. \end{aligned} \quad (16)$$

From (11)–(13), we can get

$$\begin{aligned} & -D \nabla^4 w_1 \\ & = [1 - (e_0 a)^2 \nabla^2] (M_{1xx,xx} + M_{1yy,yy} + 2M_{1xy,xy}). \end{aligned} \quad (17)$$

Substituting (17) into (16), the governing equation can be written as

$$\begin{aligned} & D \nabla^4 w_1 + [1 - (e_0 a)^2 \nabla^2] [-q_{12} + k_w w_1 - k_g \nabla^2 w_1 \\ & - N_T \nabla^2 w_1 - I_2 (\ddot{w}_{1,xx} + \ddot{w}_{1,yy}) + I_0 \ddot{w}_1]. \end{aligned} \quad (18)$$

Similarly, we can obtain the governing equation of bottom-GSs

$$\begin{aligned} & D \nabla^4 w_2 + [1 - (e_0 a)^2 \nabla^2] [-q_{21} + k_w w_2 - k_g \nabla^2 w_2 \\ & - N_T \nabla^2 w_2 - I_2 (\ddot{w}_{2,xx} + \ddot{w}_{2,yy}) + I_0 \ddot{w}_2]. \end{aligned} \quad (19)$$

4. Discretized System Equations

4.1. Weak Form. In order to get the weak form, the equilibrium equation is multiplied by the virtual displacement δw . Therefore, we obtain

$$\begin{aligned} & \int_{\Omega} \delta w_1 (D \nabla^4 w_1 + [1 - (e_0 a)^2 \nabla^2] (-q_{12} + k_w w_1 \\ & - N_T \nabla^2 w_1 - k_g \nabla^2 w_1 + I_0 \ddot{w}_1 \\ & - I_2 (\ddot{w}_{1,xtt} + \ddot{w}_{1,ytt}))) dx dy = 0. \end{aligned} \quad (20)$$

Equation (20) can be integrated by parts as

$$\begin{aligned} & D \int_{\Omega} (w_{1,xx} \delta w_{1,xx} + w_{1,yy} \delta w_{1,yy} \\ & + 2w_{1,xy} \delta w_{1,xy}) dx dy - c \int_{\Omega} (w_1 \delta w_1 \\ & - w_2 \delta w_1) \int_{\Omega} (w_{1,xx} \delta w_{1,xx} + w_{1,yy} \delta w_{1,yy} \\ & + 2w_{1,xy} \delta w_{1,xy}) dx dy \\ & + k_w \int_{\Omega} w_1 \delta w_1 \int_{\Omega} (w_{1,xx} \delta w_{1,xx} + w_{1,yy} \delta w_{1,yy} \\ & + 2w_{1,xy} \delta w_{1,xy}) dx dy + (e_0 a)^2 \\ & \cdot k_w \int_{\Omega} (w_{1,x} \delta w_{1,x} + w_{1,y} \delta w_{1,y}) \int_{\Omega} (w_{1,xx} \delta w_{1,xx} \\ & + w_{1,yy} \delta w_{1,yy} + 2w_{1,xy} \delta w_{1,xy}) dx dy \\ & + N_T \int_{\Omega} w_{1,x} \delta w_{1,x} \int_{\Omega} (w_{1,xx} \delta w_{1,xx} + w_{1,yy} \delta w_{1,yy} \\ & + 2w_{1,xy} \delta w_{1,xy}) dx dy - c (e_0 a)^2 \\ & \cdot \int_{\Omega} (w_{1,x} \delta w_{1,x} + w_{1,y} \delta w_{1,y}) \int_{\Omega} (w_{1,xx} \delta w_{1,xx} \\ & + w_{1,yy} \delta w_{1,yy} + 2w_{1,xy} \delta w_{1,xy}) dx dy \\ & + (e_0 a)^2 N_T \int_{\Omega} (w_{1,xx} \delta w_{1,xx} + w_{1,xy} \delta w_{1,xy}) \\ & \cdot \int_{\Omega} (w_{1,xx} \delta w_{1,xx} + w_{1,yy} \delta w_{1,yy} \\ & + 2w_{1,xy} \delta w_{1,xy}) dx dy + c (e_0 a)^2 \\ & \cdot \int_{\Omega} (w_{2,x} \delta w_{1,x} + w_{2,y} \delta w_{1,y}) \int_{\Omega} (w_{1,xx} \delta w_{1,xx} \\ & + w_{1,yy} \delta w_{1,yy} + 2w_{1,xy} \delta w_{1,xy}) dx dy \end{aligned}$$

$$\begin{aligned}
& + k_g \int_{\Omega} (w_{1,x} \delta w_{1,x} + w_{1,y} \delta w_{1,y}) \int_{\Omega} (w_{1,xx} \delta w_{1,xx} \\
& + w_{1,yy} \delta w_{1,yy} + 2w_{1,xy} \delta w_{1,xy}) dx dy \\
& + (e_0 a)^2 \int_{\Omega} I_0 (\delta w_{1,x} w_{1,xtt} + \delta w_{1,y} w_{1,ytt}) \\
& + I_2 (\delta w_{1,xx} w_{1,xtt} + 2\delta w_{1,xy} w_{1,xytt} \\
& + \delta w_{1,yy} w_{1,ytt}) \int_{\Omega} (w_{1,xx} \delta w_{1,xx} + w_{1,yy} \delta w_{1,yy} \\
& + 2w_{1,xy} \delta w_{1,xy}) dx dy + (e_0 a)^2 \\
& \cdot N_T \int_{\Omega} (w_{1,xy} \delta w_{1,xy} + w_{1,yy} \delta w_{1,yy}) \\
& \cdot \int_{\Omega} (w_{1,xx} \delta w_{1,xx} + w_{1,yy} \delta w_{1,yy} \\
& + 2w_{1,xy} \delta w_{1,xy}) dx dy \\
& + N_T \int_{\Omega} w_{1,y} \delta w_{1,y} \int_{\Omega} (w_{1,xx} \delta w_{1,xx} + w_{1,yy} \delta w_{1,yy} \\
& + 2w_{1,xy} \delta w_{1,xy}) dx dy + k_g (e_0 a)^2 \\
& \cdot \int_{\Omega} (w_{1,xx} \delta w_{1,xx} + w_{1,yy} \delta w_{1,yy} + 2w_{1,xy} \delta w_{1,xy}) \\
& \cdot \int_{\Omega} (w_{1,xx} \delta w_{1,xx} + w_{1,yy} \delta w_{1,yy} \\
& + 2w_{1,xy} \delta w_{1,xy}) dx dy \\
& + \int_{\Omega} [I_0 \delta w_1 w_{1,tt} + I_2 (\delta w_{1,x} w_{1,xtt} + \delta w_{1,y} w_{1,ytt})] \\
& \cdot \int_{\Omega} (w_{1,xx} \delta w_{1,xx} + w_{1,yy} \delta w_{1,yy} \\
& + 2w_{1,xy} \delta w_{1,xy}) dx dy - (e_0 a)^2 \\
& \cdot k_w \int_{\Gamma} (w_{1,x} \delta w_{1,n_x} - w_{1,y} \delta w_{1,n_y}) ds \\
& - N_T \int_{\Gamma} w_{1,x} \delta w_{1,n_x} ds + N_T \int_{\Gamma} w_{1,y} \delta w_{1,n_y} ds \\
& + (e_0 a)^2 N_T \int_{\Gamma} (w_{1,xxx} \delta w_{1,n_x} - w_{1,xx} \delta w_{1,x} n_x \\
& + w_{1,xyy} \delta w_{1,n_x} + w_{1,xy} \delta w_{1,x} n_y) ds + (e_0 a)^2 \\
& \cdot N_T \int_{\Gamma} (w_{1,xyy} \delta w_{1,n_x} + w_{1,xy} \delta w_{1,x} n_y \\
& - w_{1,yyy} \delta w_{1,n_y} + w_{1,yy} \delta w_{1,y} n_y) ds \\
& + k_g (e_0 a)^2 \int_{\Gamma} (w_{1,xxx} \delta w_{1,n_x} - w_{1,xx} \delta w_{1,x} n_x \\
& - w_{1,yyy} \delta w_{1,n_y} + w_{1,yy} \delta w_{1,y} n_y + 2w_{1,xyy} \delta w_{1,n_x} \\
& + 2w_{1,xy} \delta w_{1,x} n_y) ds + D \int_{\Gamma} (w_{1,xxx} \delta w_{1,n_x} \\
& - w_{1,xx} \delta w_{1,x} n_x - w_{1,yyy} \delta w_{1,n_y} + w_{1,yy} \delta w_{1,y} n_y \\
& + 2w_{1,xyy} \delta w_{1,n_x} + 2w_{1,xy} \delta w_{1,x} n_y) ds \\
& + c (e_0 a)^2 \int_{\Gamma} (w_{1,y} \delta w_{1,n_y} - w_{1,x} \delta w_{1,n_x} \\
& + w_{2,x} \delta w_{1,n_x} - w_{2,y} \delta w_{1,n_y}) ds \\
& + k_g \int_{\Gamma} (w_{1,y} \delta w_{1,n_y} - w_{1,x} \delta w_{1,n_x}) ds - (e_0 a)^2 \\
& \cdot I_0 \int_{\Gamma} (w_{1,xtt} \delta w_{1,n_x} - w_{1,ytt} \delta w_{1,n_y}) ds \\
& \cdot I_2 \int_{\Gamma} (w_{1,ytt} \delta w_{1,n_y} - w_{1,xtt} \delta w_{1,n_x}) ds + (e_0 a)^2 \\
& \cdot I_2 \int_{\Gamma} (w_{1,xxx} \delta w_{1,n_x} - w_{1,xtt} \delta w_{1,x} n_x \\
& - w_{1,yyy} \delta w_{1,n_y} + w_{1,ytt} \delta w_{1,y} n_y \\
& + 2w_{1,xyy} \delta w_{1,n_x} + 2w_{1,xy} \delta w_{1,x} n_y) ds = 0.
\end{aligned} \tag{21}$$

Equation (19) has the following weak form:

$$\begin{aligned}
& \int_{\Omega} \delta w_2 (D\nabla^4 w_2 + [1 - (e_0 a)^2 \nabla^2]) (-q_{21} + k_w w_2 \\
& - N_T \nabla^2 w_2 - k_g \nabla^2 w_2 + I_0 \ddot{w}_2 \\
& - I_2 (\ddot{w}_{2,xtt} + \ddot{w}_{2,ytt})) dx dy = 0
\end{aligned} \tag{22}$$

Equation (22) can be dealt with similarly.

4.2. Element-Free Discretization Technique. Using M values of the scattered particles ($\mathbf{x}_1, \mathbf{x}_2, \dots, \mathbf{x}_M$) to express the displacement field of SLGSs based on the kernel particle Ritz method [42] results in

$$\begin{bmatrix} w_1 \\ w_2 \end{bmatrix} = \sum_{I=1}^M \psi_I(x, y) \begin{bmatrix} w_{1I} \\ w_{2I} \end{bmatrix}. \tag{23}$$

where m is the number of nodes. w_I and ψ_I , respectively, denote the displacement value and the shape function regarding node I . We write the shape function as

$$\psi_I = C(\mathbf{x}; \mathbf{x} - \mathbf{x}_I) \Phi(\mathbf{x} - \mathbf{x}_I). \tag{24}$$

Herein, $C(\mathbf{x}; \mathbf{x} - \mathbf{x}_I)$ is the coefficient function and $\Phi(\mathbf{x}; \mathbf{x} - \mathbf{x}_I)$ represents the kernel function. $C(\mathbf{x}; \mathbf{x} - \mathbf{x}_I)$ can be expressed as

$$\begin{aligned} C(\mathbf{x}; \mathbf{x} - \mathbf{x}_I) &= \mathbf{H}^T(\mathbf{x} - \mathbf{x}_I) \mathbf{B}(\mathbf{x}), \\ \mathbf{H}^T(\mathbf{x} - \mathbf{x}_I) &= [1, x - x_I, y - y_I, (x - x_I)(y - y_I), \\ &\quad (x - x_I)^2, (y - y_I)^2]^T, \\ \mathbf{B}(\mathbf{x}) &= [k_0(x, y), k_1(x, y), k_2(x, y), k_3(x, y), \\ &\quad k_4(x, y), k_5(x, y)]^T, \end{aligned} \quad (25)$$

where \mathbf{H} denotes the vector of the quadratic basis and \mathbf{B} represents the function of \mathbf{x} . Thus, we have

$$\Psi_I(\mathbf{x}; \mathbf{x} - \mathbf{x}_I) = \mathbf{B}^T(\mathbf{x}) \mathbf{H}(\mathbf{x} - \mathbf{x}_I) \Phi(\mathbf{x} - \mathbf{x}_I), \quad (26)$$

satisfying the shape function to reproduction conditions resulting in

$$\sum_{I=1}^M \Psi_I(x) x_I^p y_I^q \quad \text{for } p + q = 0, 1, 2. \quad (27)$$

Coefficient $\mathbf{B}(\mathbf{x})$ has the following form:

$$\mathbf{B}(\mathbf{x}) = \mathbf{M}^{-1}(\mathbf{x}) \mathbf{H}(\mathbf{0}), \quad (28)$$

where

$$\begin{aligned} \mathbf{M}(\mathbf{x}) &= \sum_{I=1}^M \mathbf{H}(\mathbf{x} - \mathbf{x}_I) \Phi(\mathbf{x} - \mathbf{x}_I), \\ \mathbf{H}(\mathbf{0}) &= [1, 0, 0, 0, 0, 0]^T. \end{aligned} \quad (29)$$

We have the kernel function

$$\Phi(\mathbf{x} - \mathbf{x}_I) = \Phi(x; x_I) \cdot \Phi(y; y_I), \quad (30)$$

where

$$\Phi(x; x_I) = \phi\left(\frac{|x - x_I|}{a_I}\right). \quad (31)$$

The cubic spline function is used in the present study

$$\phi(s_1) = \begin{cases} \frac{2}{3} - 4s_1^2 + 4s_1^3 & \text{for } 0 \leq s_1 \leq \frac{1}{2} \\ \frac{4}{3} - 4s_1 + 4s_1^2 - \frac{4}{3}s_1^3 & \text{for } \frac{1}{2} \leq s_1 \leq 1 \\ 0 & \text{otherwise,} \end{cases} \quad (32)$$

where $s_1 = |x - x_I|/a_I$, $a_I = a(x_I)$ are the dilation parameters. a_I can be expressed as $a_I = d_{\max} c_I$, where d_{\max} denotes the scaling factor ranging between 2 and 4. To ensure that the support area contains numerous enough nodes to prevent the matrix \mathbf{M} from singularity, the factor should be selected appropriately. c_I denotes the larger distances.

4.3. *Discrete System Equations.* Where $N_T = -T(\alpha h E)/[(1 - \nu)(1 + \varphi)]$ and substituting (21) into (16), the discrete equation can be expressed as

$$\mathbf{M}_{11} \ddot{\mathbf{w}}_1 + (\mathbf{k}_{11} + \mathbf{k}_T) \mathbf{w}_1 + \mathbf{k}_{12} \mathbf{w}_2 = \mathbf{0}, \quad (33)$$

where

$$\mathbf{M}_{11} = \mathbf{M}_{11}^l + \mathbf{M}_{11}^n, \quad (34)$$

$$\mathbf{M}_{11}^l = \int_{\Omega} (I_0 \psi_I \psi_J + I_2 [N_1^I]^T [N_1^J]) d\Omega, \quad (35)$$

$$\begin{aligned} \mathbf{M}_{11}^n &= \int_{\Omega} (e_0 a)^2 (I_0 [N_1^I]^T [N_1^J] + [N_2^I]^T \mathbf{I} [N_2^J]) d\Omega, \end{aligned} \quad (36)$$

$$\mathbf{k}_{11} = \mathbf{k}_{11}^l + \mathbf{k}_{11}^n + \mathbf{k}_{\text{medium}}, \quad (37)$$

$$\mathbf{k}_{11}^l = \int_{\Omega} [N_2^I]^T \mathbf{L}_D [N_2^J] - c \psi_I \psi_J d\Omega, \quad (38)$$

$$\mathbf{k}_{11}^n = \int_{\Omega} -c (e_0 a)^2 [N_1^I]^T [N_1^J] d\Omega, \quad (39)$$

$$\mathbf{k}_{\text{medium}} = \int_{\Omega} [N_4^I]^T \mathbf{L}_G [N_4^J] + [N_3^I]^T \mathbf{L}_w [N_3^J] d\Omega, \quad (40)$$

$$\mathbf{k}_{12} = \mathbf{k}_{12}^l + \mathbf{k}_{12}^n, \quad (41)$$

$$\mathbf{k}_{12}^l = \int_{\Omega} c \psi_I \psi_J d\Omega, \quad (42)$$

$$\mathbf{k}_{12}^n = \int_{\Omega} c (e_0 a)^2 [N_1^I]^T [N_1^J] d\Omega, \quad (43)$$

$$\mathbf{k}_T = \int_{\Omega} [N_4^I]^T L_T [N_4^J] d\Omega. \quad (44)$$

Similarly, we can obtain

$$\mathbf{M}_{22} \ddot{\mathbf{w}}_2 + \mathbf{k}_{21} \mathbf{w}_1 + (\mathbf{k}_{22} + \mathbf{k}_T) \mathbf{w}_2 = \mathbf{0} \quad (45)$$

$$\mathbf{M}_{11} = \mathbf{M}_{22}, \quad (46)$$

$$\mathbf{k}_{21} = \mathbf{k}_{21}^l + \mathbf{k}_{21}^n, \quad (47)$$

$$\mathbf{k}_{21}^l = \int_{\Omega} c \psi_I \psi_J d\Omega, \quad (48)$$

$$\mathbf{k}_{21}^n = \int_{\Omega} c (e_0 a)^2 [N_1^I]^T [N_1^J] d\Omega, \quad (49)$$

$$\mathbf{k}_{22} = \mathbf{k}_{22}^l + \mathbf{k}_{22}^n + \mathbf{k}_{\text{medium}}, \quad (50)$$

$$\mathbf{k}_{22}^l = \int_{\Omega} [N_2^I]^T \mathbf{L}_D [N_2^J] - c \psi_I \psi_J d\Omega, \quad (51)$$

$$\mathbf{k}_{22}^n = \int_{\Omega} -c (e_0 a)^2 [N_1^I]^T [N_1^J] d\Omega, \quad (52)$$

$$\mathbf{L}_T = \frac{-\alpha h E T}{(1-\nu)(1+\varphi)} \begin{bmatrix} 1 & 0 & 0 & 0 & 0 \\ 0 & (e_0 a)^2 & & & \\ & & 2(e_0 a)^2 & & \\ & & & 1 & \\ & & & & (e_0 a)^2 \end{bmatrix}, \quad (53)$$

$$\mathbf{I} = \begin{bmatrix} I_2 & 0 & 0 \\ 0 & 2I_2 & 0 \\ 0 & 0 & I_2 \end{bmatrix},$$

$$\mathbf{L}_D = \begin{bmatrix} D & 0 & 0 \\ 0 & 2D & 0 \\ 0 & 0 & D \end{bmatrix}, \quad (54)$$

$$\mathbf{L}_w = \begin{bmatrix} k_w & 0 & 0 \\ 0 & (e_0 a)^2 k_w & 0 \\ 0 & 0 & (e_0 a)^2 k_w \end{bmatrix},$$

$$\mathbf{L}_G = \begin{bmatrix} k_g & 0 & 0 & 0 & 0 \\ 0 & k_g (e_0 a)^2 & 0 & 0 & 0 \\ 0 & 0 & 2k_g (e_0 a)^2 & 0 & 0 \\ 0 & 0 & 0 & k_g & 0 \\ 0 & 0 & 0 & 0 & k_g (e_0 a)^2 \end{bmatrix}, \quad (55)$$

$$[N_1^I] = \begin{bmatrix} \psi_{I,x} \\ \psi_{I,y} \end{bmatrix},$$

$$[N_2^I] = \begin{bmatrix} \psi_{I,xx} \\ \psi_{I,xy} \\ \psi_{I,yy} \end{bmatrix},$$

$$[N_3^I] = \begin{bmatrix} \psi_I \\ \psi_{I,x} \\ \psi_{I,y} \end{bmatrix}, \quad (56)$$

$$[N_4^I] = \begin{bmatrix} \psi_{I,x} \\ \psi_{I,xx} \\ \psi_{I,xy} \\ \psi_{I,y} \\ \psi_{I,yy} \end{bmatrix}.$$

We rearrange matrix equations (31) and (43) as

$$\begin{bmatrix} \mathbf{M}_{11} & \mathbf{0} \\ \mathbf{0} & \mathbf{M}_{22} \end{bmatrix} \begin{bmatrix} \tilde{\mathbf{w}}_1 \\ \tilde{\mathbf{w}}_2 \end{bmatrix} + \begin{bmatrix} \mathbf{k}_{11} + \mathbf{k}_T & \mathbf{k}_{12} \\ \mathbf{k}_{21} & \mathbf{k}_{22} + \mathbf{k}_T \end{bmatrix} = \mathbf{0}. \quad (57)$$

TABLE 1: Mechanical properties.

E	h	ρ	ν
1.06 TPa	0.34 nm	2250 Kg/m ³	0.25

We assume that

$$\begin{bmatrix} \mathbf{w}_1 \\ \mathbf{w}_2 \end{bmatrix} = \begin{bmatrix} \bar{\mathbf{w}}_1 \\ \bar{\mathbf{w}}_2 \end{bmatrix} e^{i\omega t}. \quad (58)$$

We rewrite (55) as

$$\left(-\omega^2 \begin{bmatrix} \mathbf{M}_{11} & \mathbf{0} \\ \mathbf{0} & \mathbf{M}_{22} \end{bmatrix} + \begin{bmatrix} \mathbf{k}_{11} + \mathbf{k}_T & \mathbf{k}_{12} \\ \mathbf{k}_{21} & \mathbf{k}_{22} + \mathbf{k}_T \end{bmatrix} \right) \begin{bmatrix} \bar{\mathbf{w}}_1 \\ \bar{\mathbf{w}}_2 \end{bmatrix} = \mathbf{0}. \quad (59)$$

By solving eigenvalue problem of (57), the buckling properties of DLGSSs can be presented.

5. Numerical Simulations, Results, and Discussion

In this paper, the nonlocal elastic theory and element-free method are developed for the thermal vibration behavior of DLGSSs. The mechanical properties of GSs are shown in Table 1. To verify the effectiveness of the present study, the comparison of the results is given for circular nature frequency for DLGs with the side length of 10 nm for all edges simply supported by the result obtained by [43]. $\omega_{(m,n)}^i$ in this paper represents the i th interlayer vibration mode frequency. From Table 2, the results of the present study agree well with those of He et al. [43].

Firstly, the influence of the side length and the mode (n, m) on the circular natural frequency of the square DLGSSs under SSSS boundary condition is plotted in Figure 3. It can be studied that, for all of the first vibration mode, the circular frequencies decrease with the increasing side length whereas, for the second vibration mode, the circular frequencies are not affected by the side length.

Secondly, we conduct a case study on the square DLGSSs with 10 nm width to demonstrate the influence of nonlocal parameter on the circular natural frequency. From Figure 4, we also can observe that, for all of the first vibration mode, the circular frequencies decrease with the increasing nonlocal parameter. However, for the second vibration mode, the circular natural frequencies are not influenced by the nonlocal parameters.

Then, in Figure 5, the influence of the aspect ratio on the frequency of DLGSSs with the length of 10 nm under various boundary conditions is considered. It can be seen in Figure 5 that, under various boundary conditions, all the first vibration mode circular natural frequencies decrease as the aspect ratio increases. We also can study that, under the same condition, the first interlayer circular natural frequency under CCCC boundary condition is higher than the other boundary condition. However, the second interlayer circular

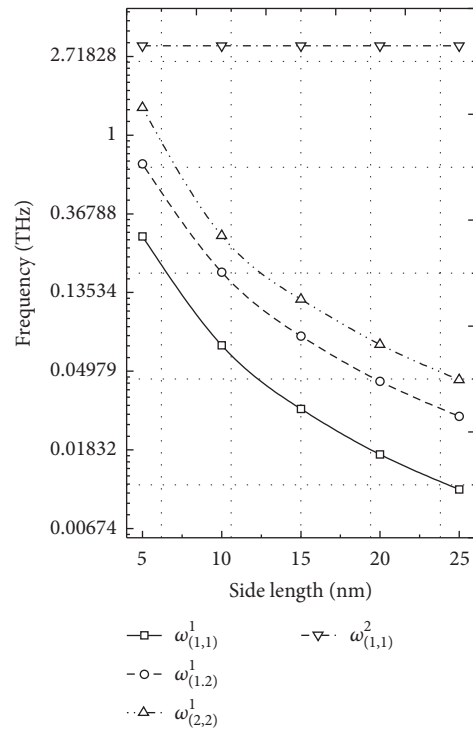


FIGURE 3: Frequency response with the side length for square DLGSs ($T = 0$, $k_g = k_w = 0$, SSSS, $e_0 a = 0$).

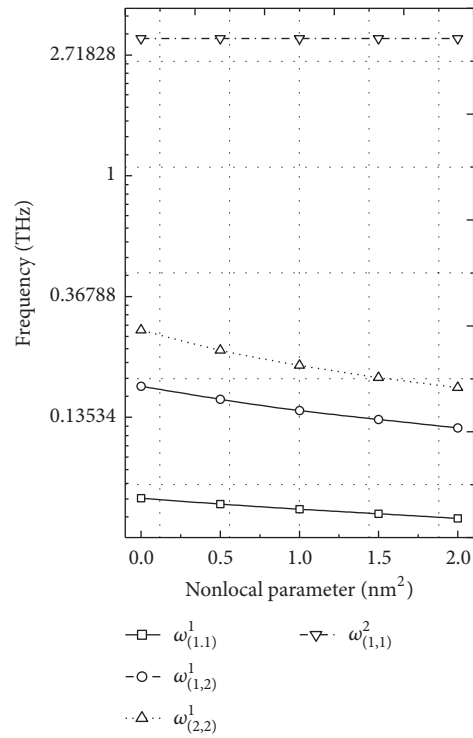


FIGURE 4: Variation of frequency with the nonlocal parameter for square DLGSs ($T = 0$, $k_g = k_w = 0$, SSSS, $L_b = 10$ nm).

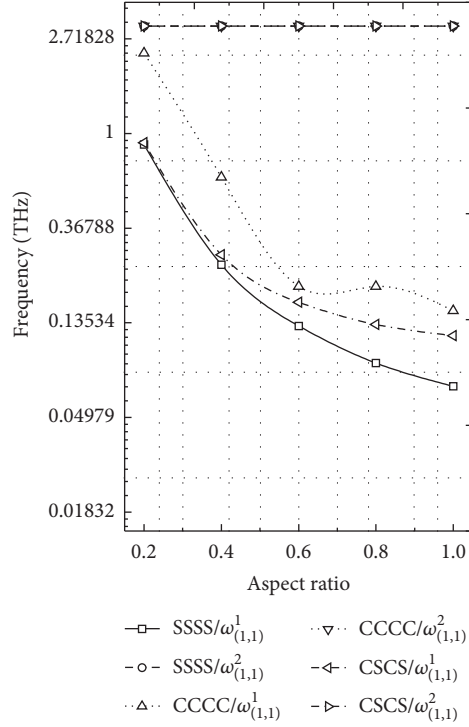


FIGURE 5: Frequency response with the aspect ratio for DLGSs ($T = 0$, $k_g = k_w = 0$, $L_b = 10$ nm, $e_0 a = 0$).

TABLE 2: Comparison of the present study with the published ones for square DLGSs with width $b = 10$ nm.

ω (THz)	$\omega^1_{(1,1)}$	$\omega^1_{(1,2)}$	$\omega^1_{(2,1)}$	$\omega^1_{(2,2)}$	$\omega^2_{(1,1)}$	$\omega^2_{(1,2)}$	$\omega^2_{(2,2)}$
He et al.	0.069	0.173	0.173	0.276	2.683	2.688	2.697
Present	0.0692	0.175	0.175	0.2787	2.680	2.684	2.693

natural frequencies under various boundary conditions are not affected by the aspect ratio and the frequencies are the same.

The influence of stacking types of DLGSs on the vibration is also studied. Figure 6 shows the frequency change with the side length under various boundary conditions and two stacking types of DLGSs. Figure 6 indicates that the first interlayer mode circular natural frequency is not affected by the stacking types of DLGSs. However, for second interlayer mode, the circular natural frequency for the AA stacking types is smaller than the AB stacking types.

To study the effects of Pasternak elastic foundation on the interlayer mode circular natural frequency of DLGSs, a case is simulated on square DLGSs with side length of 10 nm under various boundary conditions. The nondimensional Winker modulus parameter \bar{k}_W and shear modulus parameter \bar{k}_G are adopted. The nondimensional parameters are defined as

$$\begin{aligned} \bar{k}_W &= \frac{k_w L_x^4}{D}, \\ \bar{k}_G &= \frac{k_g L_x^2}{D}. \end{aligned} \quad (60)$$

As shown in Figure 7, the Winker modulus parameter $\bar{k}_W = 0$. Figure 7 indicates that, for the first vibration mode, the circular frequencies increase with the increasing of \bar{k}_G . The first natural frequency under CCCC boundary condition is larger than that under other boundary conditions. In contrast, the second natural frequency is not affected by the shear modulus parameter. Figure 8 shows the relationship between the interlayer circular natural frequency and Winker modulus parameter. It is evident that, for the first mode, the natural frequencies increase with the increasing of Winker modulus parameter. However, for the second mode, the circular natural frequency is not influenced by the Winker modulus parameter.

Finally, to comprehensively understand the effect of the temperature and temperature distribution coefficient on the interlayer mode circular natural frequency, we simulate the vibration behavior of square DLGSs with 10 nm width under SSSS boundary condition. Figure 9 presents the frequency responses under low temperature environment; as shown in Figure 9, under low temperature environment, the interlayer mode circular natural frequency is not affected by the temperature and temperature distribution types. However, as is evident from Figure 10, under high temperature environment, the first interlayer mode circular natural frequency

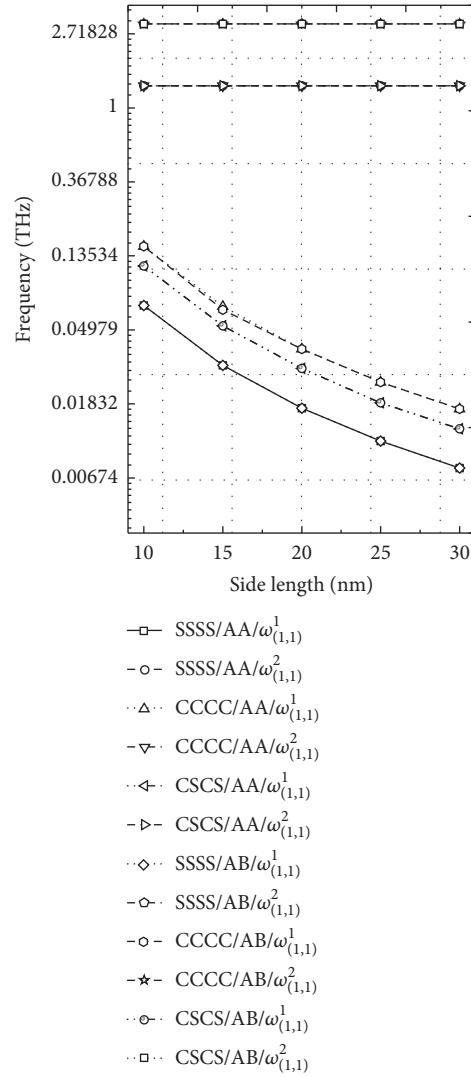


FIGURE 6: Frequency response with the stacking types for square DLGSs ($T = 0$, $k_g = k_w = 0$, $e_0 a = 0$).

decreases with increasing of the temperature under various temperature distribution types. However, for the second mode, the natural frequency is not affected by either the temperature or the temperature distribution types.

6. Conclusion

In this paper, the nonlocal elasticity theory and element-free method are utilized to reveal the vibration properties of DLGDs resting on a Winker's elastic medium in thermal environment. Influence of side length, nonlocal parameters, boundary conditions, elastic medium parameter, stacking types of graphene, aspect ratio, and temperature distribution types on the interlayer mode circular natural frequency is examined. The results reveal that, for the first mode, the natural frequency is related to the nonlocal parameter, side length, boundary condition, elastic medium parameter, and aspect ratio, but is unrelated to the vdW force. On the contrary, for the second mode, the natural frequency is

related to the vdW force, but is not affected by the side length, boundary condition, nonlocal parameter, aspect ratio, elastic medium parameter, and temperature distribution types.

Conflicts of Interest

The authors declare that they have no conflicts of interest.

Acknowledgments

This work is supported by National Natural Science Foundation of China under Grants nos. 71771161, 61472267, 51375323, 61503335, and 71271119, Fundamental Research Funds for the Central Universities under Grant no. 30917011339, Natural Science Foundation of Jiangsu Province under Grant no. BK20170820, Jiangsu Provincial Department of Housing and Urban-Rural Development under Grant no. 2017ZD253,

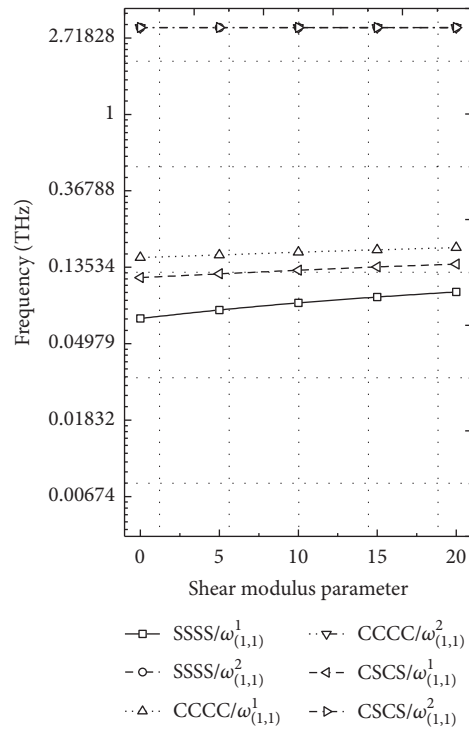


FIGURE 7: Variation of frequency with the shear modulus parameter for square DLGSs ($T = 0$, $k_w = 0$, $L_b = 10$ nm, $e_0 a = 0$).

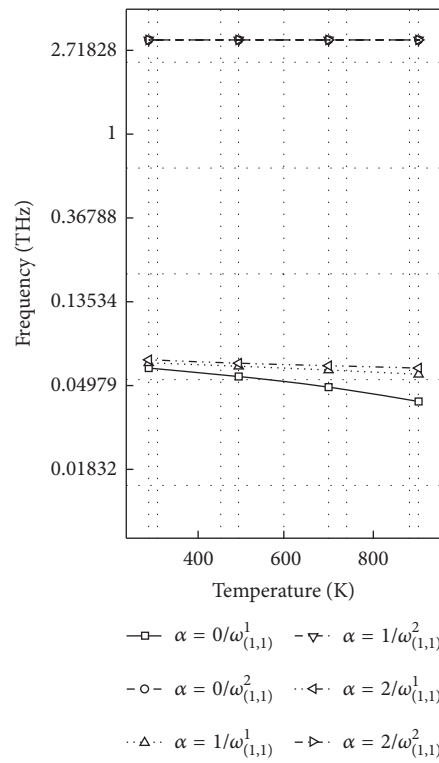


FIGURE 8: Variation of frequency with the Winker modulus parameter for square DLGSs ($T = 0$, $k_g = 0$, $L_b = 10$ nm, $e_0 a = 0$).

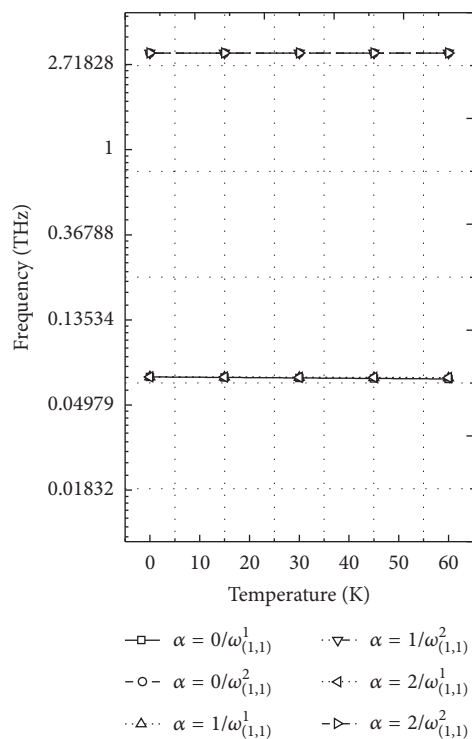


FIGURE 9: Variation of frequencies with the low temperature for square DLGSs ($k_w = k_g = 0$, $L_b = 10$ nm, $e_0 a = 0$, SSSS).

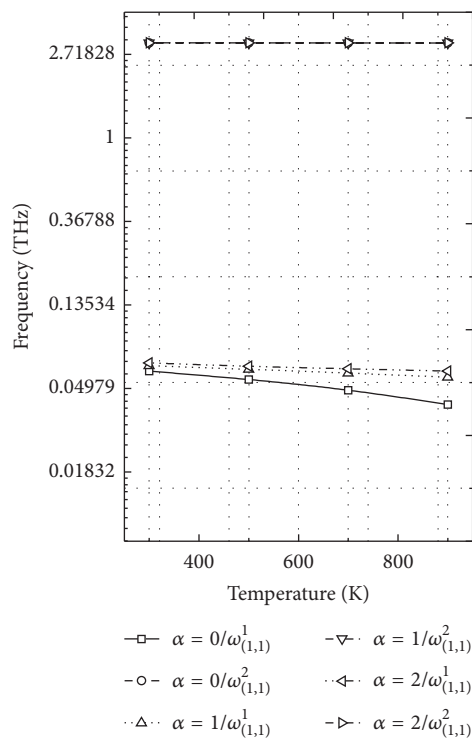


FIGURE 10: Frequency change with the high temperature for square DLGSs ($k_w = k_g = 0$, $L_b = 10$ nm, $e_0 a = 0$, SSSS).

Alexander von Humboldt Foundation of Germany, and Social Development Project of Jiangsu Provincial under Grant no. BE2017663.

References

- [1] K. S. Novoselov, A. K. Geim, S. V. Morozov et al., “Electric field in atomically thin carbon films,” *Science*, vol. 306, no. 5696, pp. 666–669, 2004.
- [2] A. Sakhaee-Pour, M. T. Ahmadian, and A. Vafai, “Potential application of single-layered graphene sheet as strain sensor,” *Solid State Communications*, vol. 147, no. 7-8, pp. 336–340, 2008.
- [3] B. G. Demczyk, Y. M. Wang, J. Cumings et al., “Direct mechanical measurement of the tensile strength and elastic modulus of multiwalled carbon nanotubes,” *Materials Science and Engineering: A Structural Materials: Properties, Microstructure and Processing*, vol. 334, no. 1-2, pp. 173–178, 2002.
- [4] C. Lee, X. Wei, J. W. Kysar, and J. Hone, “Measurement of the elastic properties and intrinsic strength of monolayer graphene,” *Science*, vol. 321, no. 5887, pp. 385–388, 2008.
- [5] A. A. Balandin, “Thermal properties of graphene and nanostructured carbon materials,” *Nature Materials*, vol. 10, no. 8, pp. 569–581, 2011.
- [6] J. S. Bunch, A. M. Van Der Zande, S. S. Verbridge et al., “Electromechanical resonators from graphene sheets,” *Science*, vol. 315, no. 5811, pp. 490–493, 2007.
- [7] F. Scarpa, S. Adhikari, and A. S. Phani, “Effective elastic mechanical properties of single layer graphene sheets,” *Nanotechnology*, vol. 20, no. 6, Article ID 065709, 2009.
- [8] Y. Shao, J. Wang, H. Wu, J. Liu, I. A. Aksay, and Y. Lin, “Graphene based electrochemical sensors and biosensors: a review,” *Electroanalysis*, vol. 22, no. 10, pp. 1027–1036, 2010.
- [9] N. A. H. Castro, “The electronic properties of graphene,” *Vacuum*, vol. 83, no. 10, pp. 1248–1252, 2007.
- [10] J. W. Yan, K. M. Liew, and L. H. He, “Free vibration analysis of single-walled carbon nanotubes using a higher-order gradient theory,” *Journal of Sound and Vibration*, vol. 332, no. 15, pp. 3740–3755, 2013.
- [11] N. Yao and V. Lordi, “Young’s modulus of single-walled carbon nanotubes,” *Journal of Applied Physics*, vol. 84, no. 4, pp. 1939–1943, 1998.
- [12] Y. Zhang, L. W. Zhang, K. M. Liew, and J. L. Yu, “Free vibration analysis of bilayer graphene sheets subjected to in-plane magnetic fields,” *Composites Part B: Engineering*, vol. 144, pp. 86–95, 2016.
- [13] M. Mirparizi and F. Aski, “Interlayer shear effect on vibrational behavior of bilayer graphene using the molecular mechanics simulation,” *Propulsion and Power Research*, vol. 5, no. 3, pp. 250–260, 2016.
- [14] S. O. Gajbhiye and S. P. Singh, “Multiscale nonlinear frequency response analysis of single-layered graphene sheet under impulse and harmonic excitation using the atomistic finite element method,” *Journal of Physics D: Applied Physics*, vol. 48, no. 14, Article ID 145305, 2015.
- [15] B. Arash and Q. Wang, “A review on the application of nonlocal elastic models in modeling of carbon nanotubes and graphenes,” *Computational Materials Science*, vol. 51, no. 1, pp. 303–313, 2012.
- [16] K. Behfar and R. Naghdabadi, “Nanoscale vibrational analysis of a multi-layered graphene sheet embedded in an elastic medium,” *Composites Science and Technology*, vol. 65, no. 7-8, pp. 1159–1164, 2005.
- [17] K. Behfar, P. Seifi, R. Naghdabadi, and J. Ghanbari, “An analytical approach to determination of bending modulus of a multi-layered graphene sheet,” *Thin Solid Films*, vol. 496, no. 2, pp. 475–480, 2006.
- [18] F. Yang, A. C. M. Chong, D. C. C. Lam, and P. Tong, “Couple stress based strain gradient theory for elasticity,” *International Journal of Solids and Structures*, vol. 39, no. 10, pp. 2731–2743, 2002.
- [19] P. Lu, L. H. He, H. P. Lee, and C. Lu, “Thin plate theory including surface effects,” *International Journal of Solids and Structures*, vol. 43, no. 16, pp. 4631–4647, 2006.
- [20] N. A. Fleck and J. W. Hutchinson, “Strain gradient plasticity,” *Advances in Applied Mechanics*, vol. 33, pp. 295–361, 1997.
- [21] P. Malekzadeh, A. R. Setoodeh, and A. A. Beni, “Small scale effect on the thermal buckling of orthotropic arbitrary straight-sided quadrilateral nanoplates embedded in an elastic medium,” *Composite Structures*, vol. 93, no. 8, pp. 2083–2089, 2011.
- [22] A. M. Zenkour and M. Sobhy, “Nonlocal elasticity theory for thermal buckling of nanoplates lying on Winkler-Pasternak elastic substrate medium,” *Physica E: Low-dimensional Systems and Nanostructures*, vol. 53, pp. 251–259, 2013.
- [23] M. Mohammadi, A. Farajpour, A. Moradi, and M. Ghayour, “Shear buckling of orthotropic rectangular graphene sheet embedded in an elastic medium in thermal environment This article is dedicated to Professor Hossien Mohammadi (Amir Hossien Mohammadi) on the occasion of his 60th birthday,” *Composites Part B: Engineering*, vol. 56, pp. 629–637, 2014.
- [24] J. Peddieson, G. R. Buchanan, and R. P. McNitt, “Application of nonlocal continuum models to nanotechnology,” *International Journal of Engineering Science*, vol. 41, no. 3-5, pp. 305–312, 2003.
- [25] W. H. Duan and C. M. Wang, “Exact solutions for axisymmetric bending of micro/nanoscale circular plates based on nonlocal plate theory,” *Nanotechnology*, vol. 18, no. 38, Article ID 385704, 2007.
- [26] S. Dastjerdi and M. Jabbarzadeh, “Non-linear bending analysis of multi-layer orthotropic annular/circular graphene sheets embedded in elastic matrix in thermal environment based on non-local elasticity theory,” *Applied Mathematical Modelling*, vol. 41, pp. 83–101, 2017.
- [27] K. M. Liew, X. Q. He, and S. Kitipornchai, “Predicting nanovibration of multi-layered graphene sheets embedded in an elastic matrix,” *Acta Materialia*, vol. 54, no. 16, pp. 4229–4236, 2006.
- [28] L. W. Zhang, Y. Zhang, and K. M. Liew, “Vibration analysis of quadrilateral graphene sheets subjected to an in-plane magnetic field based on nonlocal elasticity theory,” *Composites Part B: Engineering*, vol. 118, pp. 96–103, 2017.
- [29] S. C. Pradhan and J. K. Phadikar, “Small scale effect on vibration of embedded multilayered graphene sheets based on nonlocal continuum models,” *Physics Letters A*, vol. 373, no. 11, pp. 1062–1069, 2009.
- [30] S. R. Asemi, A. Farajpour, M. Borghei, and A. H. Hassani, “Thermal effects on the stability of circular graphene sheets via nonlocal continuum mechanics,” *Latin American Journal of Solids and Structures*, vol. 11, no. 4, pp. 704–724, 2013.
- [31] S. R. Asemi, M. Mohammadi, and A. Farajpour, “A study on the nonlinear stability of orthotropic singlelayered graphene sheet based on nonlocal elasticity theory,” *Latin American Journal of Solids and Structures*, vol. 11, no. 9, pp. 1541–1564, 2014.
- [32] W. Zhang and X. Wang, “Elastoplastic buckling analysis of thick rectangular plates by using the differential quadrature method,”

- Computers & Mathematics with Applications*, vol. 61, no. 1, pp. 44–51, 2011.
- [33] Y. Huang and Q.-Z. Luo, “A simple method to determine the critical buckling loads for axially inhomogeneous beams with elastic restraint,” *Computers & Mathematics with Applications*, vol. 61, no. 9, pp. 2510–2517, 2011.
- [34] R. Ansari, R. Rajabiehfard, and B. Arash, “Nonlocal finite element model for vibrations of embedded multi-layered graphene sheets,” *Computational Materials Science*, vol. 49, no. 4, pp. 831–838, 2010.
- [35] L. W. Zhang, Y. J. Deng, and K. M. Liew, “An improved element-free Galerkin method for numerical modeling of the biological population problems,” *Engineering Analysis with Boundary Elements*, vol. 40, pp. 181–188, 2014.
- [36] K. M. Liew, Z. X. Lei, J. L. Yu, and L. W. Zhang, “Postbuckling of carbon nanotube-reinforced functionally graded cylindrical panels under axial compression using a meshless approach,” *Computer Methods Applied Mechanics and Engineering*, vol. 268, pp. 1–17, 2014.
- [37] Z. X. Lei, K. M. Liew, and J. L. Yu, “Free vibration analysis of functionally graded carbon nanotube-reinforced composite plates using the element-free kp-Ritz method in thermal environment,” *Composite Structures*, vol. 106, pp. 128–138, 2013.
- [38] Y. Zhang, Z. X. Lei, L. W. Zhang, K. M. Liew, and J. L. Yu, “Non-local continuum model for vibration of single-layered graphene sheets based on the element-free kp-Ritz method,” *Engineering Analysis with Boundary Elements*, vol. 56, pp. 90–97, 2015.
- [39] Z. Wu, F. Hu, Y. Zhang, Q. Gao, and Z. Chen, “Mechanical analysis of double-layered circular graphene sheets as building material embedded in an elastic medium,” *Journal of Central South University*, vol. 24, no. 11, pp. 2717–2724, 2017.
- [40] P. L. Pasternak, *On a New Method of Analysis of an Elastic Foundation by Means of Two Foundation Constants*, Gosudarstvennoe Izdatelstvo Literaturi Po Stroitelstvu I Arkhitekture, Moscow, 1954.
- [41] E. Jomehzadeh, A. R. Saidi, and N. M. Pugno, “Large amplitude vibration of a bilayer graphene embedded in a nonlinear polymer matrix,” *Physica E: Low-dimensional Systems and Nanostructures*, vol. 44, no. 10, pp. 1973–1982, 2012.
- [42] J.-S. Chen, C. Pan, C.-T. Wu, and W. K. Liu, “Reproducing kernel particle methods for large deformation analysis of nonlinear structures,” *Computer Methods Applied Mechanics and Engineering*, vol. 139, no. 1-4, pp. 195–227, 1996.
- [43] X. Q. He, S. Kitipornchai, and K. M. Liew, “Resonance analysis of multi-layered graphene sheets used as nanoscale resonators,” *Nanotechnology*, vol. 16, no. 10, pp. 2086–2091, 2005.

Research Article

Tunable Multilayers of Self-Organized Silica Nanospheres by Spin Coating

Sofiane Kasmi,¹ Jeanne Solard,^{2,3} Inga Tijunelyte,¹ Alexis P. A. Fischer,^{2,3}
Marc Lamy de la Chapelle,¹ and Nathalie Lidgi-Guigui ¹

¹Laboratoire CSPBAT UMR CNRS 7244, UFR SMBH, Université Paris 13, Sorbonne Paris Cité, 74 rue Marcel Cachin, 93017 Bobigny, France

²Laboratoire de Physique de Lasers CNRS UMR 7538, Université Paris 13, Sorbonne Paris Cité, 99 avenue Jean-Baptiste Clément, 93430 Villetaneuse, France

³Centrale de Proximité en Nanotechnologies de Paris Nord, Université Paris 13, Sorbonne Paris Cité, 99 avenue Jean-Baptiste Clément, 93430 Villetaneuse, France

Correspondence should be addressed to Nathalie Lidgi-Guigui; nathalie.lidgi-guigui@univ-paris13.fr

Received 24 November 2017; Revised 1 February 2018; Accepted 12 February 2018; Published 14 March 2018

Academic Editor: Weidong Liu

Copyright © 2018 Sofiane Kasmi et al. This is an open access article distributed under the Creative Commons Attribution License, which permits unrestricted use, distribution, and reproduction in any medium, provided the original work is properly cited.

The coating of fused silica by an organized layer of silica nanospheres (NS) is an important issue for the design of optical and topographic properties especially for lithography techniques such as nanosphere lithography (NSL) or nanosphere photolithography (NSPL). Here, the spin coating of NS dispersed in N,N-dimethylformamide (DMF) is studied. The role of the NS diameter, the spin-coating acceleration, and the volume fraction are the parameters to take into account for the formation and organization of NS in single or double closely packed layers. We propose an explanation for this behavior based on the transition between sedimentation and a viscous regime on the basis of the silica NS organization.

1. Introduction

The organization of nanostructures on a surface is an important issue that many fields are confronted with. The application field of such materials depends on the dimension range of the nanostructures. For this purpose, a large variety of techniques have been developed to nicely localize the structure at a desired position. Top-down techniques, such as lithography, are preferred when it comes to placing a single structure at a specific position. For instance, e-beam lithography (EBL) uses the electron beam of a scanning electron microscope (SEM) to draw a pattern on an electroresistive resist. If EBL can indeed be used to design assemblies of nanostructures, it will be highly time-consuming and will become quite challenging when more than 1mm^2 has to be covered. For large assemblies of nanostructures, soft lithography techniques can be exploited such as nanoimprint lithography [1, 2]. Yet, bottom-up techniques are often more suitable for surface functionalization [3, 4], which make nanostructures become trapped on the surface by reactive

termination. Another strategy more suitable for larger nanostructures (a few hundreds of nanometers) is to deposit a drop of the solution in which nanospheres (NS) are dispersed; it has been shown that the evaporation of the solvent allows the formation of a nicely organized film [5]. However, this technique is difficult to control especially for samples with an area typically greater than 1mm^2 . This is why other techniques have been developed with success to reach the objective of the elaboration of a single layer of NS on a large area: Langmuir-Blodgett [6, 7], surface chemistry [8], and dip coating [9, 10]. Spin coating is probably the easiest and fastest way to get to this result [11–14]. It consists in placing a droplet of an NS solution on a substrate and taking advantage of its fast rotation to spread the liquid. In order to form a layer of organized NS, they have to be dispersed in a solution with high wettability (so that they can easily spread on the surface) and high volatility (so that the liquid phase is quickly removed as soon as the NS are spread). The wettability is usually achieved by adding a surfactant such as octoxynol, while the volatility is achieved by choosing

a solvent such as methanol. As the solution result in a mixture of surfactant, solvent, and NS, a fine optimization procedure has to be implemented. Octoxynol in methanol is one of the most frequent combinations reported in the literature; its concentration ratio can vary from a reference to another [15, 16]. This demonstrates that the reproducibility of the results is rarely straightforward. Choi et al. [11] have proposed the use of N,N-dimethylformamide (DMF) as a solvent, as it has all the necessary qualities to easily and efficiently perform deposition of a large area of self-organized NS. Most importantly, as DMF is used in a pure form, no optimization step is required.

The use of single or double layers can have a tremendous advantage in a diversity of topics. For example, soft lithography techniques are currently developed to promote nanostructuration on transparent and flexible substrates. Nanoimprint lithography (NIL) [1, 2], nanosphere lithography (NSL), [14, 16] and its derivative Film Over Nanospheres (FON) [15] or nanosphere photolithography (NSPL) [10] can all take advantage of the ease of controlling the number of silica NS layers. In these techniques, the pattern formed by the organization of the NS is used as a mask or a mold. In NSL, metal is deposited through the spaces in between the NS; it forms triangles for a single layer of NS; more complex patterns can be reached with a two-layer mask. In NSPL, silica NS are used as lenses for UV light illumination of photoreists. This technique can also take advantage of varying the number of NS layers in order to create different patterns of interferences. For these particular applications, the number of layers should not be too high so a nanostructure can still be formed (presence of interstice for NSL and transmission for NSPL).

In this paper, we study the behavior of NS solution in DMF when spread onto silica surfaces. These surfaces are very similar to the oxide layer of silicon that can be found on top of silicon wafers. Furthermore, the silica surfaces that we have used in this work are transparent to UV and visible light. These substrates can thus be used in a wide range of applications such as transparent electronic devices or as photolithographic masks as proposed by Ayenew et al. [10]. The study of the organization of NS on silica surfaces shows that it is possible to control the number of NS organized layers using a spin-coating technique. We have considered the diameter of the NS and their concentration; these intrinsic properties of the solution are decisive to explain how the spreading occurs in a spin-coating experiment. In particular, the acceleration of spinning has an influence on the organization of the NS. By carefully choosing these parameters, one can choose to form either a single or a double layer of closely packed NS.

2. Experimental

DMF was purchased from Carlo Erba. Silica powders of NS with diameters of 310 nm and 540 nm were purchased from Polysciences Europe GmbH. Solutions of both powders were prepared with volume fractions of 4.1%, 6.1%, 7%, and 7.9%. The volume fraction V_f is calculated as follows:

$$V_f = \frac{4}{3}\pi R^3 \frac{N}{V}, \quad (1)$$

where R is the radius of the NS and N is the number of NS in the volume V .

The solutions were then sonicated for 2 hours in order to ensure a good dispersion of the NS.

The solutions were deposited on fused silica surface (15 × 15 mm) purchased from Nayco. These substrates display high OH content and high flatness. Prior to the deposition of the NS, the substrates were cleaned with acetone and ethanol and treated with UV-ozone for 30 minutes in order to form a hydrophilic surface [17].

The solutions were then spin-coated in a two-step process. The first step is the acceleration of the rotation speed from 0 rpm to 2000 rpm. We have investigated the effect of different acceleration durations: 50 s, 100 s, 150 s, and 200 s. These correspond, respectively, to 4.2 rad·s⁻², 2.1 rad·s⁻², 1.4 rad·s⁻², and 1.0 rad·s⁻². During the second step, the sample rotated at a constant speed (2000 rpm) for 150 s.

All the observations were performed on an SEM Raith Pioneer equipped with a field emission gun (FEG) source. The samples were imaged at 3 kV.

3. Results and Discussion

The spreading of silica NS in DMF solutions by spin coating was tested. Single layers of closely packed NS were obtained without any optimization. The experiment was carried out for NS of 310 nm and 540 nm diameter for an acceleration duration of 150 s and a volume fraction of, respectively, 6.1% and 7.0% (Figures 1(a) and 1(b)). The quality of the organization for both diameters can be seen on the micrometer scale thanks to the SEM images. At a larger scale, Bragg reflection can be seen confirming the organization on the whole sample surface.

The experiment was repeated for different volume fractions and acceleration. For low concentration and high acceleration, single layers are observed displaying some vacancies. When the concentration of NS is increased, complete double layers can be observed for both sizes of NS. In Figure 2, the cross sections of two samples are shown. Both samples are made of 540 nm NS solutions with a volume fraction of 7%. In order to obtain a double layer, the acceleration was decreased from 2.1 rad·s⁻² to 1.0 rad·s⁻².

A set of acceleration and concentration has been tested for both diameters in order to identify the optimal parameters allowing the deposition of single or double layers. The surface coverage was measured by analyzing 20 adjacent SEM scans of 75 μm × 50 μm. The number of layers is represented in Figure 3(a) for the 310 nm NS and in Figure 3(b) for the 540 nm NS. "1" indicates a single layer obtained for a given volume fraction and given acceleration, while "2" stands for a double layer. The fractional numbers refer to the proportion of double layers on the surface. For example, 1.7 means that 30% of the surface is covered by a single layer while 70% is covered by a double layer.

The diagrams in Figures 3(a) and 3(b) reflect the ease of getting a single layer of silica NS since, for volume fractions

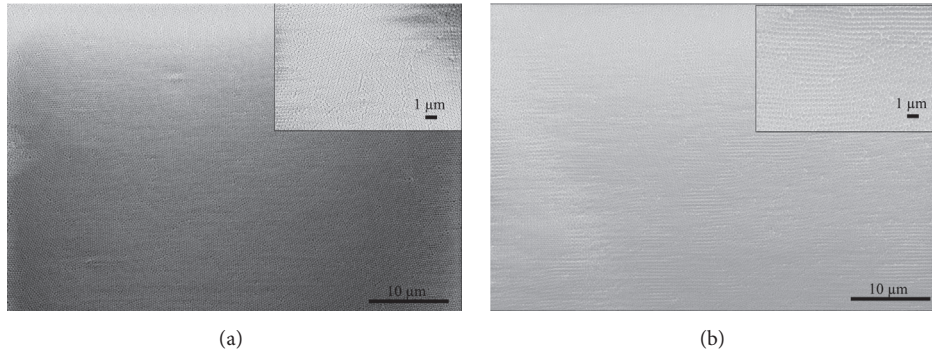


FIGURE 1: Single layers of NS of (a) 310 nm and (b) 540 nm diameter obtained for acceleration of $1.4 \text{ rad}\cdot\text{s}^{-2}$ and volume fractions of (a) 6.1% and (b) 7.0%.

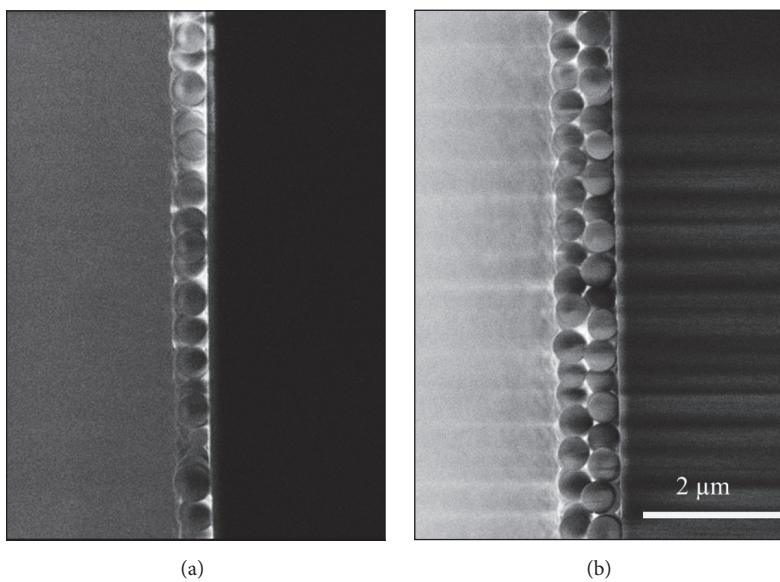


FIGURE 2: Cross section of a sample obtained by the deposition of NS of 540 nm diameter for a volume fraction of 7.0% and acceleration of (a) $2.1 \text{ rad}\cdot\text{s}^{-2}$ and (b) $1.0 \text{ rad}\cdot\text{s}^{-2}$.

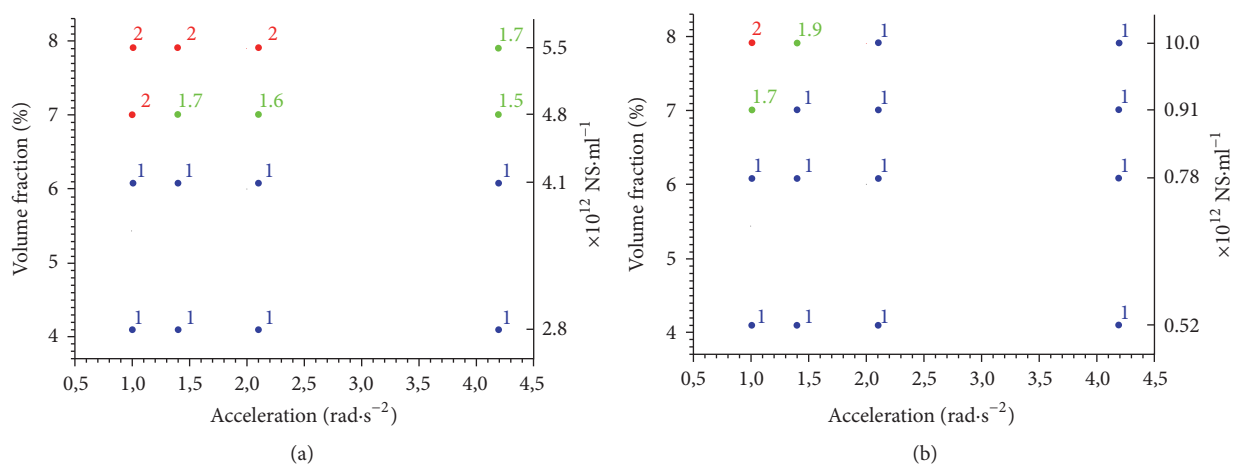


FIGURE 3: Number of layers of self-organized NS as a function of the volume fraction and the acceleration. “1” indicates that a single layer was observed on the entire surface of the sample; “2” indicates that a double layer of organized NS was found on the whole sample surface. Noninteger numbers represent the proportion of double layers on these samples of NS of (a) 310 nm and (b) 540 nm diameter.

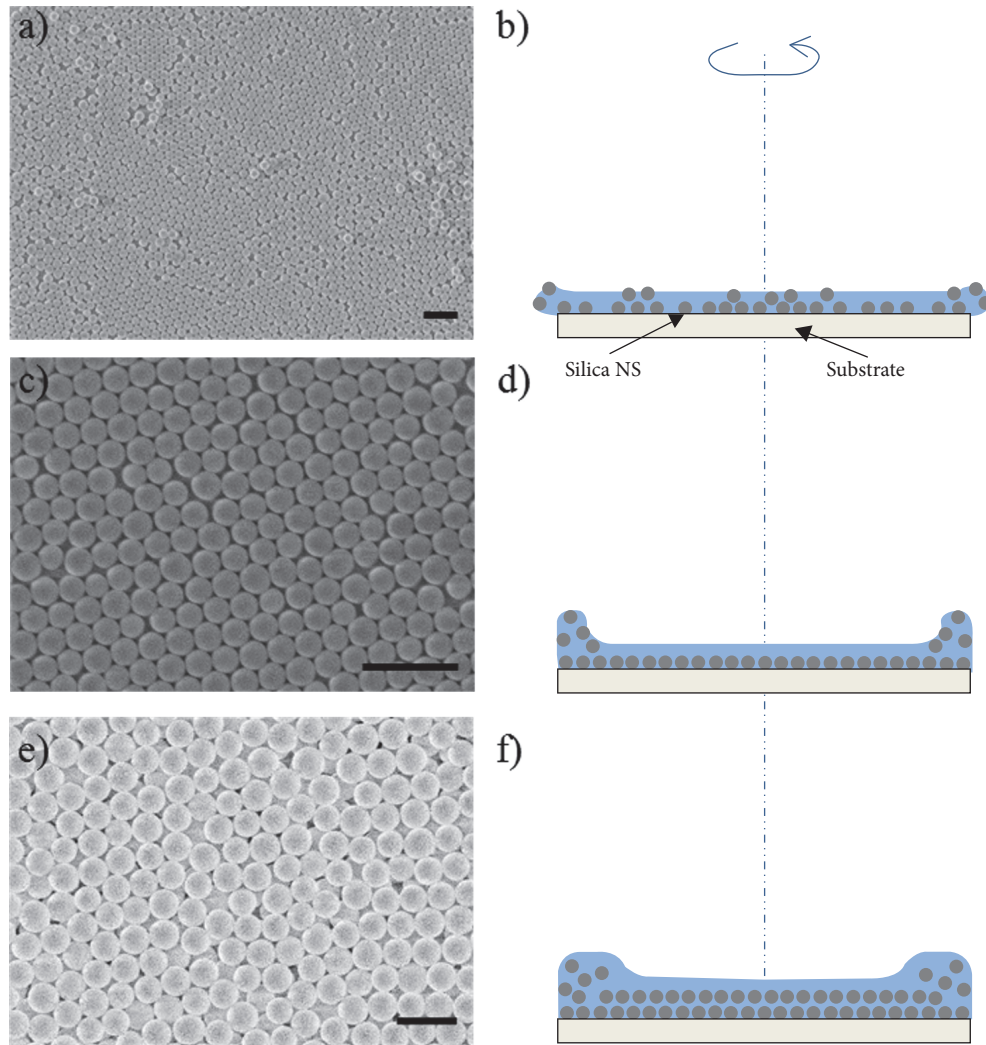


FIGURE 4: Formation of silica NS layers by spin coating. (a, c, e) SEM scan of silica NS spin-coated on fused silica for $4.2 \text{ rad}\cdot\text{s}^{-2}$, $2.1 \text{ rad}\cdot\text{s}^{-2}$, and $1 \text{ rad}\cdot\text{s}^{-2}$ and volume fraction of 4.1%, 6.1%, and 7.9%. The scale bars stand for $1 \mu\text{m}$. (b, d, f) Corresponding schematics of the process of spreading during spinning.

of 4.1% and 6.1%, single layers are obtained for both sizes and for all the acceleration values tested. A more complex behavior is observed for the volume fraction of 7.0% and 7.9%. As the volume fraction increases, multilayers of NS are observed. In the first step, the NS are organized in single layers partly covered by a second one. Then, for other samples, well organized double layers are observed. One can notice that, for a given volume fraction, the proportion of double layers becomes higher when the acceleration is lowered (see, e.g., in Figure 3(b) the volume fraction of 7.9% giving a double layer for $1 \text{ rad}\cdot\text{s}^{-2}$, 1.9 layers for $1.4 \text{ rad}\cdot\text{s}^{-2}$, and only one layer for $2.1 \text{ rad}\cdot\text{s}^{-2}$). Also, samples displaying double layers (partly or entirely) are more often encountered for the 310 nm diameters rather than for the 510 nm. Controlling the number of layers on the surface by adjusting the acceleration, the volume fraction, and the size of the NS appears to be possible.

The acceleration allows the solution to spread on the substrate surface. This is probably during this period of time

when the organization of the NS occurs [12]. As the NS layers are formed, the excess solvent forms bulges on the sample borders. These bulges are expelled when the sample reaches its maximum speed. During this second period, the evaporation of the solvent takes place. If the acceleration is too high, the bulges are immediately expelled and there is no time for the NS to self-organize. This results in a single layer displaying vacancies (Figures 4(a) and 4(b)). Lower acceleration allows the organization of the NS inside the thin layer of the solution between the bulges (Figures 4(c) and 4(d)). The capillary forces play an important role in packing the NS together; if the acceleration is too high, the centrifugal force will exceed the capillary forces and the packing will be poor. If the acceleration is too low, the packing of NS will be better and can even result in a multilayer (Figures 4(e) and 4(f)). Since DMF has a low surface tension coefficient (about $35 \text{ mN}\cdot\text{m}^{-1}$ [18]), it spreads perfectly on hydrophilic surfaces. The bulges are reduced and a uniform concentration of NS is present on the whole sample surface. Yet, these facts fail

to explain the difference of behavior encountered for 310 nm and 540 nm NS.

Regarding the differences in the two diagrams of Figure 3, one needs to take into account two properties of the NS solutions: the NS sedimentation and the viscosity. This latter parameter is linked to the surface tension of the solution that keeps the NS together despite the spinning and the sedimentation. We propose a mechanism for the formation of organized layers by spin coating of silica NS dispersed in DMF based on the competition between sedimentation of the NS and the increasing viscosity of the solution. The sedimentation speed of NS is well described by the following equation:

$$v = \frac{2}{9} \frac{R^2 \Delta \rho g}{\eta}, \quad (2)$$

where R is the sphere radius, $\Delta \rho$ is the density difference between silica and solvent, g is the acceleration of gravity, and η is the viscosity of the solvent.

This gives a sedimentation speed of $97 \text{ nm}\cdot\text{s}^{-1}$ and $290 \text{ nm}\cdot\text{s}^{-1}$, respectively, for the 310 nm and 540 nm NS before spinning starts. As the volume fraction increases, the interaction between the NS becomes more important. This leads to a more viscous behavior when the volume fraction becomes larger [19]. As a consequence, the sedimentation speed of the NS inside the solution is lower. In such solution, the sedimentation is not the main phenomenon anymore. Smaller NS display a greater number in the solution for the same volume fraction (right y -axis in the diagrams in Figure 3). This explains why the viscous regime is reached for a lower volume fraction.

In order to control the number of layers when depositing NS on a surface, a trade-off has to be found between a sedimentation dominated regime and a viscosity dominated regime. Thus, to obtain a multilayer sample, the volume fraction of the 310 nm NS has to be increased. Another possibility would be to reduce the size of NS, but then the sedimentation would be much slower and the good compromise even more difficult to find.

4. Conclusion

In conclusion, we have proposed a protocol to deposit and control the number of layers of self-organized silica NS on surfaces. The surface of silica that we have used is completely covered by these organized layers, and we believe that it could easily be transferred to even larger surfaces. A mechanism for the formation of these structures is also proposed. The benefit of DMF is found in its high wettability which allows the almost perfect coverage of the substrate and its evaporation rate which is low enough to improve the self-organization of the NS. We found that the competition between the sedimentation and the viscosity of the solution is at the root of the formation of single or double layers. Smaller NS will increase the viscosity of the solution more efficiently and thus decrease the sedimentation. Large-scale double layers of silica NS will then be easier to obtain with smaller diameters. However, it would probably be challenging to

make multilayer samples. For NS of 310 nm, the nanopowder of silica NS will reach the limit of dispersion before the appropriate volume fraction could be reached. Jiang and McFarland [13] circumvented this problem by introducing a polymer matrix in the solvent. This increased the viscosity of the solution and formed multilayer samples.

Conflicts of Interest

The authors declare that they have no conflicts of interest.

Acknowledgments

The authors would like to acknowledge the “Institut Interdisciplinaire en Sciences Expérimentales” of Université Paris 13 for the financial support.

References

- [1] S. Y. Chou, P. R. Krauss, and P. J. Renstrom, “Nanoimprint lithography,” *Journal of Vacuum Science & Technology B, Nanotechnology and Microelectronics: Materials, Processing, Measurement, and Phenomena*, vol. 14, no. 6, pp. 4129–4133, 1996.
- [2] M. Cottat, N. Lidgi-Guigui, I. Tijunelyte et al., “Soft UV nanoimprint lithography-designed highly sensitive substrates for SERS detection,” *Nanoscale Research Letters*, vol. 9, no. 1, 2014.
- [3] O. Seitz, M. M. Chehimi, E. Cabet-Deliry et al., “Preparation and characterisation of gold nanoparticle assemblies on silanised glass plates,” *Colloids and Surfaces A: Physicochemical and Engineering Aspects*, vol. 218, no. 1-3, pp. 225–239, 2003.
- [4] O. Péron, E. Rinnert, M. Lehaitre, P. Crassous, and C. Compère, “Detection of polycyclic aromatic hydrocarbon (PAH) compounds in artificial sea-water using surface-enhanced Raman scattering (SERS),” *Talanta*, vol. 79, no. 2, pp. 199–204, 2009.
- [5] F. Járαι-Szabó, S. Aştılean, and Z. Néda, “Understanding self-assembled nanosphere patterns,” *Chemical Physics Letters*, vol. 408, no. 4-6, pp. 241–246, 2005.
- [6] B. Van Duffel, R. H. A. Ras, F. C. De Schryver, and R. A. Schoonheydt, “Langmuir-Blodgett deposition and optical diffraction of two-dimensional opal,” *Journal of Materials Chemistry*, vol. 11, no. 12, pp. 3333–3336, 2001.
- [7] M. Bardosova, P. Hodge, L. Pach et al., “Synthetic opals made by the Langmuir-Blodgett method,” *Thin Solid Films*, vol. 437, no. 1-2, pp. 276–279, 2003.
- [8] N. Lidgi-Guigui, C. Dablemont, D. Veautier et al., “Grafted 2D assembly of colloidal metal nanoparticles for application as a variable capacitor,” *Advanced Materials*, vol. 19, no. 13, pp. 1729–1733, 2007.
- [9] M. Szekeres, O. Kamalin, P. G. Grobet et al., “Two-dimensional ordering of Stöber silica particles at the air/water interface,” *Colloids and Surfaces A: Physicochemical and Engineering Aspects*, vol. 227, no. 1-3, pp. 77–83, 2003.
- [10] G. T. Ayenew, A. P. A. Fischer, C.-H. Chan et al., “Self-organized nanoparticle photolithography for two-dimensional patterning of organic light emitting diodes,” *Optics Express*, vol. 22, no. 21, pp. A1619–A1633, 2014.
- [11] J.-Y. Choi, T. L. Alford, and C. B. Honsberg, “Solvent-controlled spin-coating method for large-scale area deposition of two-dimensional silica nanosphere assembled layers,” *Langmuir*, vol. 30, no. 20, pp. 5732–5738, 2014.

- [12] T. Ogi, L. B. Modesto-Lopez, F. Iskandar, and K. Okuyama, "Fabrication of a large area monolayer of silica particles on a sapphire substrate by a spin coating method," *Colloids and Surfaces A: Physicochemical and Engineering Aspects*, vol. 297, no. 1-3, pp. 71-78, 2007.
- [13] P. Jiang and M. J. McFarland, "Large-scale fabrication of wafer-size colloidal crystals, macroporous polymers and nanocomposites by spin-coating," *Journal of the American Chemical Society*, vol. 126, no. 42, pp. 13778-13786, 2004.
- [14] C. L. Haynes and R. P. Van Duyne, "Nanosphere lithography: a versatile nanofabrication tool for studies of size-dependent nanoparticle optics," *The Journal of Physical Chemistry B*, vol. 105, no. 24, pp. 5599-5611, 2001.
- [15] L. A. Dick, A. D. McFarland, C. L. Haynes, and R. P. Van Duyne, "Metal film over nanosphere (MFON) electrodes for surface-enhanced Raman spectroscopy (SERS): improvements in surface nanostructure stability and suppression of irreversible loss," *The Journal of Physical Chemistry B*, vol. 106, no. 4, pp. 853-860, 2002.
- [16] J. C. Hulteen, D. A. Treichel, M. T. Smith, M. L. Duval, T. R. Jensen, and R. P. Van Duyne, "Nanosphere lithography: size-tunable silver nanoparticle and surface cluster arrays," *The Journal of Physical Chemistry B*, vol. 103, no. 19, pp. 3854-3863, 1999.
- [17] J. R. Vig and J. W. L. Bus, "UV/Ozone Cleaning of Surfaces," *IEEE Transactions on Parts, Hybrids, and Packaging*, vol. 12, no. 4, pp. 365-370, 1976.
- [18] H. Kahl, T. Wadewitz, and J. Winkelmann, "Surface tension of pure liquids and binary liquid mixtures," *Journal of Chemical & Engineering Data*, vol. 48, no. 3, pp. 580-586, 2003.
- [19] J. C. van Der Werff and C. G. De Kruif, "Hard-sphere Colloidal Dispersions: The Scaling of Rheological Properties with Particle Size, Volume Fraction, and Shear Rate," *Journal of Rheology*, vol. 33, no. 3, pp. 421-454, 1989.

Research Article

Defect Analysis in Microgroove Machining of Nickel-Phosphide Plating by Small Cross-Angle Microgrooving

Xiaobin Dong,¹ Tianfeng Zhou ,² Siqin Pang,² Zhiqiang Liang,² Qian Yu,¹ Benshuai Ruan,¹ and Xibin Wang²

¹School of Mechanical Engineering, Beijing Institute of Technology, No. 5 Zhongguancun South Street, Haidian District, Beijing 100081, China

²Key Laboratory of Fundamental Science for Advanced Machining, Beijing Institute of Technology, No. 5 Zhongguancun South Street, Haidian District, Beijing 100081, China

Correspondence should be addressed to Tianfeng Zhou; zhoutf@bit.edu.cn

Received 27 November 2017; Accepted 31 January 2018; Published 27 February 2018

Academic Editor: Haihui Ruan

Copyright © 2018 Xiaobin Dong et al. This is an open access article distributed under the Creative Commons Attribution License, which permits unrestricted use, distribution, and reproduction in any medium, provided the original work is properly cited.

Crystalline nickel-phosphide (c-Ni-P) plating is a newly developed mold material for precision glass molding (PGM) to fabricate microgrooves. In the ultraprecision cutting process of the c-Ni-P plating material, the neighboring microgrooves are required to adjoin with each other to ensure acute microgroove ridges and miniaturize the microgroove size. Generally, defects of burrs and fracture pits can easily occur on the ridges when the plating layer is grooved. Burrs appear when tears dominate in material removal with a large adjacent amount. With the change of the adjacent amount, the removed material is sheared out from the workpiece, and when the cutting depth of the groove ridge is over the brittle-ductile transition thickness, fracture pits arise. To restrict these defects, a small cross-angle microgrooving method is proposed to test the critical adjacent amount range efficiently. It is found that an acute ridge of the microgroove is formed with a small enough adjacent amount; when this amount is in the range of 570 nm~720 nm in the microgroove machining process, fracture pits begin to arise on the gradient edge. High-quality microgrooves can be obtained based on this methodology.

1. Introduction

An optical glass microgroove array is an important component in photoelectric systems due to its function of reducing light reflectivity, improving transmittance/diffraction efficiency, and controlling light spectrum distribution [1–3]. However, it is difficult to fabricate optical glass microgrooves directly because of the brittleness of the glass materials at room temperature [4–6]. Precision glass molding (PGM) is a promising method to fabricate glass microgroove arrays with high efficiency, high accuracy, and low cost [7–9]. The shape of the molded glass is decided by the patterns on the mold surface, and the quality of the mold is of great significance for the PGM process. The mold material should have sufficiently high hardness at molding temperature and favourable micromachinability at room temperature. Silicon carbide (SiC) and tungsten carbide (WC) are too hard to be

machined, while the copper and aluminium are too soft to maintain the microshape under high pressure [10, 11].

Electroless nickel-phosphide (Ni-P) plating is an important mold surface preparation technology, which provides hard, wear-resistant, and corrosion-resistant surfaces with excellent micromachinability for single-point diamond cutting [12, 13]. A two-step cutting process that eliminates burr formation along the microgroove side and improves the quality of the microgroove on Ni-P plating was proposed by Yan et al. [14]. The forming mechanism of the burr was studied based on the pile-up model in a scratch test. The cutting depth and the edge radius of the diamond tool are considered to be the two main factors of burr formation due to the plastic flow material [15]. An energy method was used to predict the chip flow directions, and the calculated results agreed with the experimental results, which proved that the energy method is valid for designing

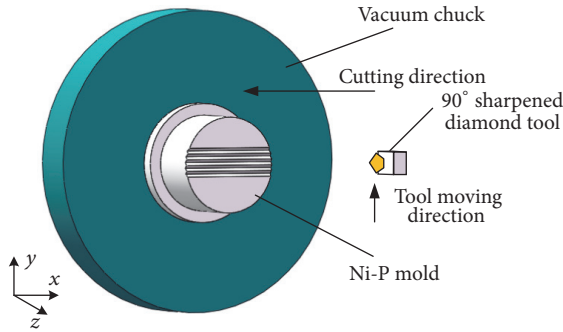


FIGURE 1: Ni-P microgroove mold single-point diamond cutting.

appropriate undeformed chip geometry to reduce burrs in ultraprecision microgrooving on Ni-P plating [16]. The wear and tear of the mold was the bottleneck of restriction of the PGM. To improve the hardness of the mold and prolong the service life, crystalline nickel-phosphide was developed by heat treatment [17, 18]. The material characteristics and removal mechanism of crystalline Ni-P plating are quite different than those of amorphous plating in terms of both brittleness and ductility for crystalline Ni-P. Few studies have been performed on the defect reduction and high-precision microgroove machining on the crystalline Ni-P material.

The goal of this paper is to restrict the defects that emerge on the ridge of the microgroove machined on crystalline Ni-P plating. In the microgrooving process, we denoted the overlap gap between the neighboring microgrooves “adjacent amount,” which determines the size and the interval of the microgrooves. Burrs and fracture pits are easily formed on the microgroove ridge during the microgroove forming with different adjacent amounts. First, the forming mechanisms are discussed theoretically. To identify the forming mechanism of the defect and reduce the appropriate adjacent amount, a method of small cross-angle microgrooving is proposed. Next, the defects of microgroove machining are identified on the gradient edge formed by the method. Finally, through the gradual change of the material removal condition, the microgroove machining mechanism for different adjacent amounts is analysed.

2. Difficulties of Ni-P Mold Microgrooving

2.1. Mold Microgrooving Process. The experiment of microgroove machining is carried out on an ultraprecision machine centre Nanoform X (produced by Precitech Corporation, USA), which achieves a positioning resolution of 0.016 nm and a moving straightness of 0.1 $\mu\text{m}/50\text{ mm}$. As shown in Figure 1, the workpiece of the Ni-P mold that is fixed by a vacuum chuck is machined by a V-shaped diamond tool with an included angle of 90°.

A precision vertical positioning stage fixed under the tool holder is developed to achieve height adjustment. The diamond tool should find the surface of the mold before the machining, and a tool setting error is inevitable in this step, regardless of the precision of the machine tool. For this problem, the neighboring grooves must be adjoining

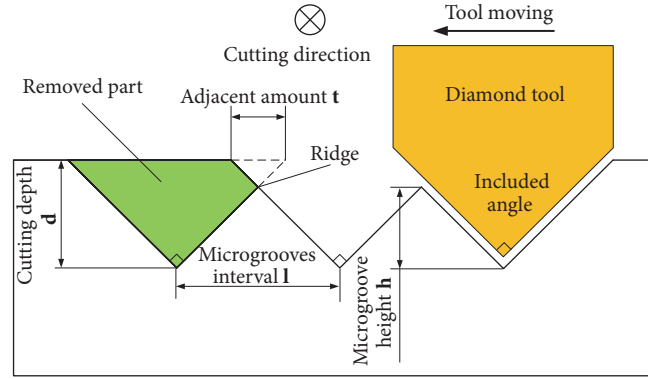


FIGURE 2: Diagram of adjacent amount control for microgrooves.

with each other to a certain extent to ensure high-precision machining and an acute microgroove ridge. In this way, the size of the microgroove is determined by the interval of neighboring grooves l instead of cutting depth d (Figure 2). Thus, the tool setting error is totally eliminated. The height of the microgroove is half of the interval of neighboring grooves for the cutting tool of the 90° included angle. The adjacent amount t is obtained:

$$t = 2d \tan 45^\circ - l. \quad (1)$$

2.2. Machining Defects in Mold Microgrooving. Figure 3 shows scanning electron microscope (SEM) images of defects, including burrs and fracture pits. During cutting, the tool moved from right to left, and the feed of each single microgroove cutting is 3.0 μm . The intervals of the microgrooves are 1.0 μm and 4.8 μm . It can be deduced from (1) that the adjacent amounts are 5.0 μm and 1.2 μm , respectively. In Figure 3(a), burrs are formed on the side of an earlier machined microgroove. The morphology of the burrs shows that the cutting direction is from the bottom up. In Figure 3(b), discontinuous fracture pits are located mainly on the ridges of the later machined surface of each single microgroove.

3. Mechanism of Defect Formation in Microgrooving

3.1. Modelling of Defect Formation in Microgrooving. Burr restricting is important in microgroove machining. Gillespie was among the first to describe different types of burrs. Four types of machining burrs were defined (Figure 4): Poisson burr, rollover burr, tear burr, and cut-off burr. The Poisson burr results from the material's tendency to bulge to the sides when it is compressed until permanent plastic deformation occurs. The forming mechanism of a rollover burr is essentially the material being bent in a cutting process such as end milling. The tear burr is the result of material tearing loose from the workpiece rather than shearing clearly. The cut-off burr is the result of workpiece separation from the raw material before the separation cut is finished [19, 20]. The size of the burrs in the SEM photo is similar to the height of the microgroove, which is too large to form by extrusion or

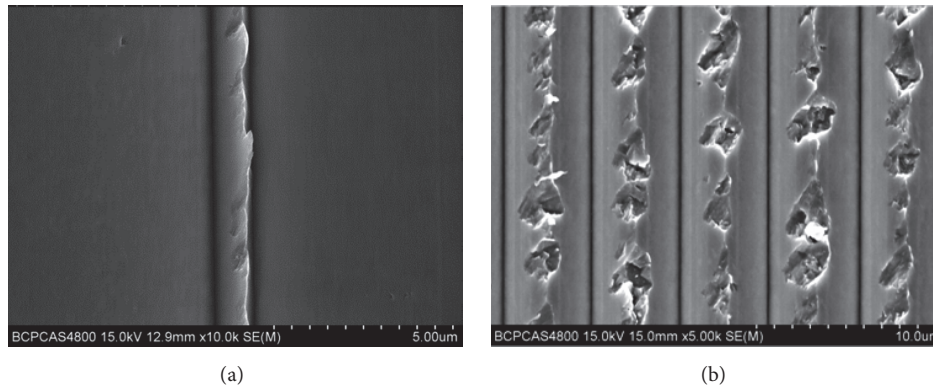


FIGURE 3: Machining defects of adjacent microgrooves: (a) burrs and (b) fracture pits.

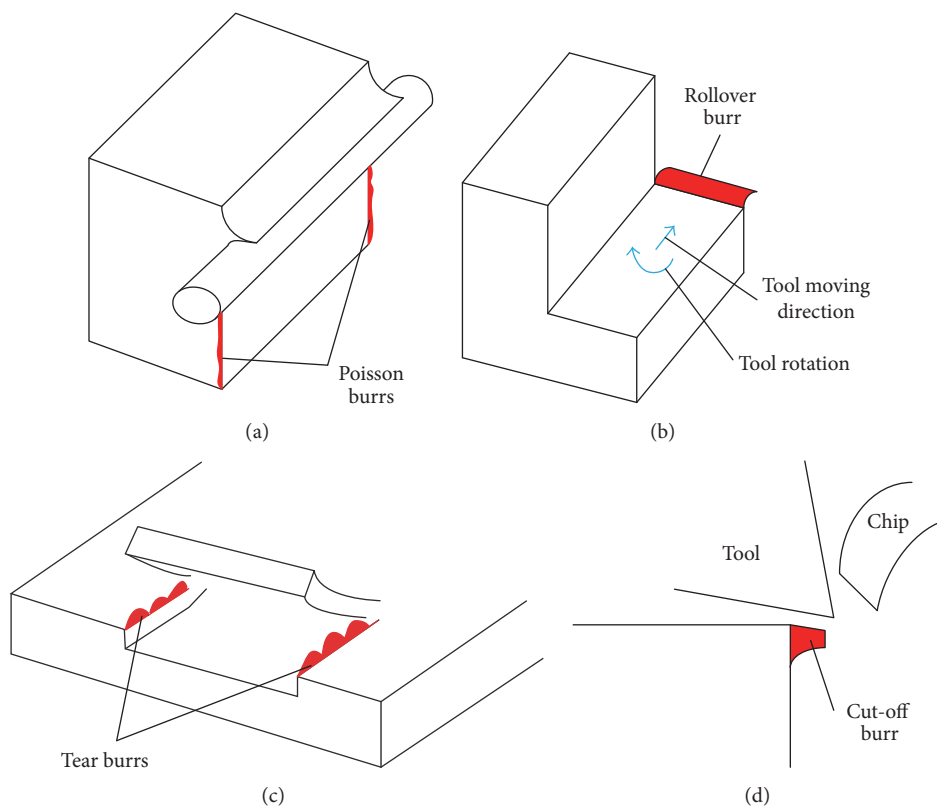


FIGURE 4: Schematic of machining burrs: (a) Poisson burr, (b) rollover burr, (c) tear burr, and (d) cut-off burr.

shearing, and it is obvious that the burrs are not formed by material bent for their shape. Therefore, the burr is speculated to be a typical kind of tear burr.

As the chip flow state is one of the important factors of the burr formation mechanism, plastic deformation in the adjacent microgrooving process should be considered. The workpiece material is pressed by the cutting tool, while the friction between the tool and material is ignored. Under these circumstances, the minimum resistance principle can be used to estimate the flow of the material macroscopically in plastic deformation. According to this principle, in the compression process, the particle of the plastic deformation

material always flows along the direction with the least resistance, which is the shortest normal of the object contour (Figure 5).

Different kinds of defects are formed according to the adjacent amount of microgrooves. Burrs are formed on the groove ridge with a large adjacent amount, while fracture pits occur with a small adjacent amount. The material flow condition is analysed by the minimum resistance principle, and the chip flow direction is estimated (Figure 6). According to the minimum resistance law, the section of the removed material is divided into four parts; the material flows of Part II and Part III are blocked by the workpiece material. Therefore,

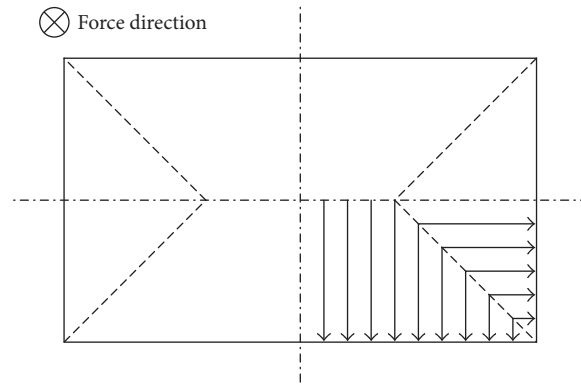


FIGURE 5: Diagram of minimum resistance principle.

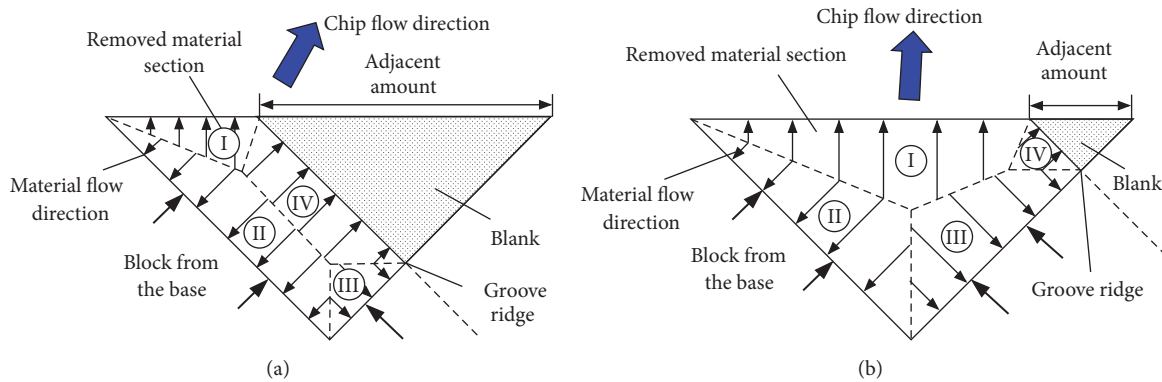


FIGURE 6: Material flow in the microgrooving under different conditions: (a) large adjacent amount and (b) small adjacent amount.

the chip flow direction is affected by the combination of material flow from Part I and Part IV. The estimated chip flow directions are shown. For the chip flow condition in Figure 6(a), the material near the groove ridge tends to be torn out from the workpiece. In this situation, tearing dominates the material removal process.

As seen in Figure 6(b), the cutting depth at the position of groove ridge is directly proportional to the adjacent amount. For the crystalline Ni-P material, fracture pits are observed on the groove ridge, and the brittle removal process is illustrated in Figure 7. The crack begins to appear when the cutting depth reaches the brittle-ductile transition thickness. With the movement of the cutting tool, the crack propagates, and brittle exfoliation of the material occurs on the surface. In this process, one single fracture pit is formed. For the gradual change of the pit depth, the cutting thickness decreases when the cutting edge of the tool reaches the brim of the fracture pit. In this situation, the material of this part would be removed in the ductile mode. As the cutting continues, the cutting tool recedes from the fracture pit, and the cutting depth returns to the original value. Afterwards, a new cycle of brittle removal begins. The morphology of discontinuous fracture pits forms in this process.

3.2. Analysis of Defect Formation by Small Cross-Angle Microgrooving Method. The adjacent amount is considered

to be the most important factor that decides the quality of the groove ridge according to the aforementioned research. The small cross-angle microgrooving method is proposed to analyse the forming mechanism of the groove ridge for different adjacent amounts. The procedure of the method is shown in Figure 8. After the machining of a microgroove, the workpiece is rotated with a small certain angle by the C-axis of the ultraprecision machine, and then the second microgroove that intersected with the first one is machined. A pair of gradient edges is generated by the intersection of the microgrooves.

Figure 9 shows the profile of the removed part of the second cutting, and the sections of the removed part at different positions of the gradient edge are marked. It can be observed that the shapes of the sections are similar to the removed part section of the parallel microgroove machined with an adjacent amount. Each section along the gradient edge could be matched with corresponding parallel microgroove machining sections shaped with different adjacent amounts. To confirm this result, the angles of the gradient edges formed by different cross angles of microgrooves in small cross-angle microgrooving experiments are calculated and shown in Table 1. The edge angle θ becomes larger as the microgroove cross-angle α increases. When the cross angle is in the range of $0^\circ \sim 10^\circ$, the edge angle varies within 0.5° , which is sufficiently small to be ignored. The change of the cross

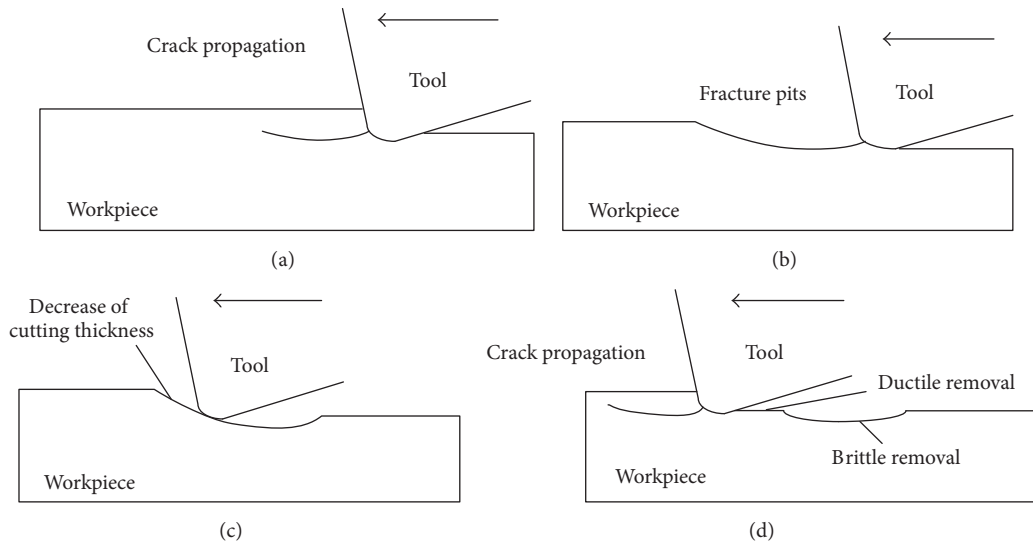


FIGURE 7: Material removing process of the crystalline Ni-P: (a) crack propagation, (b) brittle exfoliation, (c) ductile machining, and (d) formation of next fracture pit.

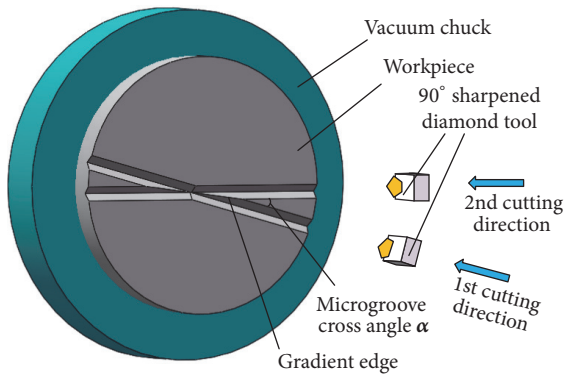


FIGURE 8: Experimental setup of small cross-angle microgrooving.

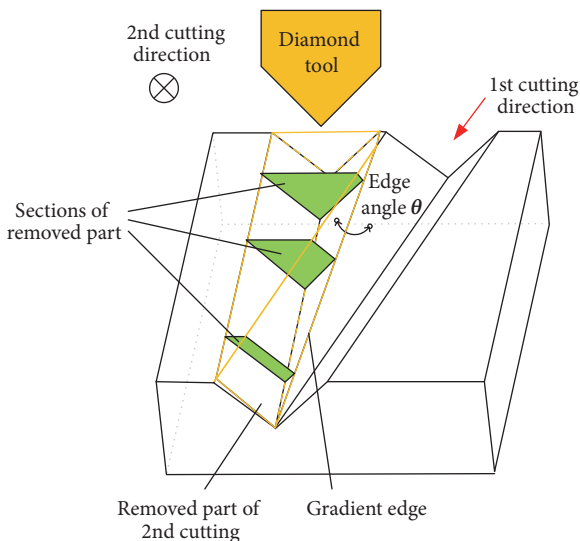


FIGURE 9: Sections of the removed material of the 2nd cutting.

TABLE I: Relationship between cross angle and gradient edge angle.

Microgroove cross-angle α (°)	Edge angle θ (°)
2	90.01745
5	90.10901
8	90.27880
10	90.43523

angle in this range has little effect on the shape of the removed section. The shape of the section could be considered to be the same as that of parallel microgroove machining.

The gradient edge formed in the small cross-angle microgrooving experiment is shown in Figure 10. Burrs and fracture pits are observed on the gradient edge, and there is no defect at the upper part of the gradient edge. The burrs are formed on the side of the first cutting direction. The fracture pits are discontinuous and mainly formed on the side of the second microgroove. At this point, the cutting depth at the position of groove ridge is less than the brittle-ductile transition thickness, and the material is removed in the ductile mode. The above signs show that the material removal mechanism in small cross-angle microgrooving experiments is the same as that of adjacent parallel microgroove machining with different adjacent amounts. Thus, it is reasonable to identify the defect formation mechanism in adjacent microgroove cutting processes through small cross-angle microgrooving experiments.

4. Defect Restriction by Controlling the Adjacent Amount

4.1. Influences of Microgrooving Parameters. To conduct a further study of the defect forming situation, a series of small cross-angle microgrooving experiments are carried out, and the experiment parameters are summarized in Table 2.

TABLE 2: Experiment parameters of small cross-angle microgrooving.

Cutting speed v (mm/min)	Depth of the 1st cutting d_1 (μm)	Depth of the 2nd cutting d_2 (μm)	Cross angle of microgrooves α ($^\circ$)
2400	3.0	3.0, 1.5	2, 5, 8, 10

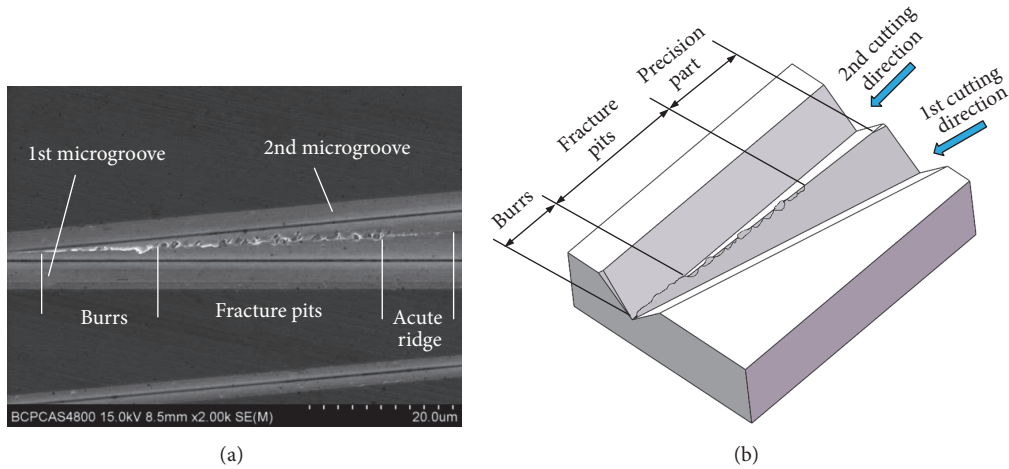


FIGURE 10: Gradient edge: (a) SEM photo and (b) overall schematic.

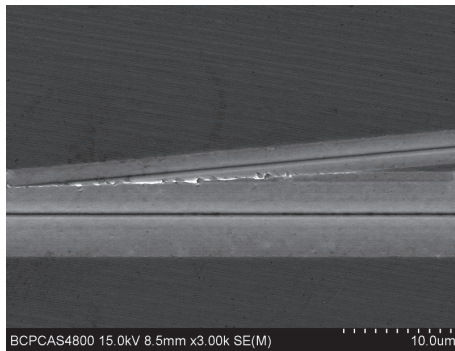
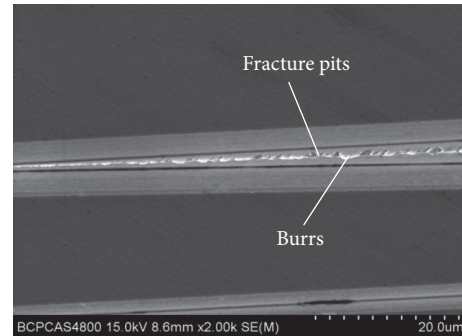
FIGURE 11: SEM photograph of gradient edge machined by cross of 1.5 μm microgroove.

FIGURE 12: SEM photograph of mix exists of burrs and fracture pits.

Several pairs of gradient edges are obtained and analysed. Gradient edges with larger sizes are created by the cross of microgrooves with larger cutting depths, while a smaller cross angle of the microgrooves makes the gradient edge slower with a certain height. Figure 11 shows a gradient edge machined by a 5° cross angle of microgrooves with a cutting depth of 1.5 μm . Burrs are clearly observed on the formed gradient edge, while fracture pits formation is not as evident as the example shown in Figure 10(a), whose size is larger. On one hand, it could be concluded that the formation of fracture pits, which is relevant to the brittle-ductile transition thickness of the material, is closely related to the cutting depth of the microgrooves. On the other hand, since the formation of the tear burr is related to the section of the removed material part, whether it would arise or not is not affected by the cutting depth of the microgroove. Figure 12 shows a gradient edge formed by microgrooves with a 2° cross angle. In this condition, the gradient edge is slower, and the defects

could be observed clearly in a sparse distribution. As seen in the figure, burrs and fracture pits coexist on the middle part of the gradient edge, which indicates that the forming mechanisms of these two defects are independent and have no effect on each other.

The high-quality part on the gradient edge corresponds to the acute ridge machined in the parallel microgrooving process. In theory, the high-quality parts of exit and entrance gradient edges should be the same length based on the previous research of the removed material section. However, it can be observed from the SEM photographs that the range of the high-quality region on the exit gradient edge is wider than that of the entrance gradient edge. In addition, the size of the fracture pits on the entrance gradient edge is larger (Figure 13). To summarize, the brittle-ductile transition occurs in a smaller adjacent amount on the exit gradient edge than the entrance gradient edge, and the phenomenon of brittle exfoliation is more remarkable on the entrance gradient edge.

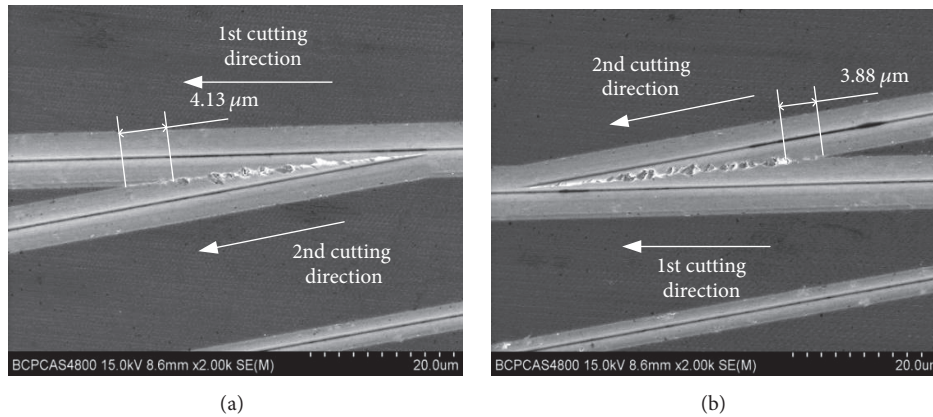


FIGURE 13: SEM photographs of: (a) exit gradient edge and (b) entrance gradient edge.

The removed material thickness on the edge increases with the diamond tool moving during the entrance gradient edge machining process. On one hand, the tensile stress between the chip and the undeformed surface material makes fracture pits easier to form on the brittle material. On the other hand, for the machining process of the exit part, the crack propagation and brittle exfoliation of the material on the edge are restrained by the hydrostatic pressure from the cutting tool. This explains why the quality of the exit gradient edge is better than that of the entrance, and the edge quality of adjacent microgrooves goes between them. For these reasons, the brittle-ductile transition positions of the exit and entrance gradient edges are, respectively, set as the upper and lower bounds for the brittle-ductile adjacent amount of microgroove machining.

4.2. Optimization and High-Quality Machining of Microgrooves. The corresponding adjacent amount of the position on the gradient edge could be obtained by geometric calculation, and the various brittle-ductile transition adjacent amounts achieved in the cross-cutting process under different cross angles are shown in Figure 14. The values of the adjacent amounts machined by different microgroove cross-angle degrees tend to be quite close, with no gradual change trend. Thus, the conclusion could be drawn that, under the test condition, the tiny change of the gradient edge shape has little effect on the brittle-ductile transition adjacent amount of the gradient edge, and the testing method is feasible. According to this method, when the adjacent amount is in the range of 570 nm~720 nm, the fracture pits begin to occur on the gradient edge, which is considered to be the transitional adjacent amount of the microgroove cut.

The defects of the machined microgroove array are difficult to repair due to the relocation difficulty of the tool and the workpiece in the machining process. Errors in submicron scale for the relative coordinate system of the workpiece surface established by tool setting, which would reflect the cutting depth, are unacceptable in ultraprecision machining. The actual cutting depth is the sum of the tool setting amount and the cutting feed, which is not an accurate value due to the uncertainty in the tool setting process. Therefore, estimations

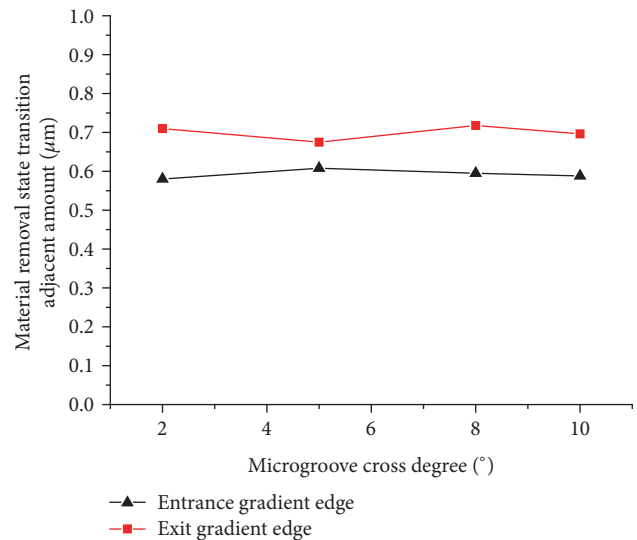


FIGURE 14: Effect of cross angle on transition adjacent amount in the material removal.

must be made to assure the high precision of the microgroove, and the prediction of the brittle-ductile transition adjacent amount provides guidance to the machining process. The cutting feed and interval of the microgrooves are rationally designed according to the tool setting conditions and depth of the microgrooves. The microgroove machining can be carried out in the appropriate adjacent amount where the material is removed in a ductile manner, and a microgroove mold with a high-quality ridge is obtained (Figure 15).

5. Conclusion

A new method to quickly estimate the appropriate adjacent amount range in a c-Ni-P mold microgrooving process is proposed. The theoretical model is established, and the brittle-ductile transition adjacent amount range of crystalline Ni-P plating is investigated for the optimization of the cutting conditions in a microgroove mold machining process. The main conclusions are as follows:

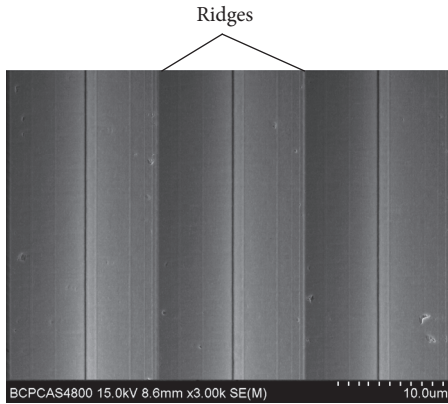


FIGURE 15: High-quality microgrooves with acute ridges.

(1) Two types of defects, namely, burrs and fracture pits, are found to coexist in the ultraprecision cutting of a Ni-P microgroove mold subjected to the adjacent amount of microgrooves.

(2) Small cross-angle microgrooving is an effective method to test the brittle-ductile transition region. The material removal and deformation mechanism on the gradient edge resemble that of microgrooves machining in different adjacent amounts.

(3) Generally, the quality on the exit gradient edge is superior to that on the entrance counterpart, and the ridge edge quality of adjacent microgrooves falls between them in the similar removed material section.

(4) For the crystalline Ni-P plating mold, the defects of burrs and fracture pits on the microgroove ridge can be effectively restrained when the microgroove adjacent amount is less than 570 nm.

Conflicts of Interest

The authors declare that they have no conflicts of interest.

Acknowledgments

This work has been financed by the National Key Basic Research Program of China (no. 2015CB059900) and the National Natural Science Foundation of China (no. 51375050). The authors would also like to acknowledge the support from the Fok Ying-Tong Education Foundation for Young Teachers in the Higher Education Institutions of China (no. 151052).

References

- [1] B. Guo, Q. Zhao, and X. Fang, "Precision grinding of optical glass with laser micro-structured coarse-grained diamond wheels," *Journal of Materials Processing Technology*, vol. 214, no. 5, pp. 1045–1051, 2014.
- [2] P. Li, J. Xie, J. Cheng, and Y. N. Jiang, "Study on weak-light photovoltaic characteristics of solar cell with a microgroove lens array on glass substrate," *Optics Express*, vol. 23, no. 7, pp. A192–A203, 2015.
- [3] K. Naessens, A. Van Hove, T. Coosemans et al., "Fabrication of microgrooves with excimer laser ablation techniques for plastic optical fibre array alignment purposes," in *Proceedings of the Laser Applications in Microelectronic and Optoelectronic Manufacturing V*, pp. 309–315, January 2000.
- [4] L. J. Yang, Y. Wang, Z. G. Tian, and N. Cai, "YAG laser cutting soda-lime glass with controlled fracture and volumetric heat absorption," *The International Journal of Machine Tools and Manufacture*, vol. 50, no. 10, pp. 849–859, 2010.
- [5] J. Shinozuka and Y. Imakama, "Effect of parallel micro-grooves fabricated on the rake and flank faces on the improvement of the cutting performance of low-rigidity elastomers," *Seimitsu Kogaku Kaishi/Journal of the Japan Society for Precision Engineering*, vol. 83, no. 7, pp. 679–686, 2017.
- [6] D. J. Stephenson, X. Sun, and C. Zervos, "A study on ELID ultra precision grinding of optical glass with acoustic emission," *The International Journal of Machine Tools and Manufacture*, vol. 46, no. 10, pp. 1053–1063, 2006.
- [7] T. Zhou, J. Yan, J. Masuda, and T. Kuriyagawa, "Investigation on the viscoelasticity of optical glass in ultraprecision lens molding process," *Journal of Materials Processing Technology*, vol. 209, no. 9, pp. 4484–4489, 2009.
- [8] T. Zhou, J. Yan, J. Masuda, T. Oowada, and T. Kuriyagawa, "Investigation on shape transferability in ultraprecision glass molding press for microgrooves," *Precision Engineering*, vol. 35, no. 2, pp. 214–220, 2011.
- [9] T. Zhou, J. Yan, and T. Kuriyagawa, "Size effects on transferability and mold change of glass molding press for microgrooves," *Advanced Materials Research*, vol. 497, pp. 235–239, 2012.
- [10] N. Al-Aqeeli, N. Saheb, T. Laoui, and K. Mohammad, "The synthesis of nanostructured WC-based hardmetals using mechanical alloying and their direct consolidation," *Journal of Nanomaterials*, vol. 2014, Article ID 640750, 16 pages, 2014.
- [11] S. Ji, L. Liu, J. Zhao, and C. Sun, "Finite element analysis and simulation about microgrinding of SiC," *Journal of Nanomaterials*, vol. 2015, Article ID 575398, 2015.
- [12] T. Zhou, J. Yan, Z. Liang, X. Wang, R. Kobayashi, and T. Kuriyagawa, "Development of polycrystalline Ni-P mold by heat treatment for glass microgroove forming," *Precision Engineering*, vol. 39, pp. 25–30, 2015.
- [13] H. Mekaru, C. Okuyama, T. Tsuchida et al., "Development of Ni-P-plated inconel alloy mold for imprinting on pyrex glass," *Japanese Journal of Applied Physics*, vol. 48, no. 6, pp. 06–FH0610, 2009.
- [14] J. Yan, T. Oowada, T. Zhou, and T. Kuriyagawa, "Precision machining of microstructures on electroless-plated NiP surface for molding glass components," *Journal of Materials Processing Technology*, vol. 209, no. 10, pp. 4802–4808, 2009.
- [15] X. Liu, T. Zhou, S. Pang, J. Xie, and X. Wang, "Burr formation mechanism of ultraprecision cutting for microgrooves on nickel phosphide in consideration of the diamond tool edge radius," *The International Journal of Advanced Manufacturing Technology*, pp. 1–7, 2017.
- [16] R. Kobayashi, S. Xu, K. Shimada, M. Mizutani, and T. Kuriyagawa, "Defining the effects of cutting parameters on burr formation and minimization in ultra-precision grooving of amorphous alloy," *Precision Engineering*, vol. 49, pp. 115–121, 2017.
- [17] Y. Liu, W. Zhao, T. Zhou, X. Liu, and X. Wang, "Microgroove machining on crystalline nickel phosphide plating by single-point diamond cutting," *The International Journal of Advanced Manufacturing Technology*, vol. 91, no. 1-4, pp. 477–484, 2017.

- [18] Y. Liu, W. Zhao, T. Zhou, X. Liu, and X. Wang, "Surface defect elimination in microgrooving of electroless nickel phosphide plating layer by brittleness enhancement," *The International Journal of Advanced Manufacturing Technology*, pp. 1–7, 2017.
- [19] J. C. Venter, K. Remington, J. F. Heidelberg et al., "Environmental genome shotgun sequencing of the sargasso sea," *Science*, vol. 304, no. 5667, pp. 66–74, 2004.
- [20] J. C. Aurich, D. Dornfeld, P. J. Arrazola, V. Franke, L. Leitz, and S. Min, "Burrs-Analysis, control and removal," *CIRP Annals - Manufacturing Technology*, vol. 58, no. 2, pp. 519–542, 2009.

Research Article

Fast-LPG Sensors at Room Temperature by α -Fe₂O₃/CNT Nanocomposite Thin Films

B. Chaitongrat  and **S. Chaisitsak** 

Department of Electronics, Faculty of Engineering, King Mongkut's Institute of Technology Ladkrabang, Bangkok 10520, Thailand

Correspondence should be addressed to S. Chaisitsak; sutichai.ch@kmitl.ac.th

Received 24 November 2017; Accepted 11 January 2018; Published 14 February 2018

Academic Editor: Chengyuan Wang

Copyright © 2018 B. Chaitongrat and S. Chaisitsak. This is an open access article distributed under the Creative Commons Attribution License, which permits unrestricted use, distribution, and reproduction in any medium, provided the original work is properly cited.

We present performance of a room temperature LPG sensor based on α -Fe₂O₃/CNT (carbon nanotube) nanocomposite films. The nanocomposite film was fabricated via the metallic Fe catalyst particle on CNTs in which both the catalyst particles and the CNT were simultaneously synthesized by chemical vapor deposition (CVD) synthesis and were subsequently annealed in air to create α -Fe₂O₃. These methods are simple, inexpensive, and suitable for large-scale production. The structure, surface morphologies, and LPG response of nanocomposite films were investigated. Raman spectroscopy and XPS analysis showed the formation of α -Fe₂O₃ on small CNTs (SWNTs). Morphological analysis using FE-SEM and AFM revealed the formation of the porous surface along with roughness surface. Additionally, the sensing performance of α -Fe₂O₃/CNTs showed that it could detect LPG concentration at lower value than 25% of LEL with response/recovery time of less than 30 seconds at room temperature. These results suggest that the α -Fe₂O₃/CNTs films are challenging materials for monitoring LPG operating at room temperature.

1. Introduction

Liquefied petroleum gas (LPG) is a complex mixture of hydrocarbon compounds, which mostly consist of propane (C₃H₈) and butane (C₄H₁₀). LPG is widely used as a combustion apparatus in a heater, cooking equipment, and automotive vehicles. Besides, LPG is of most harmful gases due to its flammable, explosive nature, which presents many hazards to the human being as well as environment. To avoid the damage caused by leaks and gas explosions, there is prevailing need to detect LPG leakage at the lower explosive limit (~2.0 vol.% of LPG) [1]. In last few decades, metal oxide semiconducting (MOS) materials have been extensively used as an LPG sensor [2, 3]. However, the optimal sensing properties of them operated along with high temperature (300–500°C). In such case, a heater needs to be installed for the sensors to function, causing increased power consumption, complexity, and investment budgets. To overcome these limitations, the fabrication of a LPG sensor operable at room temperature has gained essence importance [4, 5].

Many reports are available on the development of the LPG sensors that operate at room temperature, the reduction

of the MOS size [6, 7], and the mixing of MOS with metal nanoparticles [8] including the fabrication of heterojunctions [4, 9–11], which is one of the most strategies used. Due to the mixing of MOS and other materials, it formed a variety of the unique properties for sensing material, such as a change in conductance, improved surface catalytic property, increasing surface reaction sites, and producing a high porosity [12]. In addition, a formed contact potential at the interface between MOS and other nanostructured materials has also enhanced the sensing performance of a gas sensor [13, 14]. Therefore, more studies in fabricating devices based on heterojunctions are necessary, especially in nanostructure systems.

Iron oxide (Fe₂O₃) is n-type semiconductor, of which hematite (α -Fe₂O₃) is the most stable of Fe₂O₃. It has been widely studied for the various applications, including magnetic devices, pigments, catalysts, sensors, and medical fields [15]. In gas sensor applications, Fe₂O₃ has been continuously researched because it can provide high electron mobility, high chemical/thermal stability, multiple functions, and low cost [16, 17]. Recently, the nanostructures of Fe₂O₃ materials have attracted much attention as an effective material for various

gases because of their high surface activities, high surface-to-volume ratios, and high carrier mobility [18]. However, their electrical conductivity is limited, because it requires high temperatures to work [19]. Meanwhile, CNT can be considered as highly conductive material at room temperature. Additionally, CNTs have a hollow structure, nanosized morphology (diameter 1–10 nm), and high surface area (500–1500 m²/g) [20–24]. Therefore, CNTs have been used for mixtures enhanced in the conductivity of Fe₂O₃ at room temperature [19, 25]. Moreover, Fe₂O₃ and CNTs nanocomposites have been fabricated through asynchronous methods, and then the mixture of Fe₂O₃ and CNT has been deposited on the substrate, usually using the usually spinning and screen-printing technique [25, 26]. However, these techniques are the major performance-limiting factors in the sensor because of its inhomogeneous film thickness. Therefore, the sensor fabrication process also provides the enhancement in sensing performance, which can control the porosity and the roughness, resulting in the improvement of sensing properties of the sensor. Recently, a new strategy to synthesize metal nanoparticle/CNT hybrid materials has been reported. Both of the Fe catalyst particles and the CNT are simultaneously synthesized. Then, the metallic Fe was transformed into maghemite (α -Fe₂O₃) nanoparticles via a potential-cycling method [27].

Here, we report an effective approach to fabricate the α -Fe₂O₃/CNT nanocomposite films, in which the CNT was uniformly coated with α -Fe₂O₃ particles (α -Fe₂O₃/CNTs). According to our previous work [28], we found that the Fe catalyst particles adhere to as-grown CNTs. In this work, those particles were annealed in air to create α -Fe₂O₃ into CNTs films. In addition, we also demonstrate the application of the α -Fe₂O₃/CNTs thin films as a LPG sensor. Obtained results indicated that the response and recovery time of sensor have been significantly improved for detecting LPG at room temperature (28°C). Moreover, the sensing mechanisms of α -Fe₂O₃/CNTs-based LPG sensor were also discussed.

2. Experimental Section

2.1. Fabrication of α -Fe₂O₃/CNT Thin Films. An α -Fe₂O₃/CNTs films-based sensor was fabricated through the following processes. Firstly, as-grown CNTs were synthesized through the vertical floating catalyst chemical vapor deposition method (FC-CVD) using pyrolysing solutions of ethanol-ferrocene. The details of synthesized as-grown CNTs have been previously reported [28]. Briefly, a precursor was prepared by dissolving ferrocene powder (Fe (C₅H₅)₂; Sigma-Aldrich) in ethanol solution (C₂H₅OH; Carlo Erba) at a 0.25 wt.% ferrocene/ethanol ratio. The mist of precursor solution was carried into the 960°C reactor via argon (Ar) gas with a flow rate of 1000 sccm. The synthesized CNTs were collected onto a membrane filter directly from the FC-CVD reactor at the bottom of the reactor under room temperature (hereinafter called “as-grown CNTs”). The density of as-grown CNTs was controlled by adjusting deposition time (study; 15, 30, 45, 60, 90, and 120 min). Secondly, as-grown CNT films were then transferred from the filter to a slide glass or silicon (Si) substrate by pressing and then

dissolving the filter in acetone. Finally, the as-grown CNTs on substrate were put into a laboratory oven and annealed in air atmosphere at 350°C for 8 h to create α -Fe₂O₃ (hereinafter “ α -Fe₂O₃/CNTs”). In order to investigate the effect of stand-alone CNTs on the gas sensing properties, α -Fe₂O₃/CNTs films were purified by immersing in 3 M hydrochloric acid (HCl) to remove α -Fe₂O₃, resulting in a purified CNTs film (hereinafter called “purified CNTs”).

2.2. Characterizations. The characteristics of CNTs were analyzed by Raman spectroscopy (Renishaw inVia Reflex) with an Ar laser (514.5 nm) as the excitation source. The surface composition changes of as-grown and α -Fe₂O₃/CNTs were measured by X-ray photoelectron spectroscopy (XPS; PHI 5700), which were carried out on an AXIS Ultra DLD-X-ray photoelectron spectrometer using a monochromatic Al K _{α} source (1486.6 eV). In order to analyze the chemical functional group of the samples, the Fe 2p, O 1s, and C 1s core level were deconvoluted using the Shirley background function and Vigt fit. The surface morphology of films was performed by field-emission scanning electron microscopy (FE-SEM: JEOL, Hitachi s4700), atomic force microscopy (AFM: Park Systems XE100), and transmission electron microscopy (TEM: JEOL, JSM-2010). The sensor was placed into the chamber; N₂ (or zero air) and LPG were then injected via a mass flow controller unit (MFC). The gas sensing characteristics of the sensor were examined by monitoring changes in resistance with a constant voltage of 5 V, using Keithley source meter (Model 2004). Data acquisitions (DAQ), storage, and plotting in real time were realized using a personal computer with LabView™ software via a GPIB interface control.

3. Results and Discussion

3.1. Raman Spectroscopy Analyses. Figure 1(a) presents the Raman spectra of the as-grown CNT and α -Fe₂O₃/CNT nanocomposite films in the low-frequency (~100–500 cm⁻¹) region. The as-grown CNT films show several characteristic peaks at 162 and 267 cm⁻¹. These peaks are the Raman spectra in radial breathing mode (RBM: ~100–350 cm⁻¹) of the small-diameter CNTs (SWNTs: single-walled CNTs), which corresponded to the diameters (Φ_{SWNTs}) of the CNTs films varying in the range of 0.9–1.5 nm [29]. It is clearly seen from this figure that CNTs with 1.5 nm diameter remain after the anneal, while the small tube (0.9 nm) is easily burned at 350°C due to curvature strain [30]. In addition, Raman spectra of α -Fe₂O₃/CNT nanocomposite films also reveal additional peaks at 227, 244, 298, and 414 cm⁻¹ but these peaks are small signals (see inset of Figure 1(a)). These peaks remained after removing CNTs by annealing at 550°C, which can clearly observe the main peak at 298 cm⁻¹, 414 cm⁻¹, and 1320 cm⁻¹ and minor peaks at 227 cm⁻¹ and 244 cm⁻¹. These peaks are identified to the hematite (α -Fe₂O₃) nanostructure [31, 32].

Figure 1(b) presents the Raman spectra of the as-grown CNT and α -Fe₂O₃/CNT nanocomposite films in the high-frequency (~1200–1800 cm⁻¹). In the high-frequency regions,

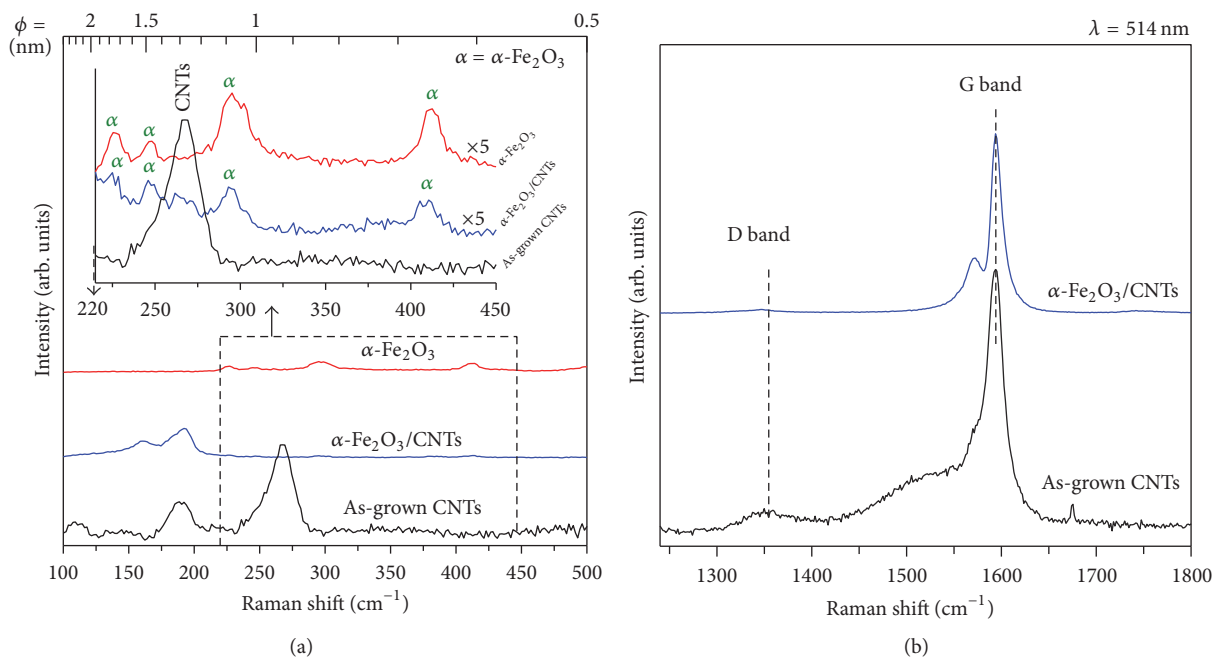


FIGURE 1: The Raman spectrum of the as-grown CNT and α -Fe₂O₃/CNT nanocomposite films measured in (a) low-frequency and (b) high-frequency regions. The inset in (a) shows a comparison between Raman spectra of as-grown CNTs, α -Fe₂O₃/CNTs, and α -Fe₂O₃ reference.

two apparent peaks at 1570 cm⁻¹ and 1590 cm⁻¹ are observed and correspond to the D and G band of CNTs [29]. The intensity ratio of G and D mode (I_G/I_D): a higher ratio indicates a lower defect, therefore, better structural quality [29]. I_G/I_D of as-grown CNT and α -Fe₂O₃/CNTs are 11.9 and 12.3, respectively. It can be seen that I_G/I_D of α -Fe₂O₃/CNT films had higher than that of as-grown CNT films. I_G/I_D results indicated that the purity of CNTs increased and the structure of CNTs was not damaged even when annealed in air.

3.2. XPS Analyses. The XPS technique is used to analyze chemical composition on the top surface of the materials (depth < 10 nm). Compositional elements can be identified by the peak position in terms of binding energy and the peak intensity (peak area) can be related to the amount of elements in the material.

Figure 2(a) demonstrates that the XPS survey spectrum of both as-grown CNTs and α -Fe₂O₃/CNT films was carbon (C 1s; ~284 eV), oxygen (O 1s; ~530 eV), silicon (Si 2p; ~100 eV), silver (Ag 3d; ~370 eV), and iron (Fe 2p; ~700 eV) [33–35]. In α -Fe₂O₃/CNT thin films, peak at 100 eV is observed and corresponds to silicon of silicon substrate; this is because of the ultra-thin films of the Fe₂O₃/CNTs. In addition, the atomic percent (At%) table (see the inset table) demonstrated that the O : Fe atomic ratio on the α -Fe₂O₃/CNT films was close to 2 : 3, which is probably Fe₂O₃ [25].

The phase analyses in α -Fe₂O₃ have been achieved via the Fe 2p deconvolution, as shown in Figure 2(b). The peaks in the Fe 2p spectrum were considered as species of Fe in films, which is referenced in the previous reports of Fe₂O₃ [36–38]. Fe 2p_{1/2} and Fe 2p_{3/2} are doublet spin orbit component

of Fe 2p. According to Figure 2(b), the as-grown CNT films were composed mostly of Fe metal, followed by Fe₃C (Fe-C), FeO, Fe₃O₄, and Fe₂O₃, respectively. After annealing, the dominant component in α -Fe₂O₃/CNT films was Fe₂O₃. In addition, two distinct peaks are observed at binding energies of 711.4 (Fe 2p_{3/2}) and 724.4 (Fe 2p_{1/2}) eV with a broad shake-up-satellite peaking at 719.3 eV. These peaks suggested that the phase formation of α -Fe₂O₃ was as good as those reported in the previous α -Fe₂O₃ studies [18, 36]. The occurrence of α -Fe₂O₃ is similar to that obtained by our Raman results. These results indicated that the most of Fe elements in α -Fe₂O₃/CNT films were α -Fe₂O₃, followed by the Fe₃O₄, Fe (OH)_x, and Fe-Si, respectively. The increase in intensity of the O 1s deconvoluted peak at 530.4 eV indicated that the surface of α -Fe₂O₃ had mostly adsorbed oxygen ions [39], as shown in Figure 2(c). The peaks at 532.4, 533.4, and 534.2 eV corresponded to carboxylate/carbonyl (O=C=O/C=O), epoxy/hydroxyl (C-O-C/C-OH), and silicon oxide (Si-O) respectively. It should be noted that the α -Fe₂O₃/CNTs showed the occurrence of a new peak at 531.7 eV (in O 1s deconvolution; Figure 2(c)) and that Fe-C (in Fe 2p deconvolution; Figure 2(b)) disappeared. This may be that bonding of metallic Fe and CNTs (Fe-C) was changed to α -Fe₂O₃ and CNTs (Fe-O-C), of which Fe atom and CNTs were contacted via carbonyl groups (-O-C). The peak at 531.7 eV, therefore, possibly is assigned to the binding of α -Fe₂O₃ and oxygen functional group on CNTs through Fe-O-C bonds.

Furthermore, more structure and characterization of the CNTs were carried out by the C 1s deconvolution [39], as shown in Figure 2(d). Both of as-grown CNT and α -Fe₂O₃/CNT films presented the main peak at 284.9 eV, which can be assigned the C 1s (Sp²) binding energy of CNTs. The

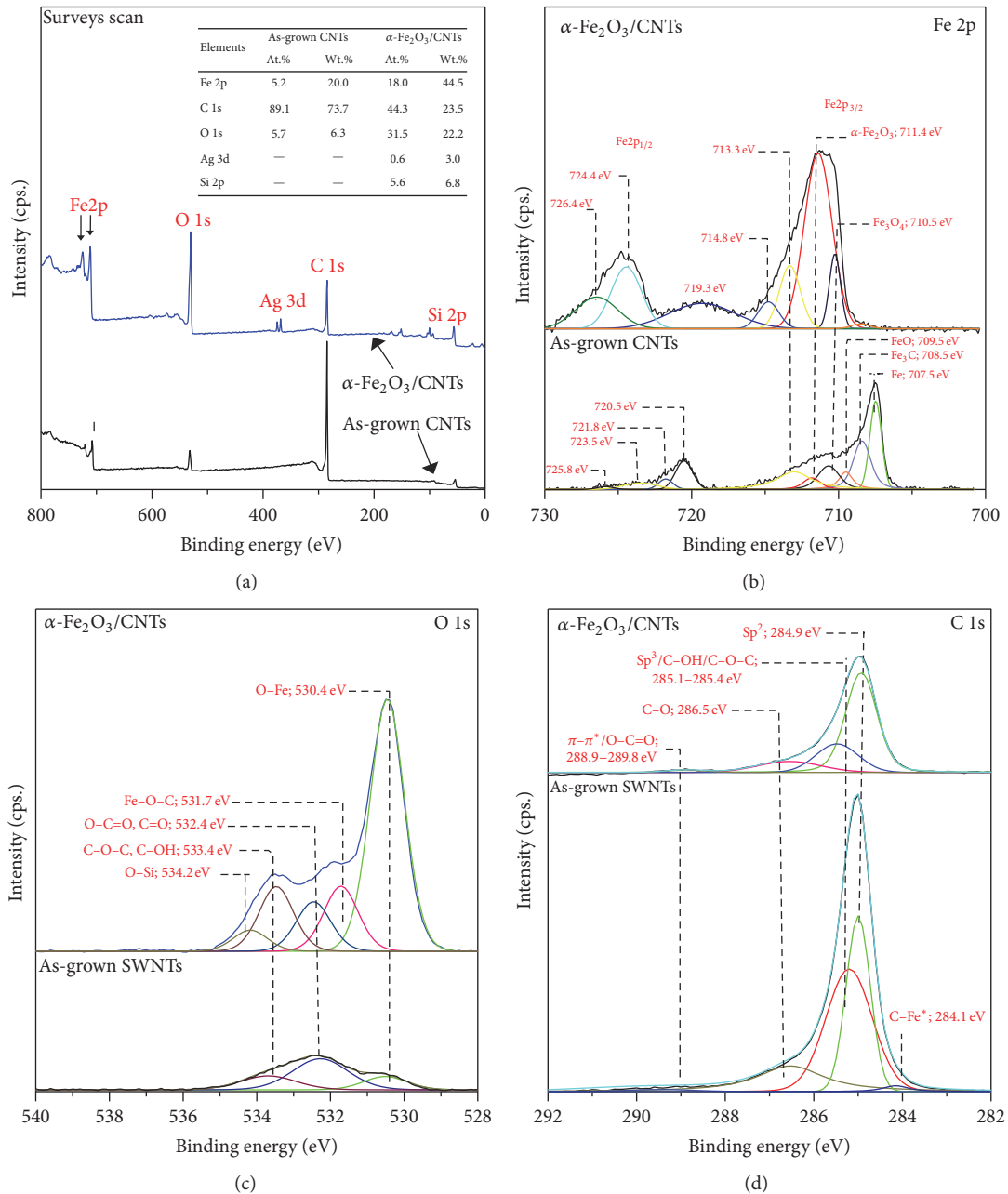


FIGURE 2: (a) XPS survey scan of as-grown CNTs and α -Fe₂O₃/CNT films. (b) XPS deconvolution of (b) Fe 2p, (c) O 1s, and (d) C 1s. The inset in (a) shows the atomic percent (At%) and weight percent (Wt%) of as-grown CNTs and α -Fe₂O₃/CNT films.

peaks in the shoulder of the main peak at 285.1–285.4, 286.5, and 288.9–289.8 eV could be assigned to Sp³/C–OH/C–O–C, C–O, and π – π^* /O–C=O, respectively. Sp³ was attributed to amorphous carbon/defects in the nanotube structure, which, at this defect, could be grafted to the –OH and –C–O [40, 41]. It is widely recognized that the mixing of oxide NPs by the formation of nucleus Fe⁺ on CNTs induces damage in CNTs [25]. However, our method did not further significantly affect the CNTs due to the Fe spontaneously grow and uniformly assemble on the entire surface of each nanotube by CVD. In addition, the sp²/sp³ ratio of the α -Fe₂O₃/CNT films was

higher than that of the as-grown CNT films. This is consistent with I_G/I_D ratios in the Raman results, implying that the structure of CNTs was not damaged even when annealed in air.

3.3. FE-SEM/AFM Analyses. From the obtained results from XPS and Raman spectroscopy, it is confirmed that the as-grown CNTs were decorated with metallic Fe. However, these metallic Fe could be easily transformed to α -Fe₂O₃ by air annealing. In this section, we investigated that the

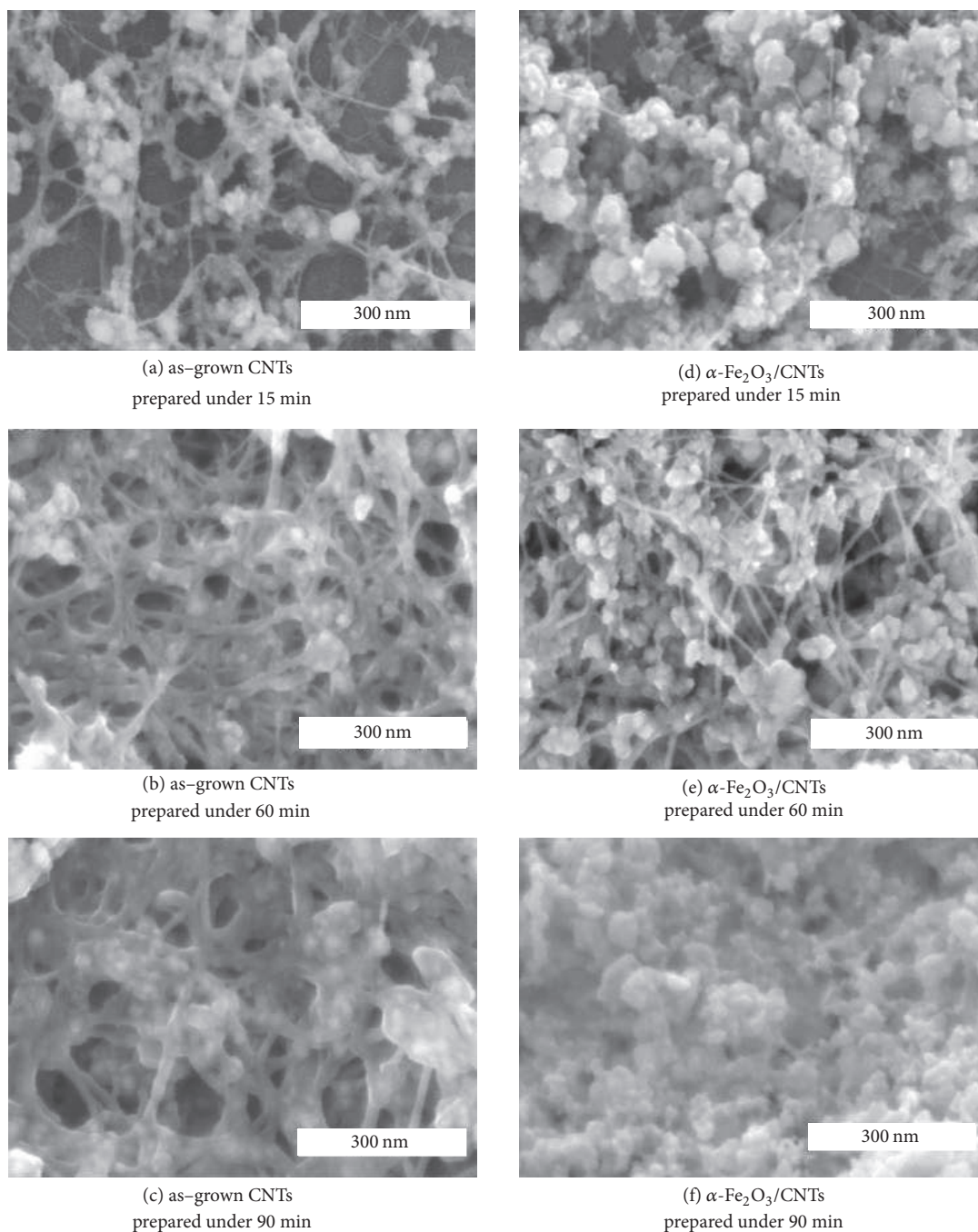


FIGURE 3: Morphology of (a–c) as-grown CNT films and (d–f) α -Fe₂O₃/CNT composite films on glass substrate.

variation of deposition time effected on the morphology of α -Fe₂O₃/CNTs.

Figures 3(a)–3(c) present the SEM images of as-grown CNT films on silicon substrates, which were prepared at different deposition times of 15, 60, and 90 min, respectively. As-grown CNT films consist of CNTs and metallic Fe particles. The decrease in the distribution of CNTs and Fe particles suggest that the density of CNTs and Fe particles increases with increasing the deposition time. In addition, the hydroxide (OH⁻) part was observed onto CNTs and Fe

particles in XPS result. These components may be attributed to the remained filters. The CNTs were the loosely packed and were consisted of the randomly oriented entangled CNT bundles, which were decorated with Fe NPs (size averaged 7.33 nm in diameter; Supplement Figure S1).

Figures 3(d), 3(e), and 3(f) present the SEM images of α -Fe₂O₃/CNT films prepared with different deposition time of 15, 60, and 90 min, respectively. The hydroxide part was removed during air annealing leading to the formation of α -Fe₂O₃ nanoparticles. It is seen that the CNTs network with

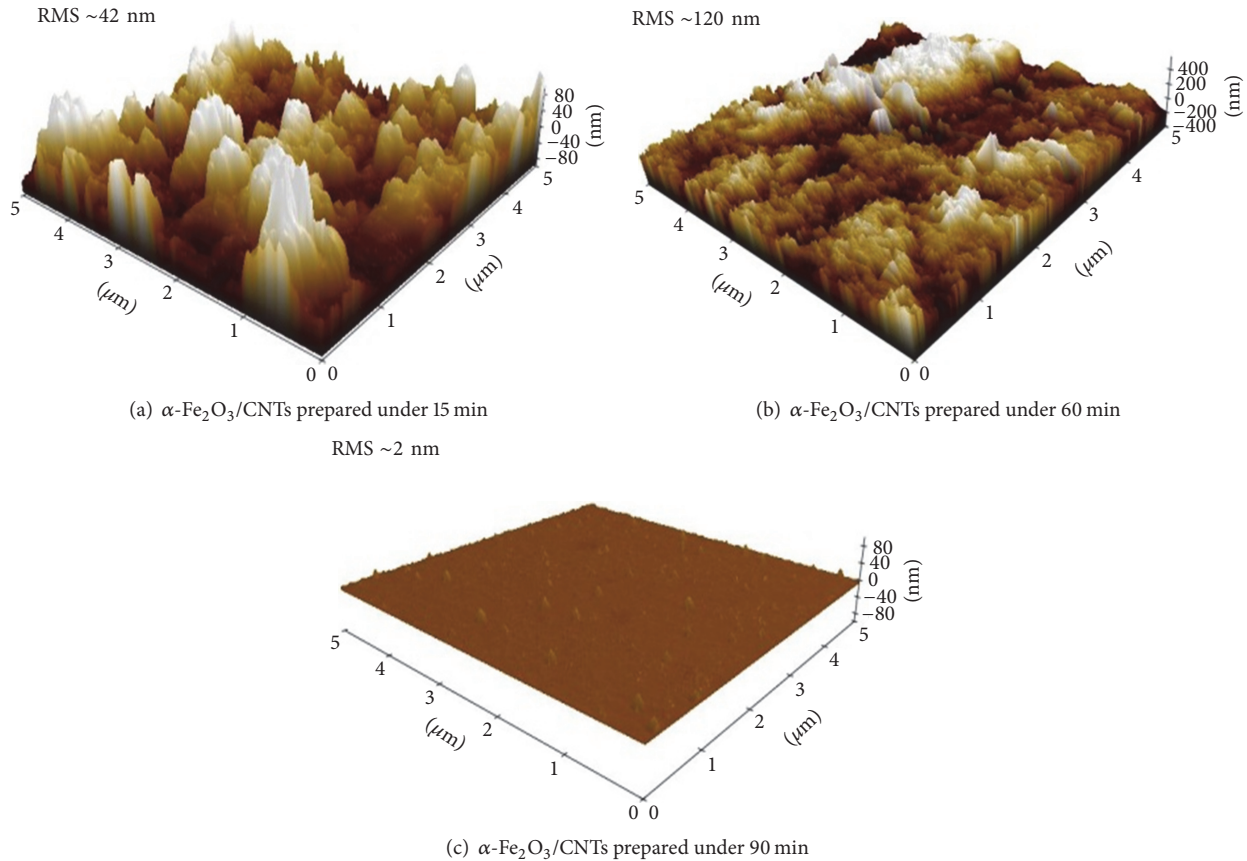


FIGURE 4: Morphology of surface measured using AFM on samples of the α -Fe₂O₃/CNT films with different deposition times. The 3D images recorded at $5 \mu\text{m} \times 5 \mu\text{m}$ planar in contact mode.

interconnected α -Fe₂O₃ nanoparticles is formed in Figures 3(d) and 3(e). In addition, the small agglomeration of the α -Fe₂O₃ particles is also observed at the interconnections of network structure along leading to the formation of the high porous surface. The α -Fe₂O₃/CNT structure with high porous is beneficial towards LPG sensing application because of the gas molecules enable to enter quickly through the porous structure.

Figures 4(a), 4(b), and 4(c) present that the AFM images of α -Fe₂O₃/CNT films. Root mean square (RMS) roughness of α -Fe₂O₃/CNT films is ~42, ~120, and ~2 nm for α -Fe₂O₃/CNT films prepared under deposition time of 15, 60, and 90 min, respectively. In our previous report [47], the sensor response of LPG sensor increases as a result of the high RMS value, because of the increase in the number of the active adsorption sites for oxygen or hydrocarbon molecules on the sensor surfaces.

According to SEM and AFM observations, it is seen that the porous structure and the surface roughness of α -Fe₂O₃/CNT films were controlled by deposition time along with spatial distribution of CNTs and α -Fe₂O₃ particles. SEM and AFM images (Figures 3(f) and 4(a)) of such α -Fe₂O₃/CNT films prepared under deposition time of 90 min clearly indicate that their surface had a bulk structure and low roughness. For a spatial distribution of Fe₂O₃/CNT films

under prepared 90 min, small particles were closed together and easily aggregated into a flat surface with reduced surface area of α -Fe₂O₃/CNT films. Obtained results indicated that choosing a suitable deposition time could generate α -Fe₂O₃/CNT films along with a highly porous structure and high roughness.

3.4. Sensing Properties of LPG Sensors. The sensor response to LPG was defined as $S(\%) = (|\Delta R|/R_g) \times 100\%$, ΔR is $R_a - R_g$, where R_g and R_b denote the resistance of sensor when exposed to LPG gas and that when exposed to baseline gas, respectively [48]. Response/recovery time [49] is an important sensing performance indicator for a sensor to detect a flammable gas. A sensor's response time ($T_{\text{resp.}}$) is defined as 90% change in resistance from its baseline value to the maximum value in the presence of LPG. Recovery time ($T_{\text{rec.}}$) is defined as the time required for recovering of the original resistance. In the examination of the sensor, carbon conductive electrodes were added onto the top of sensing films.

Figures 5(a), 5(b), and 5(c) display the change in the resistance of as-grown CNTs, α -Fe₂O₃/CNTs, and purified CNTs sensors in the presence of LPG at various concentrations. The baseline resistances in N₂ for as-grown CNTs, α -Fe₂O₃/CNTs, and purified CNTs were approximately 2.5 k Ω , 1.9 M Ω , and 360 k Ω , respectively. Figure 5(a) presents that

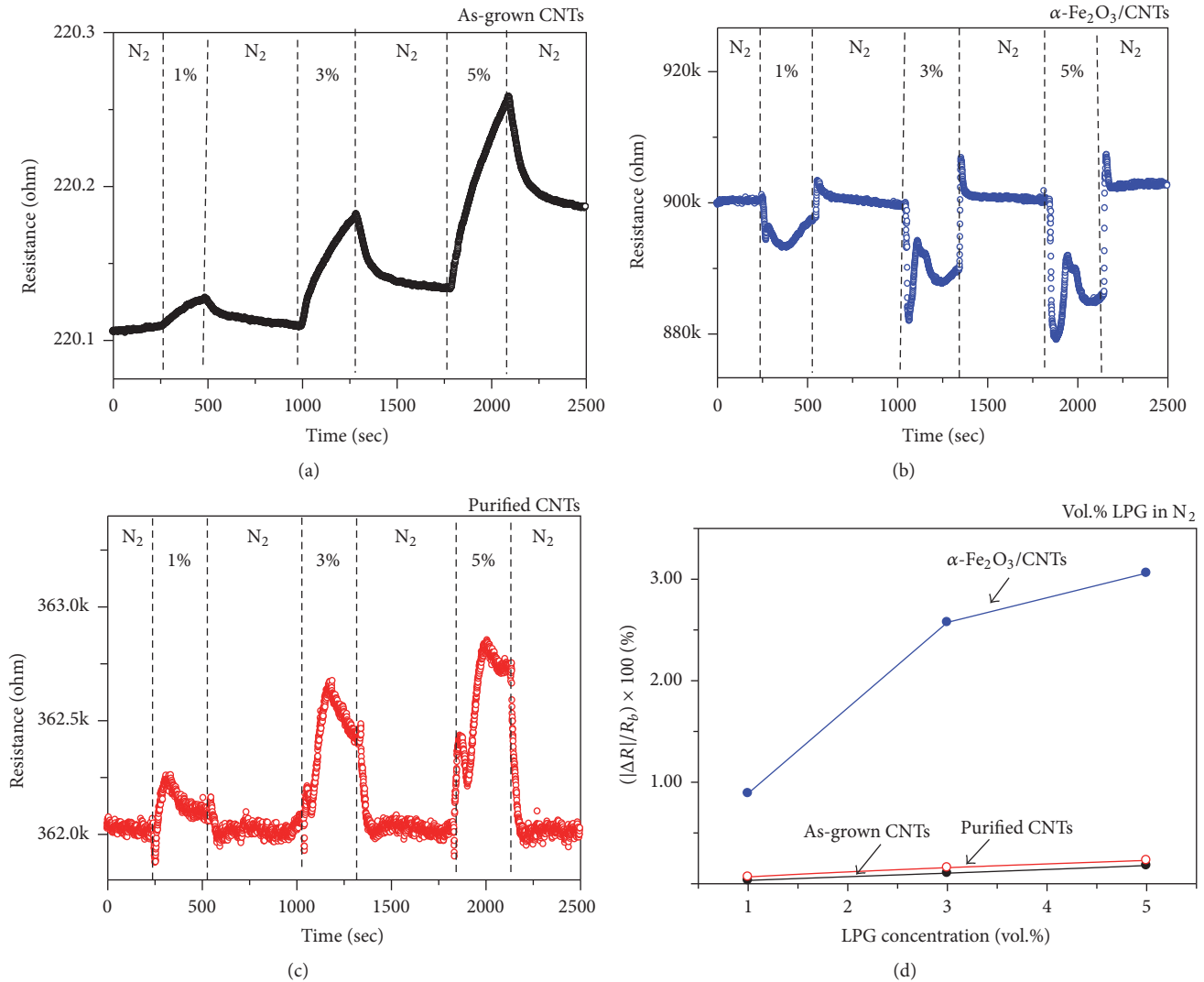


FIGURE 5: Dynamic responses of (a) as-grown CNTs; (b) $\alpha\text{-Fe}_2\text{O}_3/\text{CNTs}$; and (c) purified CNTs to LPG in air atmosphere. (d) demonstrates sensor responses by sensor type to varying LPG concentrations of 1–5 vol.%.

the p-type LPG sensing behavior is observed for as-grown CNTs, which resulted from the CNTs sensing while the Fe catalyst was encapsulated with carbon [27]. Meanwhile, $\alpha\text{-Fe}_2\text{O}_3/\text{CNT}$ films display an n-type sensing behavior due to the formations of $\alpha\text{-Fe}_2\text{O}_3$ that act as LPG sensing. It is well known that the sensing behavior of gas sensor has been related to the properties of sensing materials such as p-type material, which had hole majority carriers. The amount of hole will be decreased dramatically when reducing gas (LPG) exposure, due to the fact that an electron of reducing gas was injected to p-type material resulting in increased resistance of the sensor [50]. This could explain the sensing behavior of as-grown CNTs and $\alpha\text{-Fe}_2\text{O}_3/\text{CNTs}$ composite based on LPG sensor. Figure 5(c) clearly depicts that the sensing behavior of CNTs without $\alpha\text{-Fe}_2\text{O}_3$ is of p-type.

Figure 5(d) presents the sensor response, and $\alpha\text{-Fe}_2\text{O}_3/\text{CNT}$ films showed the maximum in response along with fast response/recovery time, while as-grown CNT and purified CNT films had a low response. This was due to the fact that

high bonding energy among LPG atoms allows limited electron transfer from LPG molecules to the CNTs [51]. However, the purified CNTs had a quick response/recovery time because of the highly purified CNTs than that of CNT films. These results indicated that the $\alpha\text{-Fe}_2\text{O}_3/\text{CNT}$ films had an excellent responsive to detect the LPG.

Moreover, we observed that the time response of $\alpha\text{-Fe}_2\text{O}_3/\text{CNTs}$ was faster than that of as-grown CNTs. This observation can be explained by the different sensing mechanism. For as-grown CNT films, the response is attributed to the adsorption between the LPG and the surface of the carbon nanotube. On the other hand, the fast response of $\alpha\text{-Fe}_2\text{O}_3/\text{CNT}$ films might be due to the sensing process of the interface between the CNTs and the $\alpha\text{-Fe}_2\text{O}_3$. According to this mechanism, the quick response of $\text{Fe}_2\text{O}_3/\text{CNT}$ -based sensors could be attributed the Schottky barrier formed at $\alpha\text{-Fe}_2\text{O}_3$ and CNTs junction [52]. Moreover, the annealing in air could improve the response time of $\alpha\text{-Fe}_2\text{O}_3/\text{CNT}$ films [53].

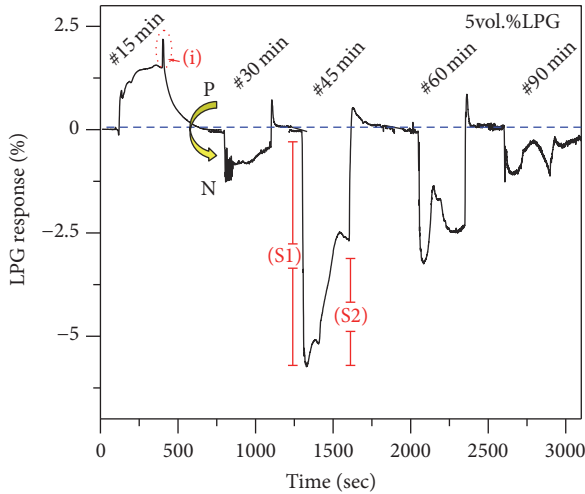


FIGURE 6: Sensing performances of $\alpha\text{-Fe}_2\text{O}_3/\text{CNT}$ films prepared under varying the deposition time of 15, 30, 45, 60, and 90 min.

In next section, we investigated the effect of the deposition time on LPG sensing, as showed in Figure 6. “S1” and “S2” are defined as the sensor response of n- and p-type, respectively. The $\alpha\text{-Fe}_2\text{O}_3/\text{CNT}$ films were prepared under varying deposition time of 15, 30, 45, 60, and 90 min. For the sensing behavior of $\alpha\text{-Fe}_2\text{O}_3/\text{CNT}$ films, we found that the $\alpha\text{-Fe}_2\text{O}_3/\text{CNT}$ films present the both of n- and p-type behavior. However, notable behaviors of the sensor were attributed to the deposition time. $\alpha\text{-Fe}_2\text{O}_3/\text{CNT}$ s prepared for 15 min showed the p-type sensing behavior while $\alpha\text{-Fe}_2\text{O}_3/\text{CNT}$ s prepared under deposition time of 30, 45, 60, and 90 min presented n-type sensing behavior. Note that the resistance of the $\alpha\text{-Fe}_2\text{O}_3/\text{CNT}$ composites prepared under the deposition time of 120 min was also investigated, because of its extremely high resistance at room temperatures, which is out of the range of our instrument. Moreover, SEM and AFM images of $\alpha\text{-Fe}_2\text{O}_3/\text{CNT}$ films indicated that the choosing a suitable deposition time could be generated the $\alpha\text{-Fe}_2\text{O}_3/\text{CNT}$ films along with a highly porous structure and high roughness. This could explain the $\alpha\text{-Fe}_2\text{O}_3/\text{CNT}$ films prepared under deposition time of 45 min, which is the maximum response of ~6% to 5 vol.% of LPG.

To examine the sensor’s multiple-cycle sensing performance under air environment, the $\alpha\text{-Fe}_2\text{O}_3/\text{CNT}$ films were measured under at various concentrations of 0.1, 0.4, and 0.7 vol.% of LPG diluted in zero air, as shown in Figure 7. The electrical resistance of sensors decreased upon LPG exposure and increased after replacing LPG with zero air. The sensor response, response, and recovery times of $\alpha\text{-Fe}_2\text{O}_3/\text{CNT}$ s on Figure 7 are summarized in Figure 8. It is observed that the sensor response and response/recovery times were stable and nearly equal at each concentration, indicating a good reproducibility of the sensing performance. Moreover, the $\alpha\text{-Fe}_2\text{O}_3/\text{CNT}$ films could detect LPG at concentration levels of less than 0.5 vol.% of LPG, which corresponds to 25% LEL of LPG. Note that LEL (lower explosive limit) is defined as the minimum level of concentration of LPG contained in the

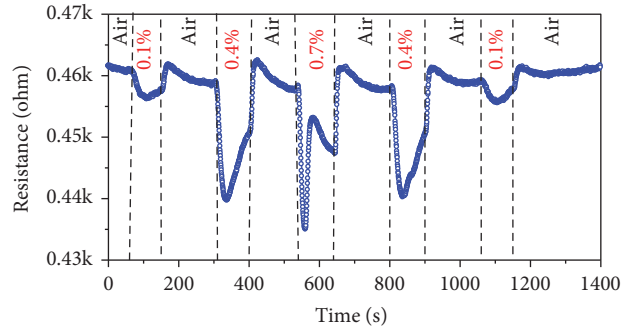


FIGURE 7: Dynamic responses of $\alpha\text{-Fe}_2\text{O}_3/\text{CNT}$ composite films to LPG concentrations varying from 0.1 to 0.7 vol.% in a different mix environment of air.

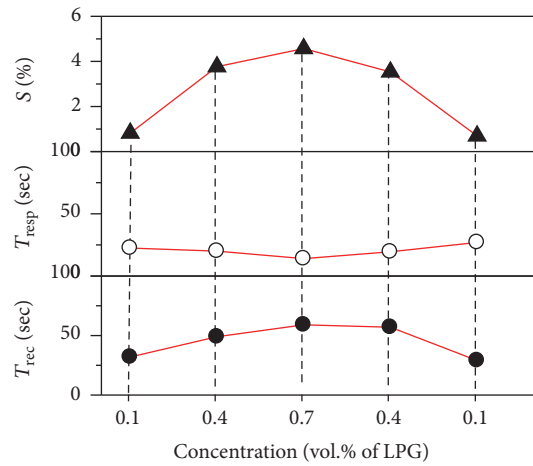


FIGURE 8: Summarizing the sensing properties of $\alpha\text{-Fe}_2\text{O}_3/\text{CNT}$ composite films to LPG concentrations varying from 0.1 to 0.7 vol.% in a different mix environment of air.

air sufficient enough to propagate a flame when exposed to a source of ignition.

3.5. LPG Sensing Mechanism. The sensing mechanism of the reducing gas (electron donors) like LPG results from the chemical reaction (between LPG molecules and the surface of materials) and relates to change in electrical properties of the samples, as discussed in many reports [48, 54]. For example, LPG sensing of the n- Fe_2O_3 semiconductor has been shown to be n-type sensing behaviors due to reducing in resistance when exposed to LPG [18]. In air, oxygen molecules in the ambient air absorb continuously on the empty absorption sites Fe_2O_3 , which can be described by the following equations:

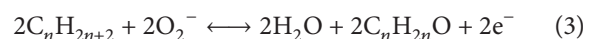
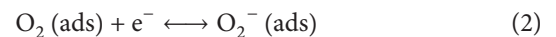


TABLE 1: Nanocomposite materials-based LPG sensors operating at room temperature.

Years [ref.]	Materials	LPG (vol.%)	S (%)	$T_{resp.}/T_{rec.}@90\%$
2011 [1]	Ferric oxide	2.0	5100.0	~120 s/~150 s
2013 [4]	Ppy/TiO ₂	0.10	55.0	~112 s/~130 s
2013 [11]	PTh/SnO ₂ hybrid	0.5–2.5	~9.5–56.2	196–94 s/182–466 s
2014 [42]	CuO-SnO ₂	0.5	~4200.0	~180 s/~200 s
2014 [10]	PANI/ γ -Fe ₂ O ₃	0.02	~140	~60 s/N/A
2014 [43]	ZnFe ₂ O ₄	5.0	~1600.0	~120 s/~150 s
2014 [44]	Cu ₂ ZnSnS ₄	0.12	~20.0	~70 s/~40 s
2016 [45]	Cu ₂ ZnSnS ₄	0.1	~60.0	~40 s/~40 s
2017 [46]	BaTiO ₃	0.5	50	~30 s/~60 s
This study	As-grown CNTs	5.0	~0.25	~290 s/N/A
	Purified CNTs	5.0	~0.25	~20 s/45 s
	α -Fe ₂ O ₃ /CNTs	0.1–5.0	~1.0–6.0	~25–13 s/~30–80 s

According to (1)–(3), the oxygen extracts electrons from the conduction band of Fe₂O₃ to form O₂⁻ (at room temperature), leading to an increase in resistance [25]. When Fe₂O₃ is exposed to LPG (C_nH_{2n+2}), O₂⁻ on the film surface interacts with the LPG molecules and produces gas intermediates (C_nH_{2n}:O), water (H₂O) vapor, and electron. An electron in (3) led to a decrease in resistance of Fe₂O₃ materials. In contrast, p-CNTs presented the resistance reduced upon exposure to LPG, showing p-type sensing behaviors, as illustrated in sensor response of as-grown CNTs (see in Figure 5).

Moreover, all α -Fe₂O₃/CNT films exhibited excessive recovery (point “i” in Figure 6), which is similar to that reported by Dai et al. in a gas sensor made of monolayer α -Fe₂O₃ [55]. They explained the excessive recovery due to the one-electron response, one initial electron recovery, and two-electron eventual recovery. In our work, the one-electron response has received from the LPG molecules; the two-electron recovery might be received from the oxygen/substance intermediates gas (C_nH_{2n}O) which may be due to the high active site on α -Fe₂O₃.

The advantageous properties of the CNTs-based gas sensor are high sensitivity and fast response; however, the CNTs-based LPG sensor is slow to respond and slow to recover. This was due to the fact that high bonding energy among LPG atoms allows limited electron transfer from LPG molecules to the CNTs [51]. In our experiment, the α -Fe₂O₃/CNTs-based LPG sensor’s improved response was achieved by converting Fe, which served as catalyst for the growth of CNTs, to α -Fe₂O₃, causing an increase in LPG active sites in the CNTs. In addition, the porous morphology and the new characteristics of the nanocomposite materials such as n-Fe₂O₃/p-CNT nanocomposites make it possible to improve LPG sensing performance. Further investigations are required to clarify this kind of sensing mechanism, which will be undertaken in our future work. Moreover, our literature review shows that various materials have been used in LPG sensor applications intended for room temperature use, as shown in Table 1. Our α -Fe₂O₃/CNT films-based LPG sensors exhibited a fast response/recovery time, indicating the promise of possible applications in LPG leak detection at room temperature.

4. Conclusions

A simple fabrication of liquid petroleum gas sensor based on α -Fe₂O₃/CNT nanocomposite films is reported. α -Fe₂O₃/CNT films were successfully synthesized through the vertical floating catalyst chemical vapor deposition method (FC-CVD) using ferrocene-ethanol mist. To fabricate a sensor, the metallic Fe particles on CNTs were changed into α -Fe₂O₃ by annealing in air at 350°C. Raman spectroscopy, XPS analysis, SEM, and AFM images reveal the Fe₂O₃/CNT structure with porous and roughness structure. The sensing performance of the sensor was tested at room temperature. The sensing performance of α -Fe₂O₃/CNTs showed that it could detect LPG concentration at lower value than 25% of LEL with response/recovery time of less than 30 seconds at room temperature. These results suggest that the α -Fe₂O₃/CNTs films are a challenging material for monitoring LPG operating at room temperature.

Conflicts of Interest

The authors declare that there are no conflicts of interest regarding the publication of this paper.

Acknowledgments

The authors are grateful to the Western Digital (Thailand) for the Raman measurements. The work has been supported, in part, by the King Mongkut’s Institute of Technology Ladkrabang (KMITL) Research Fund. B. Chaitongrat gratefully acknowledges the financial support for this work provided by the Higher Education Research Promotion and National Research University Project of Thailand, Office of the Higher Education Commission.

Supplementary Materials

Figure S1: (a) TEM images which represent iron nanoparticles (Fe NPs) at surface of the growth of CNTs; (b) particle-size distribution of the Fe NPs performed by measuring 45

individual NPs on the TEM images. Figure S1(a) shows the TEM image of the as-grown CNT films, which consisted of the randomly oriented entangled CNTs. The small-diameter CNTs were coated with Fe NPs, and some of these CNTs were coated with Fe NP clusters. These NPs were metallic iron (using XPS). An estimation of the distribution of Fe NPs' sizes performed by measuring each NP obtained from TEM images yielded an average particle size of ~ 7.33 nm, as shown in Figure 1S(b). (*Supplementary Materials*)

References

- [1] B. C. Yadav, S. Singh, and A. Yadav, "Nanonails structured ferric oxide thick film as room temperature liquefied petroleum gas (LPG) sensor," *Applied Surface Science*, vol. 257, no. 6, pp. 1960–1966, 2011.
- [2] B. Thomas and B. Skariah, "Spray deposited Mg-doped SnO₂ thin film LPG sensor: XPS and EDX analysis in relation to deposition temperature and doping," *Journal of Alloys and Compounds*, vol. 625, pp. 231–240, 2015.
- [3] F. Pourfayaz, A. Khodadadi, Y. Mortazavi, and S. S. Mohajerzadeh, "CeO₂ doped SnO₂ sensor selective to ethanol in presence of CO, LPG and CH₄," *Sensors and Actuators B: Chemical*, vol. 108, no. 1-2, pp. 172–176, 2005.
- [4] R. N. Bulakhe, S. V. Patil, P. R. Deshmukh, N. M. Shinde, and C. D. Lokhande, "Fabrication and performance of polypyrrole (Ppy)/TiO₂ heterojunction for room temperature operated LPG sensor," *Sensors and Actuators B: Chemical*, vol. 181, pp. 417–423, 2013.
- [5] V. Talwar, O. Singh, and R. C. Singh, "ZnO assisted polyaniline nanofibers and its application as ammonia gas sensor," *Sensors and Actuators B: Chemical*, vol. 191, pp. 276–282, 2014.
- [6] S. Singh, A. Singh, M. Wan et al., "Fabrication of self-assembled hierarchical flowerlike zinc stannate thin film and its application as liquefied petroleum gas sensor," *Sensors and Actuators B: Chemical*, vol. 205, pp. 102–110, 2014.
- [7] S. Singh, V. Gupta, B. C. Yadav, P. Tandon, and A. K. Singh, "Structural analysis of nanostructured iron antimonate by experimental and quantum chemical simulation and its LPG sensing," *Sensors and Actuators B: Chemical*, vol. 195, pp. 373–381, 2014.
- [8] D. Haridas, A. Chowdhuri, K. Sreenivas, and V. Gupta, "Enhanced room temperature response of SnO₂ thin film sensor loaded with Pt catalyst clusters under UV radiation for LPG," *Sensors and Actuators B: Chemical*, vol. 153, no. 1, pp. 152–157, 2011.
- [9] D. S. Dhawale, R. R. Salunkhe, U. M. Patil, K. V. Gurav, A. M. More, and C. D. Lokhande, "Room temperature liquefied petroleum gas (LPG) sensor based on p-polyaniline/n-TiO₂ heterojunction," *Sensors and Actuators B: Chemical*, vol. 134, no. 2, pp. 988–992, 2008.
- [10] T. Sen, N. G. Shimpi, S. Mishra, and R. Sharma, "Polyaniline/ γ -Fe₂O₃ nanocomposite for room temperature LPG sensing," *Sensors and Actuators B: Chemical*, vol. 190, pp. 120–126, 2014.
- [11] S. S. Barkade, D. V. Pinjari, U. T. Nakate et al., "Ultrasound assisted synthesis of polythiophene/SnO₂ hybrid nanolatex particles for LPG sensing," *Chemical Engineering and Processing: Process Intensification*, vol. 74, pp. 115–123, 2013.
- [12] N. M. Vuong, N. D. Chinh, B. T. Huy, and Y.-I. Lee, "CuO-decorated ZnO hierarchical nanostructures as efficient and established sensing materials for H₂S Gas Sensors," *Scientific Reports*, vol. 6, Article ID 26736, 2016.
- [13] B.-Y. Wei et al., "A Novel SnO₂ Gas Sensor Doped With Carbon Nanotubes Operating at Room Temperature," *Sensors and Actuators B: Chemical*, vol. 101, no. 1, pp. 81–89, 2004.
- [14] C. Bittencourt, A. Felten, E. H. Espinosa et al., "WO₃ films modified with functionalised multi-wall carbon nanotubes: morphological, compositional and gas response studies," *Sensors and Actuators B: Chemical*, vol. 115, no. 1, pp. 33–41, 2006.
- [15] S. Liang, H. Bi, J. Ding, J. Zhu, Q. Han, and X. Wang, "Synthesis of α -Fe₂O₃ with the aid of graphene and its gas-sensing property to ethanol," *Ceramics International*, vol. 41, no. 5, pp. 6978–6984, 2015.
- [16] M. Tadic, N. Citakovic, M. Panjan et al., "Synthesis, morphology and microstructure of pomegranate-like hematite (α -Fe₂O₃) superstructure with high coercivity," *Journal of Alloys and Compounds*, vol. 543, pp. 118–124, 2012.
- [17] N. D. Cuong, D. Q. Khieu, T. T. Hoa et al., "Facile synthesis of α -Fe₂O₃ nanoparticles for high-performance CO gas sensor," *Materials Research Bulletin*, vol. 68, pp. 302–307, 2015.
- [18] D. Patil, V. Patil, and P. Patil, "Highly sensitive and selective LPG sensor based on α -Fe₂O₃ nanorods," *Sensors and Actuators B: Chemical*, vol. 152, no. 2, pp. 299–306, 2011.
- [19] Q. Tan, J. Fang, W. Liu, J. Xiong, and W. Zhang, "Acetone sensing properties of a gas sensor composed of carbon nanotubes doped with iron oxide nanopowder," *Sensors*, vol. 15, no. 11, pp. 28502–28512, 2015.
- [20] R. E. Smalley et al., *Carbon Nanotubes: Synthesis, Structure, Properties, And Applications*, vol. 80, Springer Science and Business Media, Berlin, Germany, 2003.
- [21] S. Chaisitsak, B. Chaithongrat, J. Nukeaw, and A. Tuantranont, "Organic vaporsensors based on single-walled CNTs," in *Proceedings of the 2006 5th IEEE Conference on Sensors*, pp. 1081–1084, Republic of Korea, October 2006.
- [22] J. Kong, N. R. Franklin, C. Zhou et al., "Nanotube molecular wires as chemical sensors," *Science*, vol. 287, no. 5453, pp. 622–625, 2000.
- [23] L. Valentini, I. Armentano, J. M. Kenny, C. Cantalini, L. Lozzi, and S. Santucci, "Sensors for sub-ppm NO₂ gas detection based on carbon nanotube thin films," *Applied Physics Letters*, vol. 82, no. 6, pp. 961–963, 2003.
- [24] J. Chuen, "Effects of the Growth Time and the Thickness of the Buffer Layer on the Quality of the Carbon Nanotubes," *Journal of Nanomaterials*, vol. 2017, 6 pages, 2017.
- [25] P. Muthukumar, C. Sumathi, J. Wilson, C. Sekar, S. G. Leonard, and G. Neri, "Fe₂O₃/Carbon nanotube-based resistive sensors for the selective ammonia gas sensing," *Sensor Letters*, vol. 12, no. 1, pp. 17–23, 2014.
- [26] D. Jung, M. Han, and G. S. Lee, "Room-temperature gas sensor using carbon nanotube with cobalt oxides," *Sensors and Actuators B: Chemical*, vol. 204, pp. 596–601, 2014.
- [27] M. Tavakkoli, T. Kallio, O. Reynaud et al., "Maghemite nanoparticles decorated on carbon nanotubes as efficient electrocatalysts for the oxygen evolution reaction," *Journal of Materials Chemistry A*, vol. 4, no. 14, pp. 5216–5222, 2016.
- [28] K. Jantharamsakarn and S. Chaisitsak, "Ferrocene-ethanol-mist CVD grown SWCNT films as transparent electrodes," in *Proceedings of the 7th International Conference on Materials for Advanced Technologies, ICMAT 2013, Symposium G on Carbon Nanotubes and Graphene: Synthesis, Functionalisation and Applications*, pp. 49–58, Singapore, July 2013.

- [29] M. S. Dresselhaus, G. Dresselhaus, R. Saito, and A. Jorio, "Raman spectroscopy of carbon nanotubes," *Physics Reports*, vol. 409, no. 2, pp. 47–99, 2005.
- [30] S. Nagasawa, M. Yudasaka, K. Hirahara, T. Ichihashi, and S. Iijima, "Effect of oxidation on single-wall carbon nanotubes," *Chemical Physics Letters*, vol. 328, no. 4–6, pp. 374–380, 2000.
- [31] M. Lübke, A. M. Gigler, R. W. Stark, and W. Moritz, "Identification of iron oxide phases in thin films grown on Al₂O₃(0 0 0 1) by Raman spectroscopy and X-ray diffraction," *Surface Science*, vol. 604, no. 7–8, pp. 679–685, 2010.
- [32] V. Balouria, A. Kumar, S. Samanta et al., "Nano-crystalline Fe₂O₃ thin films for ppm level detection of H₂S," *Sensors and Actuators B: Chemical*, vol. 181, pp. 471–478, 2013.
- [33] T. J. Simmons, N. Maeda, J. Miao, M. Bravo-Sanchez, J. S. Dordick, and R. J. Linhardt, "Self-assembly of carbon nanotube films from room temperature ionic liquids," *Carbon*, vol. 58, pp. 226–231, 2013.
- [34] O. Akhavan and E. Ghaderi, "Self-accumulated Ag nanoparticles on mesoporous TiO₂ thin film with high bactericidal activities," *Surface and Coatings Technology*, vol. 204, no. 21–22, pp. 3676–3683, 2010.
- [35] N. A. Zubir, C. Yacou, J. Motuzas, X. Zhang, and J. C. Diniz Da Costa, "Structural and functional investigation of graphene oxide-Fe₃O₄ nanocomposites for the heterogeneous Fenton-like reaction," *Scientific Reports*, vol. 4, Article ID 04594, 2014.
- [36] F. L. Souza, K. P. Lopes, P. A. P. Nascente, and E. R. Leite, "Nanostructured hematite thin films produced by spin-coating deposition solution: application in water splitting," *Solar Energy Materials & Solar Cells*, vol. 93, no. 3, pp. 362–368, 2009.
- [37] E. F. Antunes, V. G. De Resende, U. A. Mengui, J. B. M. Cunha, E. J. Corat, and M. Massi, "Analyses of residual iron in carbon nanotubes produced by camphor/ferrocene pyrolysis and purified by high temperature annealing," *Applied Surface Science*, vol. 257, no. 18, pp. 8038–8043, 2011.
- [38] A. Furlan, U. Jansson, J. Lu, L. Hultman, and M. Magnuson, "Structure and bonding in amorphous iron carbide thin films," *Journal of Physics: Condensed Matter*, vol. 27, no. 4, Article ID 045002, 2015.
- [39] M. T. Martínez, M. A. Callejas, A. M. Benito et al., "Sensitivity of single wall carbon nanotubes to oxidative processing: Structural modification, intercalation and functionalisation," *Carbon*, vol. 41, no. 12, pp. 2247–2256, 2003.
- [40] L. Stobinski, B. Lesiak, L. Kövér et al., "Multiwall carbon nanotubes purification and oxidation by nitric acid studied by the FTIR and electron spectroscopy methods," *Journal of Alloys and Compounds*, vol. 501, no. 1, pp. 77–84, 2010.
- [41] A. Benko, A. Przekora, A. Wesełucha-Birczyńska, M. Nocuń, G. Ginalska, and M. Błażewicz, "Fabrication of multi-walled carbon nanotube layers with selected properties via electrophoretic deposition: physicochemical and biological characterization," *Applied Physics A: Materials Science & Processing*, vol. 122, no. 4, article no. 447, 2016.
- [42] S. Singh, N. Verma, A. Singh, and B. C. Yadav, "Synthesis and characterization of CuO-SnO₂ nanocomposite and its application as liquefied petroleum gas sensor," *Materials Science in Semiconductor Processing*, vol. 18, no. 1, pp. 88–96, 2014.
- [43] R. Srivastava and B. Yadav, "Nanostructured ZnFe₂O₄ thick film as room temperature liquefied petroleum gas sensor," *Journal of Experimental Nanoscience*, vol. 10, no. 9, pp. 703–717, 2014.
- [44] K. V. Gurav, S. W. Shin, U. M. Patil et al., "Cu₂ZnSnS₄ (CZTS)-based room temperature liquefied petroleum gas (LPG) sensor," *Sensors and Actuators B: Chemical*, vol. 190, pp. 408–413, 2014.
- [45] S. J. Patil, R. N. Bulakhe, and C. D. Lokhande, "Liquefied petroleum gas (LPG) sensing using spray deposited Cu₂ZnSnS₄ thin film," *Journal of Analytical and Applied Pyrolysis*, vol. 117, pp. 310–316, 2016.
- [46] M. Singh, B. C. Yadav, A. Ranjan, M. Kaur, and S. K. Gupta, "Synthesis and characterization of perovskite barium titanate thin film and its application as LPG sensor," *Sensors and Actuators B: Chemical*, vol. 241, pp. 1170–1178, 2017.
- [47] S. Chaisitsak, "Nanocrystalline SnO₂:F thin films for liquid petroleum gas sensors," *Sensors*, vol. 11, no. 7, pp. 7127–7140, 2011.
- [48] V. V. Jadhav, S. A. Patil, D. V. Shinde et al., "Hematite nanostructures: Morphology-mediated liquefied petroleum gas sensors," *Sensors and Actuators B: Chemical*, vol. 188, pp. 669–674, 2013.
- [49] V. N. Mishra and R. P. Agarwal, "Sensitivity, response and recovery time of SnO₂ based thick-film sensor array for H₂, CO, CH₄ and LPG," *Microelectronics Journal*, vol. 29, no. 11, pp. 861–874, 1998.
- [50] R. K. Roy, M. P. Chowdhury, and A. K. Pal, "Room temperature sensor based on carbon nanotubes and nanofibres for methane detection," *Vacuum*, vol. 77, no. 3, pp. 223–229, 2005.
- [51] M. D. Ganji, A. Mirnejad, and A. Najafi, "Theoretical investigation of methane adsorption onto boron nitride and carbon nanotubes," *Science and Technology of Advanced Materials*, vol. 11, no. 4, Article ID 045001, 2010.
- [52] J. Suehiro, H. Imakiire, S.-I. Hidaka et al., "Schottky-type response of carbon nanotube NO₂ gas sensor fabricated onto aluminum electrodes by dielectrophoresis," *Sensors and Actuators B: Chemical*, vol. 114, no. 2, pp. 943–949, 2006.
- [53] S. Mao, S. Cui, K. Yu, Z. Wen, G. Lu, and J. Chen, "Ultrafast hydrogen sensing through hybrids of semiconducting single-walled carbon nanotubes and tin oxide nanocrystals," *Nanoscale*, vol. 4, no. 4, pp. 1275–1279, 2012.
- [54] L. A. Patil, M. D. Shinde, A. R. Bari, V. V. Deo, D. M. Patil, and M. P. Kaushik, "Fe₂O₃ modified thick films of nanostructured SnO₂ powder consisting of hollow microspheres synthesized from pyrolysis of ultrasonically atomized aerosol for LPG sensing," *Sensors and Actuators B: Chemical*, vol. 155, no. 1, pp. 174–182, 2011.
- [55] Z. Dai, C.-S. Lee, Y. Tian, I.-D. Kim, and J.-H. Lee, "Highly reversible switching from P- to N-type NO₂ sensing in a monolayer Fe₂O₃ inverse opal film and the associated P-N transition phase diagram," *Journal of Materials Chemistry A*, vol. 3, no. 7, pp. 3372–3381, 2015.